Cape Peninsula
University of Technology

GREEN SYNTHESIS, CHARACTERIZATION AND APPLICATIONS OF CdSe BASED CORE-SHELL QUANTUM DOTS AND SILVER NANOCOMPOSITES

by

SNEHA BHAGYARAJ

Thesis submitted in fulfilment of the requirements for the degree

Doctor of Technology: CHEMISTRY

In the Faculty of APPLIED CHEMISRY

At the

Cape Peninsula University of Technology

Supervisor : Prof Oluwatobi Samuel Oluwafemi

Co-supervisor: Prof Sabu Thomas

Prof Nandakumar Kalarikkal

Cape Town

December 2015

DECLARATION

I, **SNEHA BHAGYARAJ** declare that the contents of this dissertation/thesis represent my own unaided work, and that the dissertation/thesis has not previously been submitted for academic examination towards any qualification. Furthermore, it represents my own opinions and not necessarily those of the Cape Peninsula University of Technology.

31/12/2015

Signed **Date**

ABSTRACT

Researchers around the world are now focusing on inculcating green chemistry principles in all level of research especially in nanotechnology to make these processes environmental friendly. Nanoparticles synthesized using green chemistry principles has several advantages such as simplicity, cost effectiveness, compatibility for biomedical and pharmaceutical applications and large scale production for commercial purpose. Based on this background, this thesis present the design, synthesis, characterization and applications of various CdSe based core-shell and core-multi shell quantum dots (QDs), quantum dots-polymer nanocomposites, silver nanoparticles (Ag-NPs) and silver nanocomposites via completely green methods. Various QDs like CdSe/CdS/ZnS and CdSe/ZnS, and there polymer nanocomposites were successfully synthesized and characterized. The high quality of the as-synthesized nanoparticles was confirmed using absorption and photoluminescence (PL) spectroscopy, Fourier transform infrared spectroscopy (FTIR), Raman spectroscopy, transmission electron microscopy (TEM) and high resolution TEM (HRTEM). Detailed optical and morphological characterization showed that the CdSe/CdS/ZnS core-multi shell QDs were small, monodispersed with high fluorescent intensity and narrow emission width. The CdSe/CdS/ZnS core multi-shell QDs were dispersed in epoxy polymer matrix to obtain fluorescent epoxy nanocomposite. The brillouin spectroscopy analysis revealed that the presence of QDs inside polymer composite reduces the acoustic frequency of the polymer. Highly fluorescent CdSe/ZnS core-shell QDs was also synthesized and dispersed in PMMA polymer matrix to prepare bright yellow emitting nanocomposite film. The as-synthesized QDs also undergone surface exchange to convert the organically soluble nanomaterial to water soluble. After the ligand exchange, the morphology and above all the fluorescence property of the quantum dots remained intact. In another approach, HDA-capped CdSe nanoparticles were synthesized in the absence of an inert gas followed by dispersion in polymer polycaprolactone to produce orange light emitting electrospun polymer nanocomposite nanofibre.

Furthermore, the synthesis of stable silver nanoparticles (Ag-NPs) and its composites using green chemistry principle was also investigated. Various biopolymer capped, dextrose reduced Ag-NPs and Ag nanocomposites were synthesized. Detailed optical, morphological, antibacterial, catalytic and sensing properties of the as-synthesized Ag-NPs and their nanocomposites were also carried out. Small, monodispersed and stable gelatin and starch capped Ag-NPs were synthesized. Both gelatin capped Ag-NPs and starch capped Ag-NPs showed good antibacterial property against *E.coli* and *P.aeruginosa*. The cell viability of the as-synthesised Ag-NPs against human THP-1 cells shows that, the as-synthesized particles are less toxic at concentrations less than 10 μg/mL. The as-synthesized Ag-NPs showed efficient sensing activity against H_2O_2. Gelatin-capped Ag-NPs showed a detection limit upto 10^{-6} M while starch-capped Ag-NPs was upto 10^{-10} M. Hybrid nanostructures were also prepared using gelatin capped Ag-NPs via a simple procedure. The analyses showed that Ag-NPs were

aligned on the surface of multi-wall carbon nanotubes (MWCNTs) to form Ag-MWCNTs hybrid nanostructure which showed promising catalytic activity for the conversion of p-nitrophenol to p-aminophenol in the presence of $NaBH_4$. It is believed that this synthetic route will enable the development of other novel nanostructures with unique properties for industrial application in the biological and optical fields.

ACKNOWLEDGEMENTS

I owe my deepest gratitude to my supervisor, Prof. Oluwatobi Samuel Oluwafemi for his persistent support, guidance and encouragement, throughout my PhD career. I am so privileged to have an inspiring guide like him who gave me the freedom to explore innovative trends in my field of study. I thank him for the constructive discussions along the years and for reviewing my thesis.

I offer my sincere gratitude to my co-supervisor Prof. Sabu Thomas for his enlightening guidance and inspiring instruction in the development and completion of this study. I express my sincere thanks to Dr. Nandakumar Kalarikkal for offering me an opportunity to explore the research world. I am grateful to the financial support rendered by National Research Foundation (NRF), South Africa and Department of Science and Technology (DST), Government of India for conducting the studies. Opinions expressed in this thesis and the conclusions arrived at, are those of the author, and are not necessarily to be attributed to the National Research Foundation.

My sincere gratitude also goes to Dr M. Matoetoe and Dr Simphiwe Nelana, Cape Peninsula University of Technology (CPUT), Cape Town campus for their immense support. I offer my appreciation to Prof .Didier Rouxel for inviting me to Institute Jean Lamour, Nancy, France for a research visit and helping me to carry out characterizations of my samples. I am grateful to Dr. V.P.Jayachandran for his assistance on antibacterial studies at Pushpagiri Medical College, Thiruvalla, Kerala, India.

I would like to thank all my colleagues at the International and Interuniversity Centre for Nanoscience and Nanotechnology, Mahatma Gandhi University for their immense support during my research. A good support system is important to do higher studies abroad and in this respect, I would like to thank all my colleagues and laboratory mates at CPUT and University of Johannesburg for their encouragement and immense support.

A special gratitude and love goes to my family for their unfailing support. I thank my mother, Mrs Aruna Mohan for her trust and immense support in all works of my life. I also express my deepest love and thanks to my husband, Mr. Bhagyaraj G. Panicker, for his understanding and encouragement throughout which helped me to move forward. Special love for my daughter, baby Gowri Bhagyaraj.

Above all, I thank God, for giving me this opportunity and the intellect to understand the complexity of research. Thank You for always sending your angels whenever I feel lost.

DEDICATION

TO MY FAMILY

PUBLICATIONS

1. A. Journal Papers

- **Mohan, S**.; Oluwafemi, O.S.; Songca, S.P.; Osibote, O.A.; George, S.C.; Kalarikkal, N.; Thomas, S. Facile synthesis of transparent and fluorescent epoxy–CdSe–CdS–ZnS core–multi shell polymer nanocomposites, **New Journal of Chemistry**, **2014**, 38 (1), 155-162.

- **Mohan, S**.; Oluwafemi,O.S.; George, S.C.; Jayachandran, V.P.; Lewu, F.B.; Songca, S.P; Kalarikkal, N.; Thomas, S. Completely green synthesis of dextrose reduced silver nanoparticles, its antimicrobial and sensing properties, **Carbohydrate Polymers**, **2014**,106, 469-474.

- **Mohan, S**.; Oluwafemi, O.S.; Songca, S.P.; Rouxel, D.; Miska, P.; George, S.C.; Kalarikkal, N.; Thomas, S. Green synthesis of CdSe/ZnS core-shell quantum dot nanophosphours and its Poly methyl methacrylate composite thin film in the visible spectral range, **Materials Research Society Symposium Proceedings, 2014**, DOI: 10.1557/opl.2015.76.

- **Mohan, S**.; Oluwafemi,O.S.; Kalarikkal, N.; Thomas, S. Antibacterial and sensing properties of dextrose reduced starch -capped silver nanoparticles synthesised via a completely green method. **Materials Today Proceedings, 2015.** 10.1016/j.matpr.2015.08.023.

- **Mohan, S**.; Oluwafemi, O.S.; Songca, S.P.; Rouxel, D.; Miska, P.; George, S.C.; Kalarikkal, N.; Thomas, S. Green Synthesis of yellow emitting PMMA-CdSe/ZnS quantum dots nanophosphors , **Material science in semiconductor processing,** 39 (**2015**) 587–595.

- **Mohan, S.;** Oluwafemi, O.S.; Songca, S.P.; Jayachandran, V.P; Rouxel, D.; Joubert, O; Kalarikkal, N.; Thomas, S. Synthesis, antibacterial, cytotoxicity and sensing properties of starch -capped silver nanoparticles, **Journal of molecular liquids,** 213 (**2016**) 75-81**.**

- **Mohan, S**.; Okumu, F.; Oluwafemi, O.S.; Matoetoe, M.; Arotiba, O. Electrochemical Behaviour of Silver Nanoparticle-MWCNTs Hybrid Nanostructures Synthesized via a Simple Method. **Int. J. Electrochem. Sci.,** 11 **(2016**) 745 – 753.

- **Mohan, S.;** Oluwafemi, O.S.; Songca, S.P.; Rouxel, D.; Miska, P.; Lewu, F.B.; Kalarikkal, N.; Thomas, S. Completely green synthesis of silver nanoparticle decorated MWCNT and its antibacterial and catalytic properties, **Pure Appl. Chem.** 88(1-2) **(2016)** 71-81.

B. Book chapters

Sneha Mohan, Oluwatobi Samuel Oluwafemi, Nandakumar Kalarikkal, Sabu Thomas Biopolymers: Application in Nanoscience and Nanotechnology. Chapter 3, Recent Advances in Biopolymers. ISBN 978-953-51-2255-5, InTech publishers, Croatia.

http://www.intechopen.com/articles/show/title/biopolymers-application-in-nanoscience-and-nanotechnology

Sneha Mohan, Jiji Abraham, Oluwatobi Samuel Oluwafemi, Nandakumar Kalarikkal, Sabu Thomas Rheology and Processing of Inorganic Nanomaterials and Quantum Dots / Polymer Nanocomposites. Rheology and Processing of Polymer nano composites, Wiley and Sons, Canada. (In press)

C. Books edited

Sneha Mohan, Oluwatobi S. Oluwafemi, Nandakumar Kalarikkal, Sabu Thomas. Synthesis, Characterization and Applications of Nanomaterials, 3 volumes, John Wiley and sons, Canada. (Under processing)

D. Conference attended

1. **Sneha Mohan**, Oluwafemi Oluwatobi, Sandile Songca, Nandakumar Kalarikkal, Sabu Thomas (2015). Completely green synthesis of dextrose reduced silver nanoparticles decorated MWCNT, its antibacterial and catalytic properties. TMS 144th Annual Meeting and Exhibition, Walt Disney World, Orlando, USA, 15th -19th March. (oral presentation)
2. **Sneha Mohan**, Oluwatobi.S Oluwafemi, Sandile.P Songca, Nandakumar Kalarikkal, Sabu Thomas, Completely green synthesis of dextrose reduced silver nanoparticles decorated MWCNT, its antibacterial, sensing and catalytic properties, Proceeding of second international U6 consortium conference held at Cape peninsula University, Capetown, 5th to 10th September 2014, p96. (Oral presentation)
3. **Sneha Mohan**, Oluwatobi.S Oluwafemi, Sandile.P Songca, Nandakumar Kalarikkal, Sabu Thomas, Completely green synthesis of silver nanoparticles decorated MWCNT, its antibacterial and catalytic properties, proceedings of 5th International conference on Green chemistry , held at Durban, South Africa, 17th to 21st August 2014. (Oral presentation)
4. **Sneha Mohan**, Oluwatobi.S Oluwafemi, Sandile.P Songca, Nandakumar Kalarikkal, Sabu Thomas, Stable efficient CdSe/ZnS core-shell nanophosphors fabrication through a phosphine- free route, Proceedings of India-Israel meeting on Material science and Nanoscience (IIMMN 2013), held at Mahatma Gandhi University, Kottayam, Kerala, India, 31st January to 1st February 2013, p107. (Third prize for poster presentation)
5. **S. Mohan**, O.S. Oluwafemi, N. Kalarikkal, S. Thomas, Green synthesis of CdSe polymer nanocomposite using a non-phosphine method, 21st DAE-BRNS National Laser

Symbosium (NLS 21) held at Baba Atomic Research Center, Mumbai, India on 6th-9th February 2013, p115.(Poster presentation)

6. **Sneha Mohan**, Oluwatobi.S Oluwafemi, S.P Songca, Nandakumar Kalarikkal, Sabu Thomas, Simple green synthesis of dextrose reduced silver nanoparticles and their antibacterial property, Proceedings of NanoIndia 2013, held at NIIST, Trivandrum, Kerala, India on 19th-20th February 2013,p72. (Poster presentation).

7. **Sneha Mohan**, Arun S Menon, O.S Oluwafemi, SP Songca ,Nandakumar Kalarikkal, Sabu Thomas (2012): Synthesis of High Quality CdSe/CdS/Zns Core- shell nanocomposite with High Life Time and increased mechanical property. Second International conference on Nanomaterials: Synthesis, Characterization and Applications (ICN 2012), Mahatma Gandhi University, Kerala, India, 12th -15th January.

8. **Sneha Mohan**, Oluwatobi.S Oluwafemi, Sandile P Songca, Nandakumar Kalarikkal, Sabu Thomas (2012): Simple green synthesis of dextrose reduced silver nanoparticles and their antimicrobial activity. Third International Conference on Natural Polymer (ICNP), Kottayam, Kerela, India, 26-28 Oct.

TABLE OF CONTENTS

LIST OF FIGURES

LIST OF TABLES

GLOSSARY

QDs	**Quantum dots**
Ag-NPs	**Silver nanoparticles**
NCs	**Nanocrystals**
CSNCs	**Core-shell nanocrystals**
CSQDs	**Core-shell quantum dots**
PMMA	**Poly methyl methacrylate**
PMC	**Polymer-matrix composite**
SERS	**Surface Enhanced Raman Scattering**
QDSSCs	**Quantum dot sensitized solar cells**
OA	**Oleic acid**
DDM	**4, 4' diaminodiphenyl methane**
PCL	**poly (e-caprolactone)**
LED	**Light emitting diodes**
MIC	**Minimum Inhibitory Concentration**
PLQY	**Photoluminescence quantum yield**
LSPR	**Localized surface plasmon resonance**
MBC	**Minimum Bactericidal Concentration**
MWCNTs	**Multiwall Carbon Nanotubes**
HDA	**Hexadecylamine**

Chapter 1

Introduction

Recent developments in nanofabrication technologies have facilitated the realization of novel semiconductor nanostructures with properties tailored for specific applications (Murphy, 2002). Nanostructures with spatial dimensions comparable to the de Broglie wavelength of charge carriers residing in the material are readily engineered with nanometer precision. At this length scale, quantum confinement effects modify the electronic and optical properties and interesting quantum phenomena emerge. Among these nanostructured materials, semiconductor nanocrystals have generated a lot of interest among researchers in the past decades due to their wide range of applications in photonics, electronics and optoelectronics (Gur et al., 2005; Peng et al., 2005; Murray et al., 1993; Khani et al., 2011). In addition, extensive experimental and theoretical efforts have been made in the synthesis as well as tuning the size and properties of these materials. Various physical and chemical methods have been used to synthesize nanomaterials (Luo et al., 2005; Khanna et al., 2005; Fromm et al., 2006; Hu et al., 2008). As advancement on these synthetic techniques continue to unfold, there has been an upsurge interest in implementing green chemistry principles into the synthesis of nanomaterials in order to maximize safety and efficiency, and minimize the environmental and societal impact of these materials.

1.1 Nanotechnology

The manipulation of matter on an atomic, molecular, and supramolecular scale was done for the first time by Michael Faraday in 1847 when he reported the unique optical

properties of metallic gold nanoparticles compared to its bulk counterpart (Faraday, 1857). However, he was unsuccessful in explaining the vivid colour change of the mixture which seemed to change depending on the particle size of the nanoparticle. The concept of nano regime was again introduced in a lecture by Richard Feynman (a Nobel laureate) in 1959 which was published in 1960 (Feynman, 1960). In his lecture he mentioned that “the principle of physics, as far as I can see, do not speak against the possibility of maneuvering things atom by atom”. Feynman described a process by which the ability to manipulate individual atoms and molecules might be developed, using one set of precise tools to build and operate another proportionally smaller set, and so on, down to the needed scale. In the course of this, he noted, scaling issues would arise from the changing magnitude of various physical phenomena: gravity would become less important, surface tension and Van der Waals attraction would become more important, etc. This basic idea appears plausible, and exponential assembly enhances it with parallelism to produce a useful quantity of end products. The term “nanotechnology” was defined by Tokyo Science University Professor, Norio Taniguchi (Taniguchi, 1974) in a 1974 paper as follows: “Nano-technology’ mainly consists of the processing of, separation, consolidation, and deformation of materials by one atom or by one molecule.”

In the 1980s the basic idea of this definition was explored in much more depth by Dr. K. Eric Drexler, who promoted the technological significance of nano-scale phenomena and devices through speeches and the books Engines of Creation: The Coming Era of Nanotechnology (1986) and Nanosystems: Molecular Machinery, Manufacturing, and Computation, and so the term acquired its current sense. Nanotechnology and nanoscience got started in the early 1980s with two major developments; the birth of

cluster science and the invention of the scanning tunneling microscope (STM). This development led to the discovery of fullerenes (Kroto et al., 1985) in 1986 and carbon nanotubes (Iijima., 1991) a few years later. In another development, the synthesis and properties of semiconductor nanocrystals was studied; this led to a fast increasing number of metal oxide nanoparticles of quantum confinement regime. The atomic force microscope was invented six years after the STM was invented.

1.2 Nanomaterials

Materials at a size regime of nanometer scale show very interesting and unique characteristic properties (Greenham et al., 1996). Thus, nanomaterials are defined as materials with at least one dimension in the size range from approximately 1-100 nanometers. Nanoparticles are objects with confinement in all three external dimensions and are also referred to as zero dimensional materials (Lovestam et al., 2010). Nanoparticles that are naturally occurring (e.g., volcanic ash, soot from forest fires) or incidental byproducts of combustion processes (e.g., welding, diesel engines) are usually physically and chemically heterogeneous and often termed ultrafine particles (The science museum London, n.d). Materials engineered to a small scale are often referred to as engineered nanomaterials (ENMs), which can take on unique optical, magnetic, electrical, and other properties (Lin et al., 2010). Engineered nanoparticles are intentionally produced and designed with very specific properties related to shape, size, surface properties and chemistry. These properties are reflected in aerosols, colloids, or powders. Often, the behavior of nanomaterials may depend more on the surface area than particle composition itself. Relative-surface area is one of the principal factors that enhance their reactivity, strength and electrical properties. These emergent properties have the potential

for great impacts in electronics, medicine, and other fields. The significance of various nanoparticles in advanced applications has increased the extent of research related to this field.

There are various classes of nanomaterials. These incudes; carbon based nanomaterials, metal and metal oxide nanostructures, dendrimers, nanocomposites, zeolites, polymeric nanostructures etc. Metallic nanoparticles exhibit size and shape-dependent properties that are of interest for applications ranging from catalysts and sensing to optics, antibacterial activity and data storage (Choi et al., 2007; Sudrick et al., 2006). For instance, the antibacterial activity of different metal nanoparticles such as silver colloids is closely related to their size; that is, the smaller the silver nuclei, the higher the antibacterial activity. Moreover, the catalytic activity of these nanoparticles is also dependent on their size as well as their structure, shape, size distribution, and chemical – physical environment (Yeo et al., 2003; Zhang et al., 2004). Thus, control over the size and size distribution is an important task and specific control of shape, size, and size distribution is often achieved by varying the synthesis method, reducing agent and stabilizer.

Quantum dots are tiny particles or nanocrystals of a semiconducting material with diameters in the range of 2-10 nanometers (10-50 atoms). They were first discovered in 1980 (Ekimov & Onushchenko, 1981). Quantum dots display unique electronic properties, intermediate between those of bulk semiconductors and discrete molecules, which are partly the result of the unusually high surface-to-volume ratios (Kastner, 1993; Ashoori, 1996; Vossmeyer & Heath, 1998; Alivisators, 1996; Yoffe, 1993). The most apparent result of this is fluorescence, wherein the nanocrystals can produce distinctive colors determined by the size of the particles.

1.3 Quantum confinement

The quantum confinement effect is observed when the size of the particle is too small to be comparable to the wavelength of the electron (Chan et al., 2011). The word confinement means to confine the motion of randomly moving electron or to restrict its motion in specific energy levels (discreteness) and quantum reflects the atomic realm of particles. So as the size of a particle decrease till it reach a nano scale, the decrease in confining dimension makes the energy levels discrete and this increases or widens up the band gap and ultimately the band gap energy also increases (Gibbs et al., 2011). Specifically, the effect describes the phenomenon resulting from electrons and electron holes being squeezed into a dimension that approaches a critical quantum measurement, called the exciton Bohr radius. Quantum confinement increases the spacing between energy levels as the nanocrystallite size is decreased. The origin of quantum confinement in so-called zero-dimensional nanocrystallites, such as quantum dots (QDs), is understood to arise from the spatial confinement of electrons within the crystallite boundary. Qualitatively this effect is analogous to the problem of a particle in a box, and efforts to quantify confinement effects have been the topic of considerable research. In current applications, a quantum dot such as a small sphere confines in three dimensions, a quantum wire confines in two dimensions, and a quantum well confines only in one dimension. These are also known as zero-, one- and two-dimensional potential wells, respectively. In these cases they refer to the number of dimensions in which a confined particle can act as a free carrier. Figure 1 represents a schematic diagram of the quantum confinement effect in nanostructures.

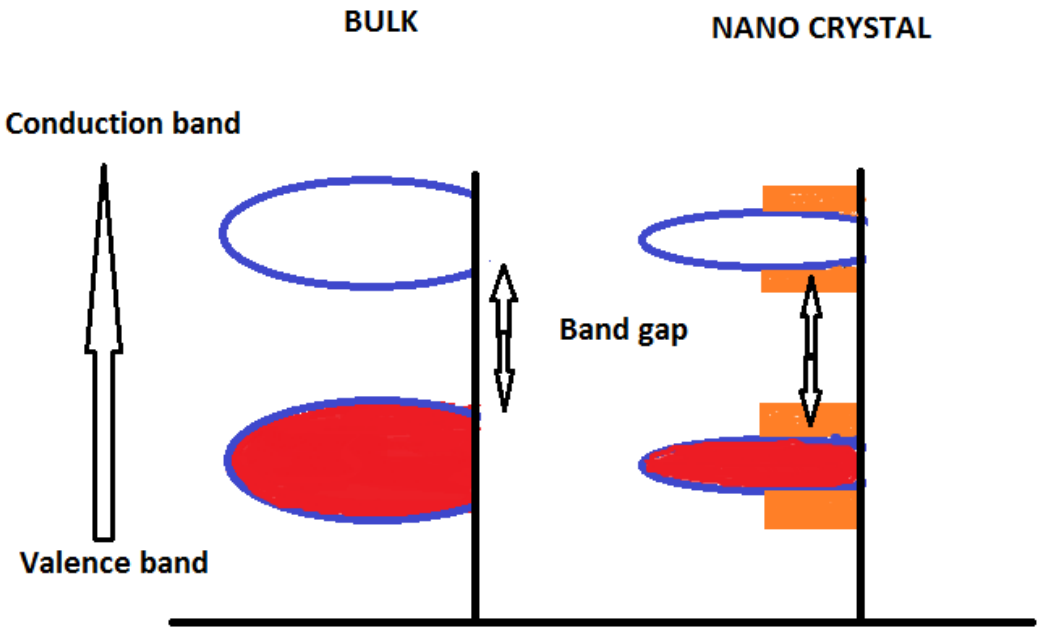

Figure 1.1: Simple schematic representation of the quantum confinement effect.

1.4 The Excitons

Excitons also known as electron–hole pairs bound by the Columbic interaction, are the fundamental quasiparticles of coherent light–matter interaction relevant for processes such as photosynthesis and optoelectronics (Chan et al., 2011; Gibbs et al., 2011; Turner & Nelson, 2010; Cundiff & Mukamel, 2013; Lee et al., 2007) . The existence of excitons in semiconductors is well established (Vossmeyer & Heath, 1998). For metals, the experimental manifestations of excitons are questionable due to screening of the Columbic interaction taking place on timescales of a few femtoseconds (Edward et al., 2010; Silkin et al., 2010; Huber et al., 2001). The electronic elementary excitations in solids mainly possess a spatial extension several times larger than the lattice constant of the crystal. The semiconductor nanostructures, depending on the confinement geometry, have been classified into two-dimensional (quantum wells), one-dimensional (quantum

wires), and zero-dimensional (quantum dots) objects. In quantum wells and quantum wires a translational symmetry in two or one dimension and a statistically large number of electrons and holes can be created. But in the case of semiconductor quantum dots, the translational symmetry is broken in all directions and only a finite number of excitations can be born within one and the same dot.

The history of quantum dot research started with the simple concept of the particle-in an-infinite-spherical-box problem. Initially the concept of weak and strong confinement limits for the quantum dots were introduced after totally neglecting the Coulombic interaction between the confined electron and hole. In this case, the quantization of the center-of-mass motion of the confined electron-hole pair with the lowest energy state is considered.

1.5 Aims and Objectives

The main aims of the study are

- To design and synthesize various CdSe QDs based core-shell quantum dots and its polymer nanocomposites.
- To synthesis stable silver nanoparticles and its composites using green reagents for antibacterial, sensing and catalytic applications.

The main objectives of the study are:

1. To design and synthesize various CdSe based core –shell and core-multi shell quantum dots and their polymer nanocomposites.

2. To carry out detailed optical and morphological characterization of the core-shell quantum dots and their polymer nanocomposites.
3. To synthesis stable silver nanoparticles (Ag-NPs) and their nanocomposites using green chemistry principle.
4. To study the detailed optical and morphological properties of the as-synthesised Ag-NPs and their nanocomposites.
5. To study the antibacterial and cytotoxic properties of the as synthesized Ag-nanoparticles.
6. To study the antibacterial, catalytic and sensing properties of the as-synthesized silver nanocomposites.

1.6 Significance of the study

1. Development of cadmium based core-shell QDs fluorescent polymer nanocomposites via an environmentally benign method.
2. Green synthesis of stable monodispersed biopolymer capped silver nanoparticles without using any accelerator.
3. Green synthesis of silver-hybrid nanocomposites using simple method.
4. Development of high efficient catalysts and sensors using silver- nanocomposites.
5. To gain an in depth understanding on the green synthesis of the nanoparticles and nanocomposites, their properties and applications

References

Alivisatos, A. P. 1996. Semiconductor Clusters, Nanocrystals, and Quantum Dots. *Science*, 271: 933–937.

Ashoori, R. C. 1996. Electrons in artificial atoms. *Nature,* 379 (6564): 413- 419.

Chan, W-L., Ligges, M., Jailaubekov, A., Kaake, L., Avila, L. M. & Zhu, X. Y. 2011. Observing the multiexciton state in singlet fission and ensuing ultrafast multielectron transfer. *Science,* 334: 1541–1545.

Choi, Y., Ho, N. & Tung, C. 2007. Sensing phosphatase activity by using gold nanoparticles. *Angew. Chem. Int. Ed*., 46: 707-709.

Cundiff, S. T. & Mukamel, S. 2013. Optical multidimensional coherent spectroscopy. *Phys. Today,* 66: 44–49.

Edwards, P. P., Lodge, M. T. J., Hensel, F. & Redmer, R. 2010. '... a metal conducts and a non-metal doesn't'. *Phil. Trans. R. Soc. A,* 368: 941– 965.

Ekimov, A. I. & Onushchenko, A. A. 1981. Quantum size effect in three-dimensional micro- scopic semiconductor crystals. *JETP Lett*., 34: 345–349.

Faraday, M., "The Bakerian Lecture: Experimental Relations of Gold (and Other Metals) to Light," Philosophical Transactions of the Royal Society of London, 1857, 145–181 <doi:10.1098/rstl.1857.0011>

Feynman, R. P. 1960. A lecture in engineering science. In California Institute of Technology February edn.

Fromm, D. P., Sundaramurthy, A., Kinkhabwala, A., Schuck, P. J., Kino, F. S & Moerner, W. E. 2006. Aligned silver nanorod arrays for surface-enhanced Raman spectroscopy. *J. Chem. Phys*., 124: 061101.

Gibbs, H. M., Khitrova, G. & Koch, S. W. 2011. Exciton–polariton light-semiconductor coupling effects. *Nature Photon*, 5: 273–273.

Greenham, N. C., Peng, X., & Alivisatos, A. P. 1996. Charge separation and transport in conjugated-polymer/semiconductor-nanocrystal composites studied by photoluminescence quenching and photoconductivity. *Phys. Rev. B,* 54:17628.

Gur, I., Fromer, N.A., Geier, M. L. & Alivisatos, A. P. 2005. Air-stable all-inorganic nanocrystal solar cells processed from solution. *Science,* 310: 462-465.

Hu, B., Wang, S. B., Wang, K., Zhang, M & Yu, S. H. 2008. Microwave-Assisted Rapid Facile “Green” Synthesis of Uniform Silver Nanoparticles: Self-Assembly into Multilayered Films and Their Optical Properties. *J. Phys. Chem. C,* 112: 11169–11174.

Huber, R., Tauser, F., Brodschelm, A., Bichler, M., Abstreiter, G. & Leitenstorfer, A. 2001. How many-particle interactions develop after ultrafast excitation of an electron–hole plasma. *Nature,* 414: 286–289.

Iijima, S. 1991. "Helical microtubules of graphitic carbon". *Nature,* 354 (6348): 56–58.

Kastner, M. A. 1993. Artificial Atoms. *Physics Today,* 46(1): 24-31

Khani, O., Rajabi, H. R., Yousefi, M. H., Khosravi, A. A., Jannesari, M & Shamsipur, M. 2011. Synthesis and characterizations of ultra-small ZnS and Zn(1-x)Fe(x)S quantum dots in aqueous media and spectroscopic study of their interactions with bovine serum albumin. *Spectrochim. Acta, Part A,* 79: 361-369.

Khanna, P. K., Singh, N., Charan, S & Viswanath, A. K. 2005. Synthesis of Ag/polyaniline nanocomposite via an in situ photo-redox mechanism. *Mater. Chem. Phys.*, 92: 214–219.

Kroto, H. W., Heath, J. R., O’Brien, S. C., Curl R. F., & Smalley, R. E. 1985. 'C60: Buckminsterfullerene. *Nature,* 318: 162-163.

Lee, H., Cheng, Y-C. & Fleming, G. R. 2007. Coherence dynamics in photosynthesis: Protein protection of excitonic coherence. *Science,* 316: 1462–1465.

Lin, D., Tian, X., Wu, F. & Xing, B. 2010. Fate and transport of engineered nanomaterials in the environment. *J Environ. Qual*., 39(6):1896-1908.

Lövestam, G., Rauscher, H., Roebben,G., Klüttgen, B. S., Gibson, N., Putaud, J. P. & Stamm, H. 2010. Considerations on a Definition of Nanomaterial for Regulatory Purposes, No. EUR 24403 EN: Joint Research Center (JRC) of the EU Commission;

Luo, C.C., Zhang, Y.H., Zeng, X. Z.,Zeng, Y. W & Wang, Y. G. 2005. The role of poly(ethyleneglycol) in the formation of silver nanoparticles. *J Colloid Interface Sci.,* 288: 444–448.

Murphy, C. J. 2002 Optical sensing with quantum dots. *Anal. Chem.,* 74(19): 520A-526 A.

Murray, C. B., Norris, D. J. & Bawendi, M. G. 1993. Synthesis and characterization of nearly monodisperse CdE (E = sulfur, selenium, tellurium) semiconductor nanocrystallites. *J. Am. Chem. Soc.,* 115: 8706-8715.

Peng, P., Milliron, D. J., Hughes, S. M., Johnson, J. C., Alivisatos, A. P. & Saykally, R. J. 2005. Femtosecond spectroscopy of carrier relaxation dynamics in type II CdSe/CdTe tetrapod hetero nanostructures. *Nano Lett.,* 5: 1809-13.

Silkin, V. M., Kazansky, A. K., Chulkov, E. V. & Echenique, P. M. 2010. Time-dependent screening of a point charge at a metal surface. *J. Phys. Condens. Matter,* 22: 304013.

Sudrik, S., Chaki, N., Chavan, V. & Chavan, S. 2006. Silver Nanocluster Redox-Couple-Promoted Nonclassical Electron Transfer: An Efficient Electrochemical Wolff Rearrangement of α-Diazoketones. *Chemistry,* 12: 859-864.

Taniguchi, N. 1974. "On the Basic Concept of 'Nano-Technology'," Proc. Intl. Conf. Prod. Eng. Tokyo, Part II, Japan Society of Precision Engineering.

The science museum London (no date) Nature’s nanoparticles. Available: http://www.sciencemuseum.org.uk/antenna/nano/planet/143.asp [Accessed on 26 May 2015]

Turner, D. B. & Nelson, K. A. 2010. Coherent measurements of high-order electronic correlations in quantum wells. *Nature,* 466: 1089–1092.

Vossmeyer, T. & Heath, J. R. 1998. Nanocrystal supper lattices. *Annu. Rev. Phys. Chem*., 49: 371-404.

Yeo, S., Lee, H. & Jeong, S. 2003. Preparation of nanocomposite fibers for permanent antibacterial effect. *J. Mater. Sci.,* 38: 2143-2147.

Yoffe, A. D. 1993. Low-dimensional systems: quantum size effects and electronic properties of semiconductor micro crystallites (zero-dimensional systems) and some quasi-two-dimensional systems. *Adv. Phys.,* 42(2): 173-266.

Zhang, J., Chen, P., Sun, C. & Hu, X., 2004. Sonochemical Synthesis of Colloidal Silver Catalysts for Reduction of Complexing Silver in DTR System. *Appl. Catal.* A, 266: 49-54.

Chapter 2

Literature review

2.1 Overview of Quantum dots:

A quantum dot (QD) is a fascinating novel nanoscale structure of great scientific interest to a wide variety of discipline, consisting of one or more semiconducting materials in which the motion of fundamental charge carriers is confined in all spatial dimensions (Balkanski & Wallis, 2000). According to the concept of physics, a quantum dot is a semiconductor nanocrystal exhibiting confinement in all three dimensions which can be further elaborated as a nanocrystal with a diameter smaller than the bulk exciton Bohr radius. The first experimental demonstrations of such confinement in two dimensions were given by Chang *et al*., and Dingle *et al*., in 1974 using various structures of Ga and As, whilst the first evidence for three-dimensional confinement was published by Ekimov in the early 1981. Quantum confinement in QDs leads to the existence of discrete energy states for the confined electron and hole when compared to the energy bands present in the bulk semiconductor material. The optical and electronic behaviour exhibited by the dots is distinctly atom-like, and this fact has led to the description of QDs as “artificial atoms” (Reed, 1993).

Confinement in QDs leads to interesting size tunable optical properties. The most exploited property of QDs is their size dependent band edge fluorescence. Recent studies also revealed that single QDs have intermittent fluorescence due to a three body Auger recombination process (Fisher et al, 2004). Due to their high quantum yield, tunable and

narrow fluorescence, customizable functionality and high resistance to photobleaching and photochemical degradation, QDs cover a wide range of applications. Various applications of QDs include QD lasers displays and other light-emitting devices, flash memory devices as floating gates photovoltaic cells based on QDs, fluorescent tags for biological applications like cellular imaging and labelling and so on (Mokhoff, 2006; Bowers et al., 2005 ; Talbot, 2007; Michalet et al., 2005). QDs can be overcoated with another semiconductor to further confine the exciton and to produce material with a new band gap (Peng et al., 1997). This kind of confined stuctures are called core-shell quantum dots (CSQDs) which will be further discussed in this chapter.

2.1.1 Electronic band structure of CdSe

CdSe is a II-VI direct band gap semiconductor due to the position of Cd and Se in the periodic table. The bulk CdSe usually has hexagonal structure (Motohisa et al., 1995). The exciton bohr radius of bulk CdSe is ~ 6 nm with broad and featureless absorption spectrum starting at ~716 nm (Kim et al., 2003). The valence band originates from the 4p state of selenium and the conduction band is from the 5s state of cadmium. The conduction band has quantum number Jz= ½. The valence band has three sub-bands with one having quantum number Jz =3/2 and the other two with Jz= ½. The band gap between the highest valence band and the conduction band at room temperature is ~1.75eV. When the materials dimension shrink below the bulk exciton Bohr radius, the effect of quantum confinement comes to play. The absorption wavelength begin to blue shift as the particle size of QDs decrease. A schematic representation of the band structure of bulk CdSe is given in Figure 2.1.

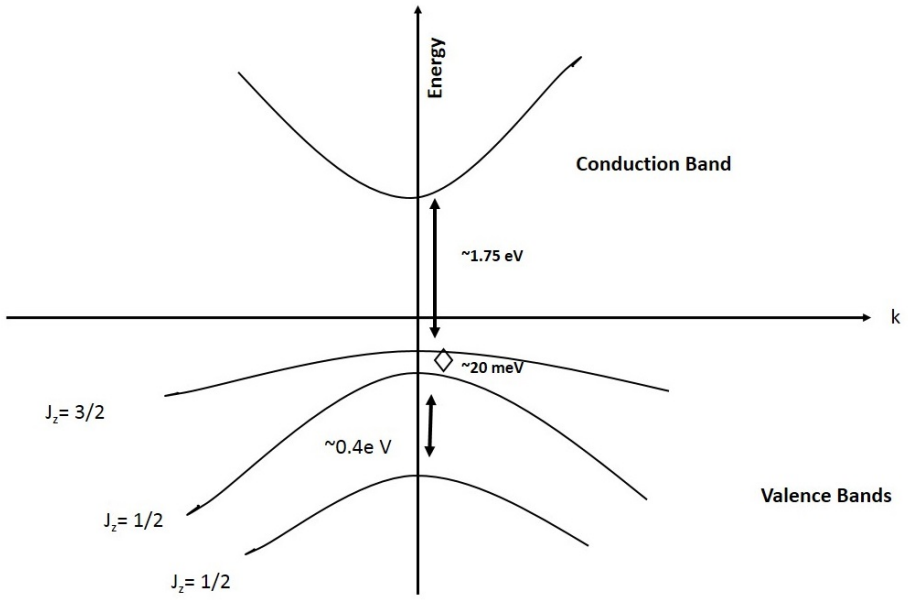

Figure 2.1: Schematic representation of Band structure of Bulk CdSe.

2.1.2 Optical transitions in CdSe Quantum dots

The confinement effects leads to the blue shifting of the band gap as the particle size of the QDs decreases. This can be compared to a particle in a spherical box. The energy of the particle E, is proportional to $1/a^2$, where 'a' is the radius of the box. As the size of the box shrinks, the energy of the particle increases (Balet et al., 2004). Unlike the bulk CdSe, CdSe QDs do not actually have energy bands, but they have quantized electron and hole states. In QDs, the conduction states originate from the cadmium 5s orbital and the valence state originates from selenium 4p orbital. The general electronic structure of CdSe quantum dot is given in Figure 2.2 (Jarosz, 2004).

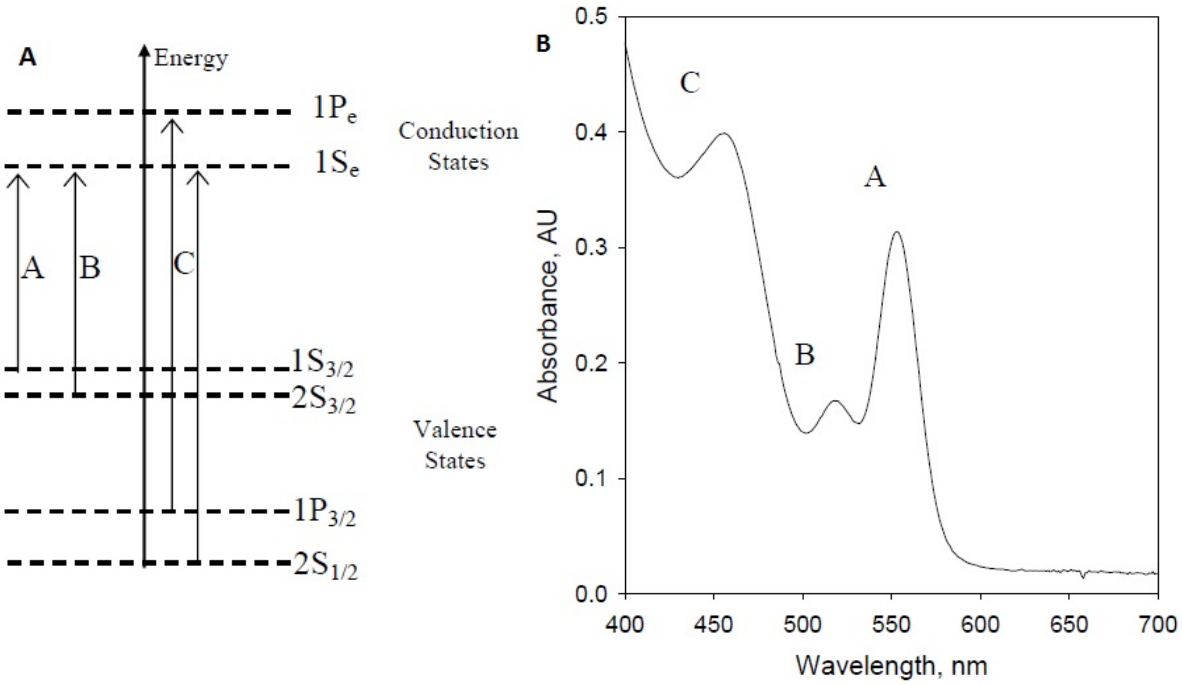

Figure 2.2: (A) Schematic representation approximating the energy level of CdSe quantum dots. (Not drawn to scale). (B) Absorption spectrum of CdSe quantum dots corresponding to the transitions indicated in (A) (Jarosz, 2004).

2.2 Core-shell Nanomaterials

Colloidal core-shell nanocrystals (CSNCs) generally contain at least two semiconductor materials in a layered structure. Growing an epitaxial-type shell of another semiconductor, in order to tune the basic optical properties like fluorescence wavelength, quantum yield and lifetime of the core nanocrystal has fueled significant progress in the chemical synthesis of these systems (Nanda et al., 2006). In such core-shell nanocrystals, the shell provides a physical barrier between the optically active core and the surrounding medium, thus making the nanocrystals less sensitive to environmental changes, surface chemistry, and photo-oxidation. The shell further provides an efficient passivation of the

surface trap states, giving rise to a strongly enhanced fluorescence quantum yield. This effect is a fundamental prerequisite for the use of nanocrystals in applications such as biological labeling and light-emitting devices, which rely on their emission properties (Wu et al., 2015).

A general requirement for the synthesis of CSNCs with satisfactory optical properties is epitaxial-type shell growth. Therefore an appropriate band alignment is not the sole criterion for the choice of materials but rather the core and shell materials should crystallize in the same structure and exhibit a small lattice mismatch (Ray et al., 2014). In the opposite case, the growth of the shell can result in strain and the formation of defect states at the core-shell interface or within the shell. These can act as trap states for photogenerated charge carriers and diminish the fluorescence quantum yield (Chen et al., 2003). Another factor which influence the final quality of the as-synthesised core shell material is the control of shell thickness. The precursors used for shell growth should have high reactivity and selectivity without any side reactions. If the shell is too thin, the passivation of the core NCs is inefficient and the photostability of the resulting core shell will be low. If the shell thickness is too high, the optical properties of the resulting CSNCs generally deteriorate as a consequence of strain induced by the lattice mismatch of the core and shell materials, accompanied by the generation of defect states.

Generally core-shell systems are fabricated in a two-step procedure. Initially, the synthesis of core NCs is done, followed by the shell growth reaction. During the shell growth step, a small number of monolayers (typically 1–5) of the shell material are deposited on the cores. The temperature for the shell growth (T_2) is generally lower than

the one used for the core NC synthesis (T_1) in order to prevent nucleation of the shell material and uncontrolled ripening of the core NCs (Fig.2). In addition, the shell precursors are slowly added, by means of a syringe pump. Figure 2.3 shows a schematic representation of the procedure.

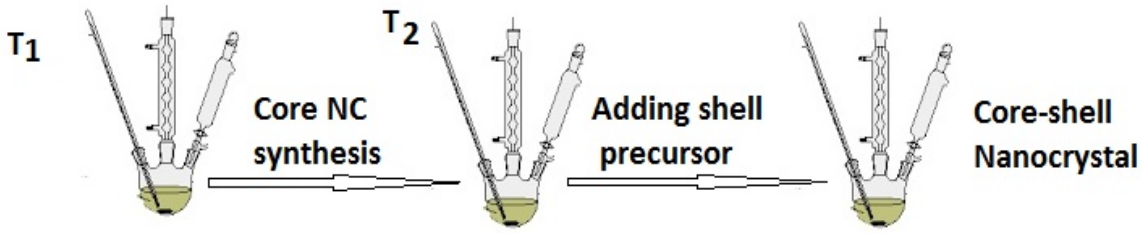

Figure 2.3: Schematic representation of Core- shell nanocrystal synthesis.

Depending on the bandgaps and the relative position of electronic energy levels of the involved semiconductors, the shell can have different functions in CSNCs. For the use of quantum dots in optical applications, it is very important to know the energy levels of the charge carriers confined within the dot, since this determines properties such as the absorption and emission spectra. CSQDs are grouped into two types based on the localization of electrons and holes within the structure. The two main categories are Type 1 and Type 11 core-shell materials. Figure 2.4 shows a schematic representation of energy level alignment of different core-shell systems.

.

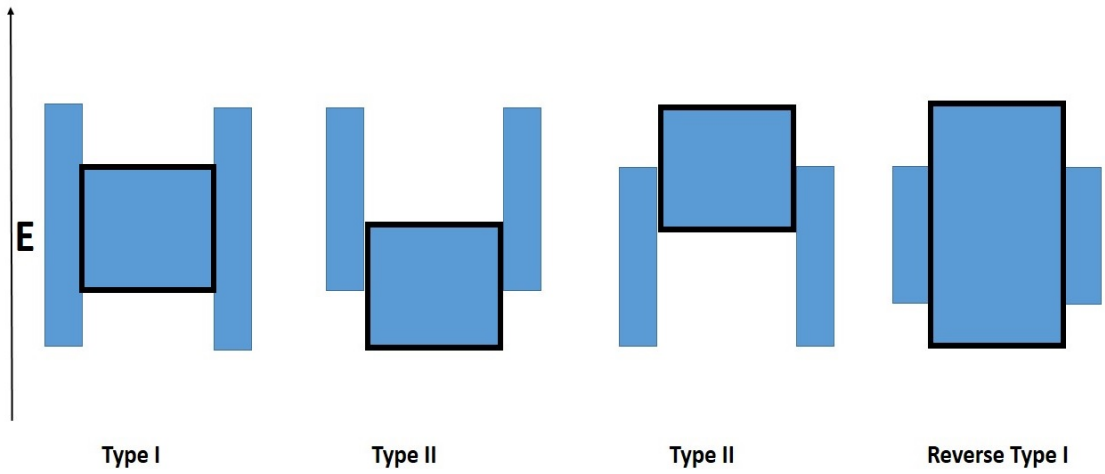

Figure 2.4: Schematic representation of the energy-level alignment in different core-shell systems realized with semiconductor NCs to date. The upper and lower edge of the rectangle corresponds to the positions of the conduction- and valence-band edge of the core (centre) and shell materials respectively.

2.2.1 Type I Core-shell materials

In Type-I, each carrier type is localized in a different section, meaning that the electrons and holes are spatially separated. In type-I CSNCs, the shell is used to passivate the surface of the core with the goal to improve its optical properties. In this CSQDs both electrons and holes are most likely to be found in the same section (either the core or shell). The shell of the NC physically separates the surface of the optically active core from its surrounding medium. Consequently, the sensitivity of the optical properties to changes in the local environment of the NCs' surface, induced, for example, by the presence of oxygen or water molecules, is reduced. With respect to core NCs, core-shell

systems exhibit generally enhanced stability against photodegradation. At the same time, shell growth reduces the number of surface dangling bonds, which can act as trap states for charge carriers and thereby reduce the fluorescence QY. The first published prototype system was CdSe/ZnS (Dabbousi et al., 1997). The ZnS shell significantly improves the fluorescence QY and stability against photobleaching. Shell growth is accompanied by a small red shift (5–10 nm) of the excitonic peak in the UV/Vis absorption spectrum and the photoluminescence (PL) wavelength. This is attributed to the partial leakage of the exciton into the shell material (Talapin et al., 2004).

2.2.2 Type II core-shell materials

In type-II systems, either the valence-band edge or the conduction band edge of the shell material is located in the bandgap of the core. In this system growing shell on the core cause a significant redshift of the emission wavelength of the NCs. The band alignment is staggered and it leads to a smaller effective bandgap than each one of the constituting core and shell materials. By manipulating the shell thickness, this systems can be tuned in such a way that the emission color moves towards spectral ranges, which are difficult to attain with other materials. For example Type- II NCs have been developed in particular for near-infrared emission using CdTe/CdSe or CdSe/ZnTe (Wang et al., 2014). Due to the lower overlap of the electron and hole wavefunctions, the PL life times of type II systems are longer than type I systems. To improve the fluorescence quantum yield and photostability of type II NCs, the core can be over coated with suitable shell materials like type I systems (Kim et al., 2004).

2.3 Metal Nanoparticles

Nanoparticles of metals have attracted scientists for over a century and are now heavily utilized in various nanotechnology based applications. Metal nanoparticles shows unique size and shape dependendent properties (Emory et al., 1998). The optical properties of these materials mainly arises from their surface plasmon resonance bands (SPR). Interest in understanding the science behind these materials have led to captivating research in the areas of optics, catalytic, electric and medical applications (Kim et al., 2007; Davarpanah & Kiasat, 2013; Theodorakosa et al., 2015).

Some features of metal nanoparticles can be described as follows;

1. large surface-area-to-volume ratio as compared to the bulk equivalents;
2. large surface energies
3. the transition between molecular and metallic states providing specific electronic structure (local density of states LDOS);
4. plasmon excitation;
5. quantum confinement;
6. short range ordering;
7. a large number of low-coordination sites such as corners and edges, having a large number of ″dangling bonds″ and
8. consequently specific and chemical properties and the ability to store excess electron

The fascination for this interesting materials have led to the research and development of various nanomaterials with different size, shapes, properties and applications.

Researchers are now capable of designing various nanomaterials based on different applications. Most of the chemical methods used for the synthesis of metal nanoparticles are too expensive and also involved with the use of toxic and hazardous chemicals that are responsible for various biological risks (Wang et al., 2005). The effluents after the synthesis also possess serious threat to ecosystem. In order to find a solution to this problem, the concept of green, eco-friendly synthesis was introduced (Raveendran et al., 2003). In this concept, most of the materials used for the synthesis of nanomaterials are environmental friendly and less or non-toxic. Various plant extracts, biopolymers, and reducing sugars were utilized to synthesis stable efficient nanoparticles (Anuj & Ishnava, 2013; Leung et al., 2010; Darroudi et al., 2011).

2.3.1 Silver nanoparticles

Among various metal nanoparticles, silver nanoparticles has gained more attention due to its good antibacterial activity and easy availability (Guzman et al., 2012). Silver nanoparticles are the particles of silver, with particle size between 1 and 100 nm. Ionic silver has a long history and was initially used to stain the glass to produce yellow coloured glass. Typically, they are synthesized by the reduction of a silver salt with a reducing agent like sodium borohydride in the presence of a colloidal stabilizer (Pastoriza-Santos & liz-Marzan, 1999). The most common colloidal stabilizers used are polyvinyl alcohol, poly (vinylpyrrolidone) (Yan et al., 2009), bovine serum albumin (BSA) (Gautam et al., 2013), citrate (Bastus et al., 2014), and cellulose (Lokanathan et al., 2014). Many methods can be used to synthesize Ag-NPs, including chemical reduction (Wang et al., 2005), micro emulsion (Solanki & Murthy, 2011), γ-Ray (Rao et al., 2010),

UV-irradiation (Darroudi et al., 2009), microwave irradiation (Yin et al., 2004), ultrasonication (Wani et al., 2011) and spray pyrolysis (Kim et al., 2006).

Polymers have also been used as matrices in nanocomposites or as stabilizers to provide stability for the metal nanoparticles against oxidation, agglomeration, and precipitation (Lin et al., 2009). Preparations of Ag-NPs in various polymers such as polyvinylpyrrolidine (PVP) (Zheng et al., 2001), polyethylene glycol (Luo et al., 2005), poly(methyl methacrylate) (Singh & Khanna, 2007), poly (vinyl alcohol) (Zhou et al., 1999), polyaniline (Khanna et al., 2005), PMMA (Majumder et al., 2011) and polyacrylonitrile (PAN) (Zhang et al., 2001) have been published to give well-dispersed Ag-NPs. Natural polymers have also been used because they are non-toxic and biocompatible. For example, natural rubber (Abu Baker et al., 2007), polysaccharides (Huang et al., 2010), cellulose (Cai et al., 2009), chitosan (Huang et al., 2004), gelatin (Mohan et al., 2014) and starch (Raveendran et al., 2003) have been used as matrices or stabilizers for the preparation of metallic nanoparticles. In order to introduce complete green synthesis protocols for the reduction, environmental friendly reducing agents like β-d-glucose, starch, plant extracts e.t.c are now been used to produce silver nanoparticles. The use of biopolymers, plant metabolites, microorganisms e.t.c instead of toxic reducing reagents like citrates, borohydrides, ammonia e.t.c have highly reduced the negative impact of these materials and its effluents on the environment.

Nanosilver has many important applications. One of the most established use of nanosilver is as an antimicrobial agent. Currently, the investigation of this phenomenon has regained importance due to the increase of bacterial resistance to antibiotics, caused

by their overuse (Rodriguez-Mozaza et al., 2015). This property of nanosilver is effectively utilized in textiles, home water purification systems, medical devices, cosmetics, electronics, and household appliances (Kholoud et al., 2010). Antibacterial activity of the silver-containing materials can be used in medicine to reduce infections in burn treatment (Adhya et al., 2015), arthroplasty (Brennan et al., 2015), to prevent bacteria colonization on prostheses (Murphy et al., 2015), catheters (Ge et al., 2014), vascular grafts (Chudobova et al., 2013), dental materials (Garcia-Contreras et al., 2011), human skin (DeLouise, 2012), e.t.c. Research are also progressing to incorporate silver nanoparticles into a wide range of medical devices, including bone cement, surgical instruments, surgical masks, e.t.c (Prokopovich et al., 2013). Moreover, due to their attractive physiochemical properties these nanomaterials have received considerable attention in biomedical imaging using surface enhanced Raman scattering (SERS). The surface plasmon resonance and large effective scattering cross-section of individual silver nanoparticles make them ideal candidates for molecular labeling (Tauran et al., 2013). Because of strong optical features, silver nanoparticles are useful for biological sensing and imaging applications (Schrand et al., 2008; Ragacheva et al., 2015). Due to their high conductivity, silver nanoparticles are applied in conductive inks, adhesives and pastes for a range of electronic devices (Zhou et al., 2014; Xu et al., 2015). Silver nanoparticles are also used as catalysts in several chemical reactions such as reduction of environmental pollutants like nitrophenol, methylene blue dye e.t.c (Naraginti & Sivakumar, 2014; Dua et al., 2015).

2.4 Polymer nanocomposites

The composite is a material which mainly contains two components; major component the ‘matrix’ and the minor component the ‘filler’. When the matrix is a polymer and the filler is a nanomaterial, the material is termed as polymer nanocomposite (Paula & Robeson, 2008). The filler act as a reinforcement in the matrix and it gives unique properties to the composite based on the desired application. Polymers due to their physical properties like light weight and flexibility, compared to other matrices like metals and ceramics, are one of the most widely used matrix material in composites for high end applications. With respect to many inorganic materials, polymer matrices have the potential to offer improved production rates, lower cost, and improved processability. In order to improve the strength, toughness, electrical conductivity, thermal stability e.t.c of the polymers, various fillers are added to prepare desired polymer nanocomposites based on different applications.

The addition of inorganic spherical nanoparticles to polymers allows the modification of the polymers physical properties as well as the implementation of new features in the polymer matrix. Such extremely small particles possess only poor “compacting properties”. Considering the system as an ideal case and assuming that the monomodal spherical nanoparticles with no friction, no van-der Waals forces and no agglomeration between a cubic face centered arrangement of particles; a maximum filling degree of 74 vol % can be obtained for a composite. In reality, the filling degree will always be significantly lower. Among all the established main material classes of metals, ceramics and polymers composites, especially polymer-matrix composites (PMC) allow high flexibility for a physical property tailoring using different type of fillers (Zare, 2015).

Depending on the particle size, shape, specific surface area and chemical nature of the matrix and the fillers, the polymer composites shows improved properties. Some of the properties of the polymer matrix that can be modified are:

1. electrical and thermal conductivity
2. polymer phase behavior and thermal stability
3. mechanical properties like stiffness, Young's modulus, wear, fatigue, and others
4. flame retardancy
5. density
6. Physical properties such as magnetic, optic, or dielectric properties.

This modification of matrix properties are highly significant when it comes to the application of these materials.

2.4.1 Light emitting polymer nanocomposites

The development of energy-efficient devices that generate white light is in high demand in the optical and electronic industry. The development of efficient full colour displays and solid state light emitting devices are still major challenges in the communication and information, and lighting industries. Recently, the focus is on developing full colour displays made of red, green blue (RGB) light emitting diodes (LEDs) or white LED illumination systems, which are energy-efficient. Significant improvements have been made in developing group III–V semiconductor based bright long-lived blue light emitting diodes (Kneissl et al., 2011) and blue laser diodes (Li et al., 2013). However, developing full colour displays from InGaN-based LEDs is rather limited by the difficulty of controlling the concentration and a complex fabrication processes.

The incorporation of light-emitting nanocrystals in polymers allows one to combine the ease of processing and structural flexibility of organic materials, with the optical and thermal stability shown by the luminescence of inorganic fillers. Nano patterning of light-emitting organic–inorganic composites and shaping them to obtain fluorescent nanostructures and fibers often remain important challenges in order to employ these materials in nanocomposite-based optoelectronic devices. To overcome this problem. the nano-complexes should be incorporated into some flexible matrix which has good optical transparency, physical and chemical stability, tunable mechanical properties and easy molding.

Compared to conventional quartz fibers, plastic fibers have many advantages such as high flexibility, low weight and low cost (Pujadas et al., 2014). Semiconductor nanocrystals (quantum dots, QDs) show unique optical and electronic properties which includes; strong extinction coefficient, high quantum yield and tunable emission profile by changing the size of particles (Sanusi & Nyokong, 2014). Combining the properties of polymers and QDs, novel optoelectronic devices, such as LEDs (Light Emitting Diodes), fibers and fiber amplifiers can be developed (Kramer & Sargent, 2011; Gordillo et al., 2011). It is already reported that the QDs doped fiber amplifiers (using usual SiO_2 glass) are endowed with broader bandwidth and lower noise compared with conventional erbium doped fiber amplifiers (Wu et al., 2008; Chao et al., 2008). Among the various QDs, CdSe QDs with high PL quantum efficiency is favorable for optoelectronic devices (Purohita et al., 2015).

2.5 Applications of nanomaterials.

Nanomaterials have already marked their presence in almost all applications of our day to day activities. This include but not limited to improving material strength, performance of batteries, solar cells, water filtration, nanomedicine, nanocatalysis, pollution control, sensing, nanoelectronics, automobile industry and so on.

2.5.1 Light emitters

Application of optical imaging in basic life science research and clinical diagnostics have become highly significant because of its noninvasive, rapid, highly sensitivity and inexpensive nature (Wu et al., 2010). Many cutting-edge imaging technologies have emerged with the aim of increasing the resolution of optical imaging in order to improve the final result. The recent developments in luminescent nanoparticles (NPs) with unique optical properties have shown new roads for fluorescence imaging and sensing as well as for *in vitro* and *in vivo* labeling in cells, tissues, and organisms (Tonga & Cheng, 2011). QDs are becoming an important class of biomaterials because they possess unique optical properties when compared to organic dyes or fluorescent proteins (Zha & Zeng, 2015). They are characterized by a broad excitation range, a narrow emission peak, ultrahigh brightness, greater chemical stability, and resistance to photobleaching (Kobayashi et al., 2010). In addition, QDs have similar quantum yields but extinction coefficients that are 10−50 times larger and significantly more reduced photobleaching rates. The overall effect is that QDs have 10−20 times brighter fluorescence and 100−200 times better photostability. Another advantage of QDs is that, they can emit in NIR region for in vivo imaging with better fluorescence lifetime when compared with organic fluorophores (Zhang et al., 2012).

Sensitive detection of target analytes present at trace levels in biological samples often requires labeling of reporter molecules with fluorescent dyes. However, it can be difficult to reach a low detection limit in fluorescence detection due to the limited extinction coefficients or quantum yields of traditional organic dyes and also low dye-to-reporter molecule labeling ratio. The recent explosion of nanotechnology, leading to the development of materials with submicrometer-sized dimensions and unique optical properties, has opened up new horizons for fluorescence detection. Nanomaterials can be made from both inorganic and organic materials and are less than 100 nm in length along at least one dimension.

2.5.2 Photovoltaics

In order to solve the major issue of energy crisis, solar energy, one of the cleanest energy is regarded as a major solution. Advances in nanomaterial synthesis have led to the development of solar cells that can potentially combine high efficiency with lower production costs than conventional cells (Choi et al., 2013). The dye sensitized solar cell was first demonstrated in 1991 by O'Regen and Grätzel. Quantum dot sensitized solar cells (QDSSCs) are a modified version of this design with more efficiency in which colloidal quantum dots (QDs) replace the organic dye (Alexander et al., 2012). A number of the properties of QDs make them well-suitable as photoabsorber particularly their band gap that can often be size-tuned to optimize exploitation of the solar spectrum. They exhibit multiple exciton generation with high photostability and highly absorbing nature (Ellingson et al., 2005). Quantum dots can also be used to replace the electrolyte as the hole-transporting medium (McElroy et al., 2014).

Many latest reports shows the improved cell efficiency of quantum dot-sensitized solar-cells (QDSSCs) (Kouhnavard et al., 2014; Jun et al., 2013; Tian & Cao, 2013). A wide variety of QDs have been investigated as sensitizers for QDSSCs, because of their tunable band gap energy, high extinction coefficients and large dipole moment. The most commonly used are CdSe (Gao et al., 2014), PbS (Sung et al., 2013), CdTe (Badawi et al., 2013), SnS (Tsukigase et al., 2011), CdS (Wang et al., 2013) and Sb_2S_3 (Li et al., 2013). These materials are usually coupled with metal oxide entities to improve the efficiency of the solar cells (Pralay & Prashant, 2012). Reports have suggested that coupled QDs-sensitized solar cells systems are advantageous over single QDs-sensitized cells due to their enhanced photocurrent generation (Cheng et al., 2015; Huang & Zou, 2015).

Many researches are now focused on co-sensitized solar cells with CdS / CdSe QDs for their strong visible light harvesting ability and high carrier migrating speed (Zhang et al., 2012). CdSe QDs have wider absorption scope (k < 730 nm) (Jun et al., 2013), and CdS QDs are stronger oxidizers to gain electrons from electrolyte. Coupled together, CdS/CdSe QDs can ensure in theory high photoelectric conversion efficiency at full visible light spectrum (Cheng et al., 2012). Hybrid systems like CdS–CdSe and CdS–CdTe core–shell quantum dots sensitized TiO_2 nanotube array solar cells (Li et al., 2011), CdSe in P3HT:PCBM layer (Park et al., 2014) e.t.c have shown high efficiency compared to their old counterparts.

2.5.3 Catalytic applications

Nanomaterials especially metal nanoparticles due to their high surface energy shows good catalytic properties. Nanomaterials like ZnS shows excellent photocatalytic activity and act as excellent photocatalyst for the photocatalytic degradation of organic pollutants such as dyes, p-nitrophenol and halogenated benzene derivatives in wastewater treatment (Mansur et al., 2014). Metal nanoparticles are also excellent catalyst for the degradation of environmental pollutants (Narayanan & Sakthivel, 2011). Silver nanoparticles shows good catalytic activity in the reduction of aromatic nitro compounds, dyes (Vanaja et al., 2014) etc.

2.5.4 Sensing

The development of suitable sensors for monitoring production process and effluents is a major challenge faced by the industry. Environmental pollution caused by heavy metal ions (Hg^{2+}, Cd^{2+}, As^{3+}, Pb^{2+}, e.t.c.), toxic gases (SO_2, NO_x, HCl, e.t.c.), organophosphorus (OP) compounds (pesticides and insecticides), and industrial and domestic wastewater (phenol, H_2O_2), can directly or indirectly damage and impact the ecosystem and greatly threaten the environmental security and human health (Yang et al., 2013). Therefore, in order to monitor and clear away these toxic substances in air, water and soil it is necessary to develop inexpensive, sensitive, selective, and simple detection methods and devices.

Fluorescent quantum dots have shown some promising results in the sensing of various enzymes and reagents. The CdSe- ZnS CSQDs when conjugated with different enzymes like glucose oxidase and horseradish peroxidase served as FRET probes to sense glucose

(Doung et al., 2007). The mechanism for the sensing process involved the conversion of glucose to glucose oxidase by a redox reaction using the electron donated by CSQDs. The CSQDs fluorescence quenching corresponds to the concentration of glucose. Another example is the analysis of H_2O_2, and urea by the luminescence quenching of (CdSe) ZnS CSQD (Gill et al., 2008). CSQDs have also been demonstrated to be effective pH sensors. The unique size-dependent optical properties of Ag-NPs has led to their applications as sensing materials for many chemical and biological compounds. Various toxic compounds like urea, nitro phenol, H_2O_2, heavy metals e.t.c can be detected by using the localized surface plasmon resonance (LSPR) property of silver nanoparticles (Filippo et al., 2009; Anbazhagan et al., 2014) .

2.6 Brief outline of the thesis

The thesis is subdivided into six chapters:

Chapter 1 gives a general overview about nanotechnology and the physics behind nanomaterials. The reasons why nanomaterials are unique and the factors which makes them different from other dimensional materials are also discussed. The aims and objectives of the thesis are presented in this chapter.

Chapter 2 provides detailed literature review about quantum dots and metal nanoparticles. It explains the concept of quantum confinement and electronic band structure of CdSe. The concept of core-shell nanomaterials and its various classifications are also explained in this section. Importance of metal nanoparticles specifically silver nanoparticles are also explained followed by their various applications in the field of sensing, catalytic property and biomedical field.

Chapter 3 describes the synthesis and characterization of various core-shell QD polymer nanocomposites. The optical and morphological characterizations of the as-synthesized nanoparticles and composites are investigated. Raman spectroscopic analysis of the as synthesized core-shell QDs were done to confirm the formation of the core-shell structure. Brillouin spectroscopy analysis of the QD polymer composite revealed the effect of QDs on the mechanical property of the polymer nanocomposite. The fluorescent property of the polymer matrix was improved by the addition of QDs. Fluorescent water soluble QDs were also synthesized and characterized using a simple ligand exchange method.

The synthesis and characterization of biopolymer capped Ag-NPs is explained in chapter 4. Detailed optical, morphological, antibacterial, toxicity analysis and sensing properties of the Ag-NPs were investigated. Compared to starch capped Ag-NPs, gelatin capped Ag-NPs showed better MIC and MBC values against different bacteria.

Chapter 5 focusses on various applications of the as synthesized Ag-NPs. The synthesis and characterization of silver functionalized MWCNTs via a simple and facile method using biodegradable and biocompatible reagents were discussed. Detailed optical, morphological, antibacterial and catalytic property analysis of the hybrid system was done. Both Ag-NPs showed good sensing activity against H_2O_2 even at very smaller concentration of 10^{-10} M. The as-synthesized material can be explored for other applications like catalytic, tissue engineering etc.

Finally, brief conclusions and future work are given in Chapter 6.

Reference

Abu Bakar, N.H.H., Ismail, J. & Abu Bakar, M. 2007. Synthesis and characterization of silver nanoparticles in natural rubber. *Mater. Chem. Phys*., 104 (2-3): 276–283.

Adhya, A., Bain, J., Ray, O., Hazra, A., Adhikari, S., Dutta, G., Ray,S. & Majumdar, B.K. 2015. Healing of burn wounds by topical treatment: A randomized controlled comparison between silver sulfadiazine and nano-crystalline silver. *J Basic Clin Pharm*., 6(1): 29–34.

Alexander H. Ip, Thon, S.M., Hoogland, S., Voznyy, O., Zhitomirsky, D., Debnath, R., Levina, L., Rollny, L.R., Carey, G.H., Fischer, A., Kemp, K.W., Kramer, I.J., Ning, Z., Labelle, A.J., Chou, K.W., Amassian, A. & Sargent, E.H. 2012. Hybrid passivated colloidal quantum dot solids. *Nat. Nanotechnol*., 7: 577-582.

Anbazhagan, V., Ahmed, K.B.A. & Janani, S. 2014. Synthesis of catalytically active silver nanoparticles using lipid derived signaling molecule, N-steroylethanolamine: Promising antibacterial agent and selective colorimetric sensor for mercury ion. *Sens. Actuators, B,* 200: 92–100.

Anuj, S.A. & Ishnava, K.B. 2013. Plant mediated synthesis of silver nanoparticles by using dried stem powder of Tinospora Cordifolia , its antibacterial activity and comparison with antibiotics. *Int J Pharm Bio Sci.,* 4: 849–863.

Badawi, A., Al-Hosiny, N., Abdallah, S., Negm, S. & Talaat, h. 2013. Tuning photocurrent response through size control of CdTe quantum dots sensitized solar cells. *Solar Energy,* 88: 137–143

Balet, L. P., Ivanov, S. A., Piryatinski, A., Achermann, M. & Klimov, V. I. 2004. Inverted core/shell nanocrystals continuously tunable between type-I and type-II localization regimes. *Nano Lett.,* 4(8): 1485 – 1488.

Balkanski, M & Wallis, R. F. 2000. Semiconductor Physics and Applications, Oxford University Press.

Bastús, N.G., Merkoçi, F., Piella, J. & Puntes, V. 2014. Synthesis of highly monodisperse citrate-stabilized silver nanoparticles of up to 200 nm: kinetic control and catalytic properties. *Chem. Mater*., 26 (9):2836–2846.

Bowers II, M. J., McBride, J. R. & Rosenthal, S. J. 2005. White-light emission from magic-sized cadmium selenide nanocrystals. *J. Am. Chem. Soc*., 127(44):15378 – 15379.

Brennan, S.A., Fhoghlú, C.N., Devitt, B.M., Mahony, F.J.O., Brabazon, D. & Walsh, A. 2015. Silver nanoparticles and their orthopaedic applications. *Bone Joint J* ,97-B(5): 582-589.

Cai, J., Kimura, S., Wada, M. & Kuga, S. 2009. Nanoporous cellulose as metal nanoparticles support. *Biomacromolecules,* 10(1): 87–94.

Chang, L. L., Esaki, L. & Tsu, R. 1974. Resonant tunneling in semiconductor barriers. *Appl. Phys. Lett*., 24(12): 593 – 595.

Chao, L., Jong, H., Xianghua, Z. & Adam, J. L. 2008. Photoluminescence of PbS quantum dots embedded in glasses. *J. Non Cryst. Solids,* 354: 618–623.

Chen, X.B., Lou, Y.B., Samia, A.C. & Burda, C. 2003. Coherency strain effects on the optical response of core/shell heteronanostructures. *Nano Lett*., 3:799–803.

Cheng, H.M., Huang, K.Y., Lee, K.M., Yu, P., Lin, S.C., Huang, J.H., Wu, C.G. & Tang, J. 2012. High-efficiency cascade CdS/CdSe quantum dot-sensitized solar cells based on hierarchical tetrapod-like ZnO nanoparticles. *Phys. Chem. Chem. Phys*., 14: 13539-13548.

Cheng, K., Wu, Y., Meng, J., Zhao, Y., Wang, X., Du, Z. 2015. Plasmon-enhanced photocurrent generation in quantum dots-sensitized solar cells by coupling of gold nanocrystals. *Science Bulletin,* 60(5): 541-548.

Choi, H., Nahm, C., Kim, J., Kim, C., Kang, S., Hwang, T. & Park, B. 2013. Toward highly efficient quantum-dot- and dye-sensitized solar cells. Curr. Appl. Phys. 13: S2–S13.

Chudobova, D., Nejdl, L., Gumulec, J., Krystofova, O., Angel, M., Rodrigo, M., Kynicky, J., Ruttkay-Nedecky, B., Kopel, P., Babula, P., Adam, V. & Kizek, R. 2013. Complexes

of silver (I) ions and silver phosphate nanoparticles with hyaluronic acid and/or chitosan as promising antimicrobial agents for vascular grafts. *Int J Mol Sci*., 14(7): 13592–13614.

Dabbousi, B.O., Rodriguez-Viejo, J., Mikulec, F.V., Heine, J.R., Mattoussi, H., Ober, R., Jensen, K.F. & Bawendi, M.G. 1997. (CdSe)ZnS Core−Shell quantum dots: synthesis and characterization of a size series of highly luminescent nanocrystallites. *J. Phys. Chem. B*, 101(46): 9463-9475.

Darroudi, M., Ahmad, M.B., Abdullah, A.H. & Ibrahim, N.A. 2011. Synthesis and characterization of UV-irradiated silver/montmorillonite nanocomposites. *Int. J Nanomedicine*, 6(1): 569–574.

Darroudi, M., Ahmad, M.B., Shameli, K., Abdullah, A.H. & Ibrahim, N.A. 2009. Synthesis and characterization of UV-irradiated silver/montmorillonite nanocomposites. *Solid State Sci*., 11: 1621–1624.

Davarpanah, J. & Kiasat, A.R. 2013. Catalytic application of silver nanoparticles immobilized to rice husk-SiO2-aminopropylsilane composite as recyclable catalyst in the aqueous reduction of nitroarenes. *Catal. Commun.*, 41: 6–11.

DeLouise, L.A. 2012. Applications of Nanotechnology in Dermatology. *J Invest Dermatol.*, 132: 964–975.

Dingle, R., Gossard, A. C. & Wiegmann, W. 1974. Direct observation of superlattice formation in a semiconductor heterostructure. *Phys. Rev. Lett*., 33(14): 827 – 830.

Dua, L., Xua, Q., Huanga, M., Xiana, L. & Feng, J. 2015. Synthesis of small silver nanoparticles under light radiation by fungus Penicillium oxalicum and its application for the catalytic reduction of methylene blue. *Mater. Chem. Phys*., 160: 40–47.

Duong, H.D. & Rhee, J.I. 2007. Use of CdSe/ZnS core-shell quantum dots as energy transfer donors in sensing glucose. *Talanta*, 73(5):899-905.

Ekimov, A. I. 1981. Quantum size effect in three-dimensional microscopic semiconductor crystals. *JETP Lett*., 34(6): 345 – 349.

Ellingson, R.J., Beard, M.C., Johnson, J.C., Yu, P., Micic, O.I., Nozik, A.J., Shabaev, A. & Efros, A.L. 2005. Highly efficient multiple exciton generation in colloidal PbSe and PbS quantum dots. *Nano Lett*., 5(5): 865-871.

Emory, S.R., Haskins, W.E. & Nie, S. 1998. Direct observation of size-dependent optical enhancement in single metal nanoparticles. *J. Am. Chem. Soc*., 120: 8009-8010.

Filippo, E., Serra, A. & Manno, D. 2009. Poly(vinyl alcohol) capped silver nanoparticles as localized surface plasmon resonance-based hydrogen peroxide sensor. *Sens. Actuators, B,* 138: 625-630.

Fisher, B. R., Eisler, H. J., Stott, N. E. & Bawendi, M. G. 2004. Emission intensity dependence and single-exponential behavior in single colloidal quantum dot fluorescence lifetimes. *J. Phys. Chem. B,* 108 (1): 143–148.

Gao, B., Shen, C., Yuan, S., Zhang, B., Zhang, M., Yang, Y. & Chen, G. 2014. Influence of nanocrystal size on the quantum dots sensitized solar cells' performance with low temperature synthesized CdSe quantum dots. *J. Alloys Compd*., 612: 323–329.

García-Contreras, R., Argueta-Figueroa, L., Mejía-Rubalcava, C., Jiménez-Martínez, R., Cuevas-Guajardo, S., Sánchez-Reyna, P.A. & Mendieta-Zeron, H. 2011. Perspectives for the use of silver nanoparticles in dental practice. *Int Dent J*, 61(6):297-301.

Gautam, S., Dubey, P. & Gupta, M.N. 2013. A facile and green ultrasonic-assisted synthesis of BSA conjugated silver nanoparticles. *Colloids Surf.,B,* 102: 879–883.

Ge, L., Li, Q., Wang, M., Ouyang, J., Li, X. & Xing, M.M.Q. 2014. Nanosilver particles in medical applications: synthesis, performance, and toxicity. *Int J Nanomedicine*, 9: 2399–2407.

Gill, R., Bahshi, L., Freeman, R. & Willner, I. 2008. Optical detection of glucose and acetylcholine esterase inhibitors by H_2O_2-sensitive CdSe/ZnS quantum dots. *Angew. Chem*., 120:1700–1703.

Gordillo, H., Surez, I., Abargues, R., Rodríguez-Cantó, P., Albert, S. & Mart´ınez Pastor, J.P. 2011. Polymer/QDs Nanocomposites for waveguiding applications. *Nanotechnology*, 22, Article ID 435202: 43

Guzman, M., Dille, J. & Godet, S. 2012. Synthesis and antibacterial activity of silver nanoparticles against gram-positive and gram-negative bacteria. *Nanomedicine: Nanotechnology, Biology and Medicine*, 8(1):37–45.

Huang, H., Yuan, Q. & Yang, X. 2004. Preparation and characterization of metal-chitosan nanocomposites. *Colloid Surf., B,* 39(1-2): 31–37.

Huang, N.M., Lim, H.N., Radiman, S., Khiew, P.S., Chiu, W.S., Hashim, R. & Chia, C.H. 2010. Sucrose ester micellar-mediated synthesis of Ag nanoparticles and the antibacterial properties. *Colloid Surf., A*, 353(1): 69–76.

Huang, Z. & Zou, X. 2015. Superior Photocurrent of Quantum Dot Sensitized Solar Cells Based on PbS : In/CdS Quantum Dots. *Int J Photoenergy,* Article ID 657871: 9.

Jarosz, M. (2004). The physics and Chemistry of transport in CdSe quantumdots solids, PhD thesis, Massachusetts Institute of Technology.

Jun, H. K., Careem, M. A. & Arof, A. K. 2013. Quantum dot-sensitized solar cells—perspective and recent developments: A review of Cd chalcogenide quantum dots as sensitizers. *Renew. Sustain. Energy Rev*., 22:148–167.

Khanna, P.K., Singh, N., Charan, S. & Viswanath, A.K. 2005. Synthesis of Ag/polyaniline nanocomposite via an in situ photo-redox mechanism. *Mater. Chem. Phys*., 92: 214–219.

Kholoud, M.M., El-Noura, A., Eftaihab, A., Al-Warthanb, Ammarb, R.A.A. 2010. Synthesis and applications of silver nanoparticles. *Arab J Chem*., 3(3): 135–140.

Kim, H. S., Lee, K. H. & Kim, S. G. 2006. Growth of monodisperse silver nanoparticles in polymer matrix by spray pyrolysis. *Aerosol. Sci. Tech*., 40: 536–544.

Kim, J.S., Kuk, E., Yu, K.N., Kim, J.H., Park, S.J., Lee HJ, Kim S. H., Park, Y.K., Hwang, C.Y., Kim, Y. K., Lee, Y. S., Jeong, D. H., Cho, M. H. 2007. Antimicrobial effects of silver nanoparticles. *Nanomedicine: Nanotechnology, Biology and Medicine,* 3 (1): 95-101.

Kim, S., Fisher, B., Eisler, H. J. & Bawendi, M. 2003. Type-II quantum dots: CdTe/CdSe (core/shell) and CdSe/ZnTe (core/shell) heterostructures. J. Am. Chem. Soc., 125 (38): 11466 – 11467.

Kim, S., Lim, Y.T., Soltesz, E.G., Grand, A.M., Lee, J., Nakayama, A., Parker, J.A., Mihaljevic, T., Laurence, R.G., Dor, D.M., Cohn, L.H., Bawendi, M.G. & Frangion, J.V. 2004. Near-infrared fluorescent type II quantum dots for sentinel lymph node mapping. *Nature Biotechnology*, 22: 93 – 97.

Kneissl, M., Kolbe, T., Chua, C., Kueller, V., Lobo, N., Stellmach, J., Knauer, A., Rodriguez, H., Einfeldt, S., Yang, Z., Johnson, N.M. & Weyers, M. 2011. Advances in group III-nitride-based deep UV light-emitting diode technology. *Semicond. Sci. Technol*., 26: 014036.

Kobayashi, H., Ogawa, M., Alford, R., Choyke, P.L. & Urano, Y. 2010. New strategies for fluorescent probe design in medical diagnostic imaging. *Chem Rev*., 110(5): 2620–2640.

Kouhnavard, M., Ikeda, S., Ludin, N.A., Ahmad Khairudin, N.B., Ghaffari, B.V., Mat-Teridi, M.A., Ibrahim, M.A., Sepeai, S. & Sopian, K. 2014. A review of semiconductor materials as sensitizers for quantum dot-sensitized solar cells. *Renew sust energy rev.*, 37: 397–407.

Kramer, I.J. & Sargent, E.H. 2011. Colloidal quantum dot photovoltaics: a path forward. *ACS Nano*, 5(11) : 8506–8514.

Leung, T. C.Y., Wong, C. K. & Xie, Y. 2010. Green synthesis of silver nanoparticles using biopolymers, carboxymethylated-curdlan and fucoidan. *Mater. Chem. Phys*., 121 (3): 402-405.

Li, S.G., Gong, Q., Cao, C.F., Wang, X.Z., Yan, J.Y., Wang, Y. & Wang, H.L. 2013. The developments of InP-based quantum dot lasers. *Infrared Physics & Technology*, 60: 216–224.

Li, Y., Wei, L., Zhang, R., Chen, Y., Mei, L. & Jiao, J. 2013. Annealing effect on Sb2S3-TiO2 nanostructures for solar cell applications. *Nanoscale Res. Lett*., 8:89.

Li, Z.X., Xie, Y.L., Xu, H., Wang, T.M., Xu, Z.G. & Zhang, H.L. 2011. Expanding the photoresponse range of TiO2 nanotube arrays by CdS/CdSe/ZnS quantum dots co-modification. *J. Photochem. Photobiol*., A 224: 25–30.

Lin, C. A., Tsai, H. C. & Tung, C. C. 2009. Preparation of silver nanoparticles/pseudo-thermoplastic polyvinyl alcohol (PT-PVA) films by the synchronous chemical reduction method. *Polym.-Plast.Technol*., 48: 1171–1175.

Lokanathan, A.R., Uddin, K.M. & Rojas, O.J. & Laine, J. 2014. Cellulose nanocrystal-mediated synthesis of silver nanoparticles: role of sulfate groups in nucleation phenomena. *Biomacromolecules*, 15(1): 373-379.

Luo, C., Zhang, Y., Zeng, X., Zeng, Y. & Wang, Y. 2005. Formation of calcium crystallites in dry natural rubber particles. *J. Colloid Interf. Sci*., 288: 444–448.

Majumder, M., Chakraborty, A.K., Biswas, B., Chowdhury, A. & Mallik, B. 2011. Indication of formation of charge density waves in silver nanoparticles dispersed poly (methyl methacrylate) thin films. *Synthetic Metals*, 161(13–14): 1390–1399.

Mansur, A.P.A., Mansur, H.S., Ramanery, F.P., Oliveira, L.C. & Souza, P.P. 2014. "Green" colloidal ZnS quantum dots/chitosan nano-photocatalysts for advanced oxidation processes: Study of the photodegradation of organic dye pollutants. *Appl. Catal., B*, (158–159):269–279.

McElroy, N., Page, R.C., Espinbarro-Valazquez, D., Lewis, E., Haigh, S., O' Brien, P. & Binks, D.J. 2014. Comparison of solar cells sensitised by CdTe/CdSe and CdSe/CdTe core/shell colloidal quantum dots with and without a CdS outer layer. *Thin Solid Films*, 560: 65–70.

Michalet, X., Pinaud, F. F., Bentolila, L. A., Tsay, J. M., Doose, S, Li, J. J., Sundaresan, G., Wu, A. M., Gambhir, S. S. & Weiss, S. 2005. Quantum dots for live cells, in vivo imaging, and diagnostics. *Science*, 307(5709): 538 – 544.

Mohan, S., Oluwafemi, S.O., George, S.C., Jayachandran, V.P., Lewu, F.B., Songca, S.P., Kalarikkal, N. & Thomas, S. 2014. Completely green synthesis of dextrose reduced silver nanoparticles, its antimicrobial and sensing properties. *Carbohydr. Polym*., 106: 469-474.

Mokhoff, N. 2006. MIT Spinoff Demos Quantum Dot Display Technology. EE Times.

Motohisa, J., Kamakura, K., Kishida, M., Yamazaki, T., Fukui, T., Hasegawa, H. & Wada, K. 1995. Fabrication of GaAs/AlGaAs quantum dots by metalorganic vapor phase epitaxy on patterned GaAs substrates. *J. Appl. Phys.*, 34:1098 – 1101.

Murphy, M., Ting, K., Zhang, X., Soo, C. & Zheng, Z. 2015. Current development of silver nanoparticle preparation, investigation, and application in the field of medicine. *J Nanomaterials*, 2015 (2015), Article ID 696918: 12.

Nanda, J., Ivanov, S. A., Htoon, H., Bezel, I., Piryatinski, A., Tretiak, S. & Klimov, V. I. 2006. Absorption cross sections and Auger recombination lifetimes in inverted core-shell nanocrystals: Implications for lasing performance. *J. Appl. Phys.*, 99(3): Art. No. 034309-7.

Naraginti, S. & Sivakumar, A. 2014. Eco-friendly synthesis of silver and gold nanoparticles with enhanced bactericidal activity and study of silver catalyzed reduction of 4-nitrophenol. *Spectrochim. Acta, Part A*, 128: 357–362.

Narayanan, K.B. & Sakthivel, N. 2011. Heterogeneous catalytic reduction of anthropogenic pollutant, 4-nitrophenol by silver-bionanocomposite using Cylindrocladium floridanum. *Bioresour Technol*., 102(22):10737-10740.

O'Regan, B. & Gratzel, M. 1991. A low-cost, high-efficiency solar cell based on dye-sensitized colloidal TiO2 films. *Nature*, 353: 737-740.

Park, E.K., Kim, J.H., Ji, I.A., Choi, H.M., Kim, J.H., Lim, K.T., Bang, J.H. & Kim, Y.S. 2014. Optimization of CdSe quantum dot concentration in P3HT: PCBM layer for the improved performance of hybrid solar cells. *Microelectron. Eng*., 119: 169–173.

Pastoriza-Santos, I. & Liz-Marzán, L.M. 1999. Formation and stabilization of silver nanoparticles through reduction by N,N-Dimethylformamide. *Langmuir*, 15 (4): 948–951.

Paula, D.R. & Robeson, L.M. 2008. Polymer nanotechnology: Nanocomposites. *Polymer*, 49(15): 3187–3204.

Peng, X., Schlamp, M. C., Kadavanich, A. V. & Alivisatos, A. P. 1997. Epitaxial growth of highly luminescent CdSe/CdS Core/Shell nanocrystals with photostability and electronic accessibility. *J. Am. Chem. Soc*., 119 (30): 7019 – 7029.

Pralay, K.S. & Prashant, V.K. 2012. Mn-Doped quantum dot sensitized solar cells: A strategy to boost efficiency over 5%. *J.Am.Chem.Soc*., 134:2508–2511.

Prokopovich, P., Leech, R., Carmalt, C.J., Parkin, I.P. & Perni, S. 2013. A novel bone cement impregnated with silver–tiopronin nanoparticles: its antimicrobial, cytotoxic, and mechanical properties. *Int J Nanomedicine*, 2003(8): 2227—2237.

Pujadas, P., Blanco, A., Cavalaro, S.H.P., Aguado, A., Grünewald, S., Blom, K. & Walraven, J.C. 2014. Plastic fibres as the only reinforcement for flat suspended slabs: Parametric study and design considerations. *Construction and Building Materials*, 70: 88–96.

Purohita, A., Chander, S., Nehra, S.P., Lal, C. & Dhak, M.S. 2015. Effect of thickness on structural, optical, electrical and morphological properties of nanocrystalline CdSe thin films for optoelectronic applications. *Opt. Mater*., 47: 345–353.

Ragacheva, A.A., Yarmolenkoa, M.A., Xiaohonga, J., Shenb, R., Luchnikovc, P.A. & Rogachev, A.V. 2015. Molecular structure, optical, electrical and sensing properties of PANI-based coatings with silver nanoparticles deposited from the active gas phase. *Appl. Surf. Sci*., 351: 811–818.

Rao, Y.N., Banerjee, D., Datta, A., Das, S.K., Guin, A. & Saha, A. 2010. Gamma irradiation route to synthesis of highly re-dispersible natural polymer capped silver nanoparticles. *Radiat. Phys. Chem.*, 79(12): 1240–1246.

Raveendran, P., Fu, J. & Wallen, S.L. 2003. Completely “Green” synthesis and stabilization of metal nanoparticles. *J. Am. Chem. Soc.*, 125: 13940-13941.

Ray, M., Basu, T.S., Bandyopadhyay, N.R., Klie, R.F., Ghosh, S., Raja, S.O. & Dasgupta, A.K. 2014. Highly lattice-mismatched semiconductor-metal hybrid nanostructures: gold nanoparticle encapsulated luminescent silicon quantum dots. *Nanoscale*, 6(4): 2201-10.

Reed, M. A. 1993. Quantum Dots. *Sci. Am.*, 268(1): 118 – 124.

Rodriguez-Mozaza, S., Chamorroa, S., Martia, E., Huertaa, B., Grosa, M., Sànchez-Melsióa, A., Borregoa, C.M., Barceló a, D. & Balcázar, J.L. 2015. Occurrence of antibiotics and antibiotic resistance genes in hospital and urban wastewaters and their impact on the receiving river. *Water Research,* 69:234–242.

Sanusi, K. & Nyokong, T. 2014. Indium phthalocyanine–CdSe/ZnS quantum dots nanocomposites showing size dependent and near ideal optical limiting behaviour. *Opt. Mater*., 38: 17–23.

Schrand, A.M., Braydich-Stolle, L.K., Schlager, J.J., Dai, L. & Hussain, S.M. 2008. Can silver nanoparticles be useful as potential biological labels?. *Nanotechnology* 19: 235104.

Singh, N. & Khanna, P.K. 2007. In situ synthesis of silver nano-particles in polymethyl methacrylate. *Mater. Chem. Phys*., 104: 367–372.

Solanki, J.N. & Murthy, Z.V.P. 2011. Controlled size silver nanoparticles synthesis with water-in-oil microemulsion method: A topical review. *Ind. Eng. Chem. Res*., 50 (22): 12311–12323

Sung, S.D., Lim, I., Kang, P., Lee, C. & Lee, W.I. 2013. Design and development of highly efficient PbS quantum dot-sensitized solar cells working in an aqueous polysulfide electrolyte. *Chem. Commun*., 49: 6054-6056.

Talapin, D.V., Mekis, I., Gotzinger, S., Kornowski, A., Benson, O. & Weller, H. 2004.CdSe/CdS/ZnS and CdSe/ZnSe/ZnS Core−Shell−Shell Nanocrystals. *J. Phys. Chem. B,* 108: 18826-18831.

Talbot, D. 2007. Nanocharging Solar. *Technology Review*, March/April.

Tauran, Y., Brioude, A., Coleman, A.W., Rhimi, M. & Kim, B. 2013. Molecular recognition by gold, silver and copper nanoparticles. *World J Biol Chem*., 4(3): 35–63.

Theodorakosa, I., Zacharatosa, F., Geremiab, R., Karnakisb, D. & Zergiotia, I. 2015. Selective laser sintering of Ag nanoparticles ink for applications in flexible electronics. *Appl. Surf. Sci.*, 336: 157–162.

Tian, J. & Cao, G. 2013. Semiconductor quantum dot-sensitized solar cells. *Nano Rev*., 4: 10.3402/nano.v4i0.22578.

Tonga, L. & Cheng, J. 2011. Label-free imaging through nonlinear optical signals. *Mater. Today*, 14(6): 264-273.

Tsukigase, H., Suzuki, Y., Berger, M.H., Sagawa, T. & Yoshikawa, S. 2011. Synthesis of SnS nanoparticles by SILAR method for quantum dot-sensitized solar cells. *J Nanosci Nanotechnol*., 11(3):1914-22.

Vanaja, M., Paulkumar, K., Baburaja, M., Rajeshkumar, S., Gnanajobitha, G., Malarkodi, C., Sivakavinesan, M. & Annadurai, G. 2014. Degradation of methylene blue using biologically synthesized silver nanoparticles. *Bioinorg Chem Appl*., 2014: 742346.

Wang, H., Qiao, X., Chen, J., Ding, S. 2005. Preparation of silver nanoparticles by chemical reduction method. *Colloids Surf., A,* 256 (2–3) : 111–115.

Wang, K., Rai, S.C., Marmon, J., Chen, J., Yao, K., Wozny, S., Cao, B., Yan, Y., Zhang, Y., Zhou, W. 2014. Nearly lattice matched all wurtzite CdSe/ZnTe type II core-shell nanowires with epitaxial interfaces for photovoltaics. *Nanoscale*, 6(7): 3679-85

Wang, X., Zheng, J., Sui, X., Xie, H., Liuab, B. & Zhao, X. 2013. CdS quantum dots sensitized solar cells based on free-standing and through-hole TiO2 nanotube arrays. *Dalton Trans*., 42: 14726-14732.

Wani, I.A., Ganguly, A., Ahmed,J. & Ahmad, T. 2011. Silver nanoparticles: Ultrasonic wave assisted synthesis, optical characterization and surface area studies. *Mater. Lett*., 65(3) : 520–522.

Wu, F.,Tian, W., Ma, L., Chen, W., Zhang, G., Zhao, G., Cao, S., Xie, W., Wei, T., Li-Na, M., Wen-Ju, C., Gui-Lan, Z., Guo-Feng, Z. 2008. Optical Nonlinear Properties of CdSeS/ZnS Core/Shell Quantum Dots. *Chinese Phys. Lett*., 25: 1461–1464.

Wu, W., Li, F., Nie, C., Wu, J., Chen, W., Wu, C., Guo, T. 2015. Improved performance of flexible white hybrid light emitting diodes by adjusting quantum dots distribution in polymer matrix. *Vacuum*, 111: 1- 4.

Wu, W., Shen, J., Banerjee, P. & Zhou, S. 2010. Core-shell hybrid nanogels for integration of optical temperature-sensing, targeted tumor cell imaging, and combined chemo-photothermal treatment. *Biomaterials*, 31(29):7555-7566.

Xu, C., Li, W., Wei, Y., Cui, X. 2015. Characterization of SiO2/Ag composite particles synthesized by in situ reduction and its application in electrically conductive adhesives. *Materials & Design*, 83: 745–752.

Yan, J., Tao, H., Zeng, M., Tao, J., Zhang, S., Yan, Z., Wang, W. & Wang, J. 2009. PVP-capped silver nanoparticles as catalyst for oxidative coupling of thiols to disulfides. *Chinese J Catal*., 30(9): 856–858.

Yang, Y., Zhang, C. & Hu, Z. 2013. Impact of metallic and metal oxide nanoparticles on wastewater treatment and anaerobic digestion. *Environ. Sci.: Processes Impacts*, 15:39-48.

Yin, H., Yamamoto, T., Wada, Y., Yanagida, S. 2004. Large-scale and size-controlled synthesis of silver nanoparticles under microwave irradiation. *Mater. Chem. Phys*., 83: 66–70.

Zare, Y. 2015. A simple technique for determination of interphase properties in polymer nanocomposites reinforced with spherical nanoparticles. *Polymer*, 72: 93–97.

Zha, M. & Zeng, E. 2015. Application of functional quantum dot nanoparticles as fluorescence probes in cell labeling and tumor diagnostic imaging. *Nanoscale Res Lett*., 10: 171.

Zhang, Q., Chen, G., Yang, Y., Shen, X., Zhang, Y., Li, C., Yu, R., Luo, Y., Li, D. & Meng, Q. 2012. Toward highly efficient CdS/CdSe quantum dots-sensitized solar cells incorporating ordered photoanodes on transparent conductive substrates. *Phys.Chem. Chem.Phys*.,14: 6479–6486.

Zhang, X., Bloch, S., Akers, W. & Achilefu, S. 2012. Near-infrared Molecular Probes for In Vivo Imaging. *Curr Protoc Cytom*. CHAPTER: Unit12.27.

Zhang, Z., Zhang, L., Wang, S., Chen, W., Lei & Y. A. 2001. Convenient route to polyacrylonitrile/silver nanoparticle composite by simultaneous polymerization–reduction approach. *Polymer*, 42 (19) 8315–8318.

Zheng, M., Gu, M., Jin, Y. & Jin, G. 2001. Optical properties of silver-dispersed PVP thin film. *Mater. Res. Bull*., 36: 853–859.

Zhou, X., Li, W., Wu, M., Tang, S. & Liu, D. 2014. Enhanced dispersibility and dispersion stability of dodecylamine-protected silver nanoparticles by dodecanethiol for ink-jet conductive inks. *Appl. Surf. Sci*., 292: 537–543.

Zhou, Y., Yu, S.H., Wang, C.Y., Li, X.G., Zhu, Y.R. & Chen, Z.Y. 1999. A novel ultraviolet irradiation photo-reduction technique for preparation of single crystal Ag nanorods and Ag dendrites. *Adv. Mater.*, 11: 850–852.

Chapter 3

Synthesis and characterization of core-multi shell CdSe based quantum dots and its polymer nanocomposites.

3.1 Introduction

Semiconductor nanocrystallites, due to their quantum confinement effect, possess unique physical and optical properties which have attracted tremendous attention from researchers in the last two decades. The interest in fluorescent semiconducting nanocrystals has increased due to their enormous applications in absorption filters (Hall & Borrelli, 1988; Borelli et.al., 1987) chemical sensors (Somers et al., 2007), light emitting diodes (Schlamp et al., 1997; Lim et al., 2007) and photovoltaic devices in addition to their potential as tools in biotechnology (Sperling & Parak, 2010; Ananthakumar et al., 2014). Extensive experimental and theoretical efforts had been made in the syntheses as well as tuning the size and properties of these materials. Currently the focus has shifted from syntheses to applications of these materials. This includes fabrication of devices, such as solar cells, light emitting diodes (LED) and so on (Lee et al., 2008; Leschkies et al., 2007; Li et al., 2008). In the fabrication of devices, the quantum dots (QDs) need to be well dispersed and must be compatible with the supporting matrix while transferring it into a composite (Kazes et al., 2009; Sun et al., 2008).

CdSe nanocrystals have been considered as an important material because of its high emission efficiency and size-tunable photoluminescence (PL) across the visible spectrum (Bruchez et al., 1998; Danek et al., 1996; Peng et al., 1997). Several works on the syntheses of CdSe using various synthetic routes have been reported. However, most of these methods involved the use of phosphines, and alkylphosphines (such as

trioctylphosphine (TOP), and tributylphosphine (TBP)), as the coordinating solvent or ligand to form complex precursors with Se. Though high quality materials have been produced via these techniques, the starting materials are hazardous, expensive and unfriendly to the environment. Thus, they are good for laboratory setting but undesirable for commercial exploitations.

Core-shell composite QDs exhibit novel properties making them attractive from both an experimental and practical point of view. Over-coating nanocrystallites with higher band gap inorganic materials allows passivation of the surface non radiative recombination sites thereby increasing the quantum yield of the nanocrystals. Previous studies have shown that particles passivated with inorganic shell structures are more robust than organically passivated ones and have greater tolerance to processing conditions necessary for incorporation into solid state structures (Zhao et al., 2013; Littau et al., 1993). Although some stable, inexpensive, low toxic and environmentally benign precursors or solvents have been used to synthesize core-shell QDs, the use of direct, organic, phosphine-free synthetic route for CdSe based core/multi-shell structures with high optical quality is still desirable. In the quest for greener synthesis, coordinating and non-coordinating solvents such as 1-octadecene and liquid paraffin which are environmentally friendly have been used to replace the hazardous coordinating solvents like TOP and TOPO (Bullen & Mulvaney, 2004; Jasieniak et al., 2005; Ouyang et al., 2008; Deng et al., 2005). In a recent development, Wang et al., reported the first synthesis of CdSe/CdS/ZnS core multi-shell QDs using one pot-injection method via a phosphine-free method in paraffin liquid (Wang et al., 2011). This is an environmentally benign and simple method compared to the conventional “two step” synthetic route, which is

laborious and time-consuming, and may strongly harm the properties of core QDs. In CdSe/ZnS core-shell NCs, a type I core-shell material, the band gap of the core lies energetically within the band gap of the shell material and the photo-generated electrons and holes are mainly confined inside the core (Hines & Guyot-Sionnest, 1996). Such core/shell NCs have widespread applications in biological and biomedical research due to better stability and processability (Li et al., 2003; Dabbousi et al., 1997). In the majority of the reported methods, the precursors and solvents used are highly toxic, which can further increase the toxicity of the final product. Recent developments in using greener materials like 1-octadecene, paraffin, hexadecylamine e.t.c. as alternative to toxic reagents has opened a new area for wider application of nanomaterials.

Research is currently focusing towards the design of novel functional materials to perform more complex and efficient tasks. One of the promising approaches is the incorporation of nanoparticles into a suitable polymer matrix to form a nanocomposite. These multicomponent materials will have the combined novel properties of both the nanoparticles and polymer matrix. Effective dispersion of the QDs inside the polymer matrices is one of the key factors which determine the optical properties of the polymer nanocomposite. Due to the organophobic surface of the QDs, they tend to agglomerate inside the polymer matrix causing light scattering inside the matrix (Novak, 1993; Li et al., 2008). Various techniques have been adopted to increase the dispersion of fillers inside the polymer matrices such as modifying the QDs surface, using nanoplatelets for effective dispersion, etc. (Li et al., 2008; Sun et al., 2008). In some cases these surface modifications increases the particle size which causes low transparency and lower luminescence efficiency (Zou et al., 2010). Transparent epoxy resin is mostly employed

encapsulant in LED solid-state lighting due to their high transparence, high glass transition temperature and low water absorption (Kortan et al., 1990).

Highly luminescent nanocrystals with narrow emission width may be grown in hydrophobic inorganic surfactants which are insoluble in water and, therefore not compatible for some applications that require hydrophilic conditions. An alternative to this is the synthesis in aqueous solutions (Correa-Duarte et al., 1998; Rogach et al., 2000). However, this usually produces polydispersed nanocrystals with a broad trapped state emission. This draw back limits some of their applications. One of the strategies to solubilize high quality nanocrystals in aqueous solvents is by ligand exchange of the nanocrystal surface with a thiol-terminated aliphatic compound having a primary carboxyl group (Chen et al., 1999; Mitchell et al., 1999; Chan & Nie, 1998). Most of the water soluble NCs produced via ligand exchange usually have low (or lose their) luminescent properties after the surface modification. In the case of thiol-terminated aliphatic carboxylic acids, the bond holding the primer to the nanocrystal is dynamic, and sometimes leads to low stability of the nanocrystals in water. Hence, the syntheses of highly stable water soluble QDs with high fluorescent emission still require much attention.

Although significant developments have already been made in the synthesis of fluorescent core- shell QDs, there are still empty gaps to explore like, the use of environmental friendly reagents, more economic conditions like absence of inert atmosphere, low temperature synthesis etc. The preparation and characterization of fluorescent quantum dots – polymer nanocomposites is a least exploited field. Considering their huge potential for application in various fields like solar energy, bio sensing and bio medical

applications, there is still need to explore these systems more. Keeping this in mind, various fluorescent core shell QDs were synthesized in the absence of inert atmosphere using environmental friendly reagents followed by their polymer nanocomposites. Synthesis of water soluble core-shell QDs by ligand exchange without losing the fluorescence of the materials was also done. The synthetic route and, optical and morphological characterization and properties were explained in details in this chapter.

3.2 Materials and Methods

3.2.1 Materials required

Cadmium oxide (CdO; 99.5%) was purchased from Loba chemie. Selenium powder (Se; 99.9%) and 11-mercaptoundecanoic acid were obtained from Sigma Aldrich. Zinc acetate dehydrate ($Zn(CH_3COO)_2 .H_2O$, cadmium chloride ($CdCl_2. xH_2O$) analytical reagent), zinc sulphide anhydrous (ZnS), potassium hydroxide (KOH), oleic acid (OA, analytical grade), sodium sulphide ($Na_2S.9H_2O$), hexadecylamine (HDA), toluene, acetone GR (58.08 g/mol) were purchased from Merck. Paraffin liquid (chemical grade with boiling point higher than 300 ^oC) was from Nice chemicals. The polymer, diglycidyl ether of bisphenol A and the curing agent 4, 4' diaminodiphenyl methane (DDM), were supplied by Atul India limited. Poly methyl methacrylate (PMMA) (Mn- 15,000) was from Himedia while poly (e-caprolactone) (PCL, Mn= 50,000 – 80,000) was purchased from Sigma – Aldrich company.

3.2.2 Method of synthesis

3.2.2.1 Synthesis of CdSe/CdS/ZnS core multi shell QDs

In a typical synthesis, 0.2 mmole of Se was dissolved in 18 mL of paraffin in a three neck flask at 220 ^{o}C under vigorous stirring. In another flask, CdO (2 mmole) was dissolved in a mixture of 6.0 mmole oleic acid (2 mL) and paraffin liquid (8 mL) in a three necked flask at 160 ^{o}C. This cadmium precursor solution (2 mL) was quickly injected into the Se solution, and the growth temperature was kept at 220 ^{o}C. Aliquots were taken at different time intervals and immediately injected into toluene to stop any further growth. To add the CdS layer to the core, the temperature of the core CdSe solution was quickly cooled to 50 ^{o}C. Then 0.5 mmole of $Na_2S.9H_2O$ as the sulphur precursor was added into the solution and heated to 140 ^{o}C under vigorous stirring. The Cd precursor (2 mL, 0.25 mmole) produced by dissolving cadmium acetate in liquid paraffin was injected dropwise into the reaction to produce the CdS shell. Then the solution was cooled to 100 ^{o}C. After 30 min of reaction, another portion of $Na_2S.9H_2O$ (0.5 mmole) was added into the solution, and the solution was heated to 160 ^{o}C under vigorous stirring. Then the Zn precursor (3 mL, 0.48 mmole) prepared by dissolving zinc acetate in liquid paraffin was injected drop wise into the solution and the mixture was cooled to 100 ^{o}C and kept for 90 min for the ZnS shell growth. Aliquots were taken at different reaction times and diluted with toluene for further analysis.

3.2.2.2 Synthesis of CdSe/CdS/ZnS core-multi shell epoxy nanocomposite

As- synthesized CdSe/CdS/ZnS core- multi shell QDs were dispersed in epoxy polymer matrix by the melt mixing technique. A solution of 0.3 weight percentage core-multi-shell QDs was mixed with the polymer (40 g) by ultra-sonication for 1 hour at room temperature. Then the curing agent DDM was added at 80 ^{o}C and stirred for 15 min. The mixture was poured into a preheated metal mould and cured at 100 ^{o}C for 5 hours in a hot

air oven to produce the polymer nanocomposite. Neat epoxy resin was cured at the same reaction condition for comparison.

3.2.2.3 Synthesis of CdSe/ZnS core-shell quantum dots

The preparation of organically soluble CdSe/ZnS core-shell was based on the hot precursor injection technique by following our method on the synthesis of CdSe/CdS/ZnS with slight modifications (Mohan et al., 2014). In the current synthesis, 0.2 mmol of Se was dissolved in 18 mL of paraffin in a three necked flask at 220 ^{o}C under vigorous stirring. In another flask, the cadmium precursor was prepared by dissolving CdO (2 mmol) in a mixture of 0.6 mmol oleic acid (2 mL) and paraffin liquid (8 mL) at 160 ^{o}C. The oleic acid dissolves the CdO and forms a homogenous solution and it also acts as the capping agent for the final core-shell structure. 2 mL of the cadmium precursor solution was quickly injected into the Se solution, and the growth temperature was kept at 220 ^{o}C. Aliquots were taken at different time intervals (to monitor the growth of the NCs until there is no further change in the absorption spectra) and immediately injected into the toluene to stop further growth. After 20 mins, the solution was cooled to 100 ^{o}C, followed by the addition of $Na_2S.9H_2O$ (0.5 mmol) into the solution. The solution was heated to 160 ^{o}C under vigorous stirring followed by drop wise addition of the Zn precursor (3 mL) prepared by dissolving zinc acetate in liquid paraffin. The mixture was cooled to 100 ^{o}C and the reaction was allowed to continue for 90 min to allow for the growth of the ZnS shell. Aliquots were taken at different reaction times and diluted with toluene for further analysis.

3.2.2.4 Synthesis of CdSe/ZnS – PMMA polymer nanocomposite film

3 g PMMA pellets was dissolved in 10 mL toluene. 0.5 weight percentage of core-shell QDs were added to the polymer solution and stirred well. The mixture is then sonicated for 20 minutes keeping it in an ice bath to avoid the degradation of polymer matrix due to increase in temperature. The resultant polymer nanocomposite was solvent casted on a Teflon mould and dried at room temperature for 5 hours and again dried at 40 ^{o}C in a hot air oven.

3.2.2.5 Synthesis of HDA capped CdSe QDs

A (20 ml) 0.04 M $CdCl_2$ solution was mixed with (20 ml) 0.04 M Se solution (sodium selenosulphate) and stirred for 15 minutes ($NaSeSO_4$ was previously prepared by refluxing a mixture of 0.002 mol selenium and 0.8 g sodium sulphite (0.127 mol) in 50 mL distilled water at 70 ^{o}C for 8 hours) to produce a yellow precipitate of CdSe. The solution was centrifuged followed by the dispersion of the precipitate into 6 mL octadecene. This produced well dispersed yellowish solution. The resultant octadecene-CdSe complex was injected into 6 g hot HDA at 160 ^{o}C in a there neck flask under ambient condition. The addition of the octadecene-CdSe solution resulted in sudden temperature decrease to 140 ^{o}C. The reaction mixture was raised to 160 ^{o}C and the reaction was allowed to continue for 1 h followed by the addition of excess methanol. The addition of the methanol resulted in the reversible flocculation of the nanoparticles. The flocculate was separated from the supernatant by centrifugation. Excess methanol was removed under vacuum to give HDA-capped CdSe nanoparticles. The resultant particles were dissolved in toluene to give an optically orange solution of nanocrystallites for characterization.

3.2.2.6 Synthesis of electrospun polycaprolactone-HDA capped CdSe nanofibres

3 g PCL pellets was dissolved in 10 mL acetone and stirred for 8 hours in a magnetic stirrer to get a uniform solution of PCL. To this solution, 0.1 weight percentage of HDA-CdSe solution was added to the PCL solution and stirred for another 4 hours at room temperature. The solution was filled in a 10 mL syringe and mounted on the electrospinning machine. The spinning parameters were adjusted as follows. Tip to collector distance= 15 cm, Applied voltage = 15 KV and Feed rate =1 ml/hr.

3.2.2.7 Conversion of organic soluble QDs to water soluble - Ligand exchange

Modification of the organic soluble QDs into water soluble was done by using the ligand exchange procedure. Excess toluene in QDs where removed using methanol. 2 mL of core-shell QDs were dispersed in 10 mL chloroform to form an orange-colored solution. 0.1 g of 11-mercaptoundecanoic acid was added to the solution and dissolved completely. In a different vial, a pH 13 solution was prepared by dissolving 0.1 g of KOH flakes in 20 mL of distilled water (DW). Approximately 6 mL of the basic solution was added to the chloroform solution and shaken vigorously yielding a milky orange solution. This solution was centrifuged at 6000 RPM for 2 min leading to phase separation. The top aqueous phase was orange due to the transference of QDs to the water and the bottom organic solution was milky white. The aqueous phase was collected and methanol was added at a ratio of 3:1 to water. The solution was centrifuged at 6000 RPM for 2 min, and the QDs precipitated out of the solution. The precipitate was dried and re-dispersed by sonication in DW. Since the bottom organic phase still retains orange color, the process was repeated again from the addition of the aqueous basic solution onwards.

3.3 Characterization Techniques

3.3.1 Ultraviolet-visible (UV-Vis) spectroscopy

The absorption properties of the synthesized materials were analysed by using SHIMDTH UV2401PC spectrophotometer at room temperature. The liquid samples were diluted and the measurements were taken in a quartz cuvette. The absorption band-gaps were calculated using the direct band gap method by plotting a graph of hυ (in eV) Vs $(Ahυ)^2$, where h is Planck's constant (6.626×10^{-34}), υ is frequency of light and A is the absorbance. The particle diameters were calculated using the Yu *et al.*,equation, (D = $(1.6122 \times 10\text{-}9)\lambda^4$ - $(2.6575 \times 10\text{-}6)\lambda^3$ + $(1.6242 \times 10\text{-}3)\lambda^2$ - $(0.4277)\lambda$ + (41.57) where D (nm) is the size of a given nanocrystal sample, and λ (nm) is the wavelength of the first excitonic absorption peak of the corresponding sample.

3.3.2 Photoluminescence (PL) spectroscopy

The emission properties of the nanoparticles were recorded using SHIMDTH RF-5301PC spectrophotometer. The diluted samples were measured using a quartz cuvette. The photoluminescence quantum yield (PL QY) was obtained by Cumberland et al. method i.e. comparison with standard Rhodamine B in methanol and using data derived from the luminescence and the absorption spectra in the following equation: $\phi=\phi'(I/I')(A'/A)(n/n')^2$. In this equation, I (sample) and I' (standard) are the integrated emission peak areas, upon 400 nm excitation; A (sample) and A' (standard) are the absorption at 400 nm; n (sample) and n' (standard) are the refractive indices of the solvents; and ϕ and ϕ' are the PL QY for the sample and the standard, respectively.

3.3.3 Fluorescent Lifetime analysis

The Lifetime measurements of QDs and the QDs/polymer nanocomposites was performed using Horiba jobinvyon IBH picosecond lifetime analyzer. The laser used was of second harmonics within the range of 350-450 nm wavelength. The liquid samples were diluted before analyzing.

3.3.4 Fourier transform Infrared spectroscopy (FTIR)

The confirmation regarding the capping of various QDs were analysed using Fourier transform infrared spectroscopy (Nicolet-Nexus 670 FTIR spectrophotometer), by spanning along a frequency range from 400 to 4000 cm^{-1}. The potential interaction between polymers and inorganic filler inside the polymer nanocomposites also was analyzed.

3.3.5 Raman spectroscopy analysis

The Raman signature peaks of the nanoparticles were analysed using Horiba Jobin Vyon LabRAM HR with laser wavelength of 633 nm. The diluted samples were taken in a glass cuvette and scanned to get the significant peaks.

3.3.6 X-ray diffraction (XRD) analysis

The crystallinity of the materials synthesized was analyzed using XRD. XRD measurements were performed on the Bruker D8 Advance diffractometer operating in the reflection mode with Cu-Kα radiation (40 kV, 20 mA) at a wavelength of 1.5418 Å and diffracted beam monochromator. The samples for the XRD measurements were prepared by casting the nanoparticle solution on glass substrate and subsequently air-drying under

ambient conditions. The particle size of the nanomaterial was calculated using Bragg's equation.

3.3.7 Scanning electron microcopy (SEM) analysis

The morphology of polymer QD composite thin films was elucidated by using scanning electron microscope (SEM) (JEOL-2100, Kyoto, Japan). Thin sections of scaffold were cut using razor blade and gold sputtered using Polaron sputtering apparatus and then analysed.

3.3.8 Energy dispersive x-ray spectroscopy (EDX) Analysis

Energy dispersive X-ray spectroscopy (EDX) system Oxford INCA Energy 200 Premium was used to analyse the material composition of the prepared nanoparticles and polymer nanocomposites.

3.3.9. High resolution transmission electron microscopic (HRTEM)

The detailed morphology and crystallinity analysis of the CdSe core multi shells and their polymer nanocomposites were done by using JEOL JEM- 3010 electron microscope operating at 200 kV. The samples for TEM and HRTEM analyses were prepared by putting a drop of toluene solution of the core-shells onto an amorphous carbon substrate supported on a copper grid and then allowing the solvent to evaporate at room temperature. For the nanocomposite, the samples were cut into ultrathin layers using microtone cutter.

3.3.10 Brillouin spectroscopy analysis

Brillouin spectroscopy allows access to the elastic coefficients of materials ranging from crystalline to amorphous materials, including nanocomposites. In Brillouin experiments, photons are in elastically scattered by interacting with the hypersonic modes. The hypersonic modes are interpreted as acoustic phonons interacting with the incident photons of the laser beam. The analysis of the scattered light and the frequency shift due to the elastic phonon is used to investigate the mechanical properties of the material. The Brillouin spectrometer used was based on a Sandercock three-pass tandem Fabry-Perot interferometer. The distance between the mirrors was 2.5 mm. The wavelength of the laser was 532 nm and the power was fixed at 100 mW. A photomultiplier was used to detect the light that passed through the interferometer. The high intensity of the elastic scattered light was cut by a shutter during each scan to protect the detector. The size of the measured area for one Brillouin scattering measurement was 50 μm in diameter.

3.3.11. Tensile Analysis

Tensile measurements of the QD polymer nanocomposite were carried out using Tinus olsen H50KT. The composites were cut into uniform pieces of 10 cm length and 2 cm width. Five set of samples were analysed for each composition and the average was calculated.

3.4 Results and Discussions

3.4.1 Synthesis of CdSe/CdS/ ZnS core-multi shell quantum dots

In this reaction, the core CdSe QDs synthesized was not separated from the excess precursors for the next coating step. This is to avoid the inappropriate changes which

could affect the quality of the QDs if exposed to air and moisture. A schematic representation of the synthesis protocol is given in Figure 3.1. The purification of the sample was performed only after the complete formation of the desired multi core shell. The addition of each layer to the core caused an increase in the size of the particles. The nanoparticles obtained were of high quality and monodispersed with highly desirable absorption and emission features. During the entire reaction process, the growth of the particles was clearly evident from both the colour change and the shift of absorption spectra to longer wavelengths as the reaction time increased.

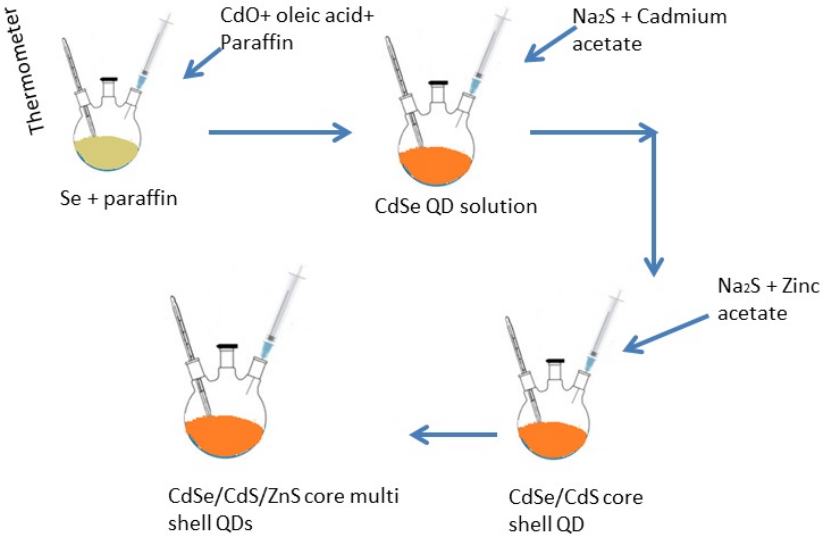

Figure 3.1: Schematic representation of preparation of CdSe/CdS/ZnS core multi shell QDs.

3.4.1.1. Optical characterizations

3.4.1.1.1. UV-Visible spectroscopy

The absorption spectra of the CdSe/CdS/ZnS at different reaction times and different stages of growth are shown in Figure 3.2. The absorption peaks were red-shifted as the

growth time and the shell coating increased indicating increase in particle size. The absorption band-edges as calculated using the direct band gap method (Pankove, 1990) are shown in Table 3.1. The sharp absorption features are indicative of particles with narrow size distributions. The sharpness of the excitonic peak diminishes slightly as the coating increased. This broadening has been attributed to the increase in the particle size (Khani et al., 2011; Peng et al., 1997). The particle diameters as-calculated using the Yu *et al*., 2003 equation, are in the range 2.49 nm to 3.36 nm (Table 3.1).

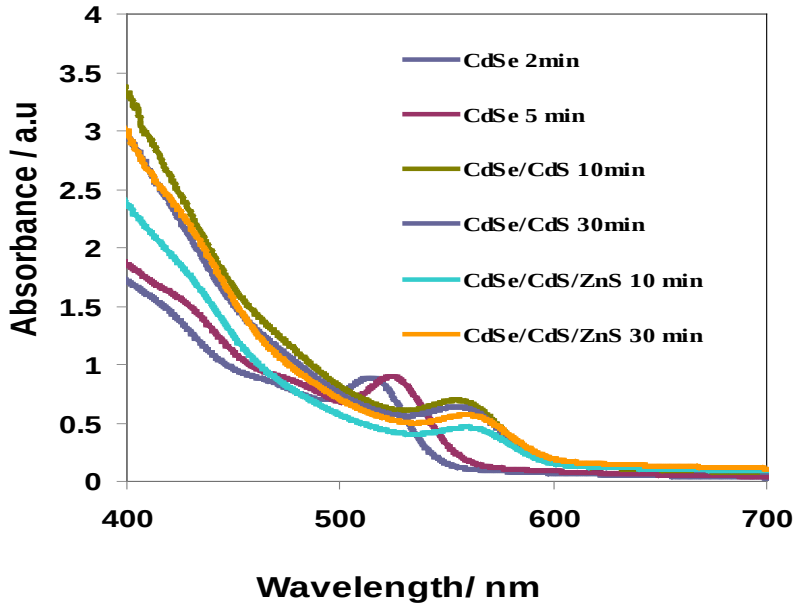

Figure 3.2: UV-Vis absorption spectra of the CdSe/CdS/ZnS core-multi shell QDs at different reaction time and stages of growth.

Table 3.1: Particle size and the band edge values of the core-multi shells

Sample code	Absorption Maxima (nm)	Emission Maxima (nm)	Band Gap (eV)	Particle size (nm)
CdSe 2 min	519	524	3.5	2.49
CdSe 5 min	528	532	3.3	2.62
CdSe/CdS 10 min	558	564	3	3.08
CdSe/CdS 30 min	562	564	2.9	3.20
CdSe/CdS/ZnS 10 min	564	569	2.8	3.29
CdSe/CdS/ZnS 30 min	566	571	2.7	3.36

3.4.1.1.2. Photoluminescence spectroscopy

The emission spectra of the CdSe/CdS/ZnS QDs at different reaction times and different stages of growth are shown in Figure 3.3. The emission maxima of all the as-synthesized particles are red shifted in relation to the corresponding absorption maxima and exhibit band-edge luminescence for excitation at 400 nm with the particles emitting in the green-orange window as the coating layer increased. A red-shift in the PL and absorbance spectra observed for the CdSe/CdS QDs and the CdSe/CdS/ZnS QDs compared with CdSe core QDs has been attributed to the partial leakage of the excitons into the shell matrix and the formation of the core/shell and core/multi-shell QDs rather than the formation of alloyed QDs (Uddin & Chan, 2008; Talapin et al., 2004). The red-shift after the formation of ZnS shell is much smaller than that, after the CdS shell indicating slower

growth rate during the second coating process. In addition, the PL intensity of the CdSe/CdS core/shell QDs was obviously superior to the CdSe core QDs, and it was further improved by further coating with ZnS shell. The fluorescence peak position remained constant as the excitation wavelength was varied indicating that the origin of the emitting state is similar in all species. This observation had also been reported by Bailes et al., 2009 and Wageh *et al*., 2003 and had been attributed as a strong evidence for the purity of the samples. The full width at half maximum (FWHM) and PL quantum yield of the CdSe/CdS/ZnS core-multi shell after 30 mins was found to be 45 nm and 70 % respectively.

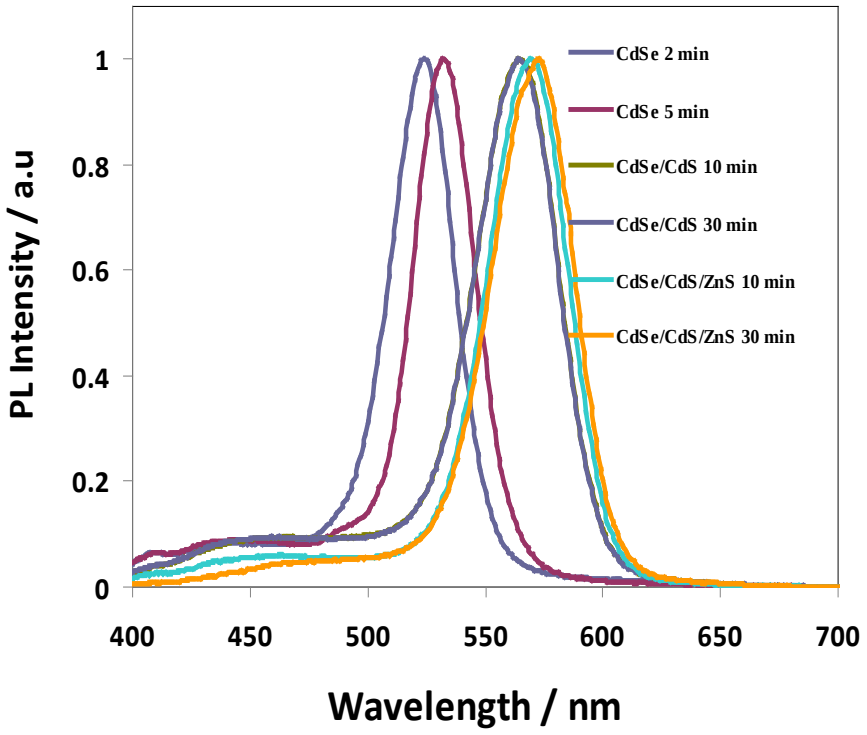

Figure 3.3: photoluminescence spectra of the CdSe/CdS/ZnS core-multi shell QDs at different reaction time and stages of growth.

3.4.1.1.3. Fourier transform infrared spectroscopy

FTIR spectrum of the as-synthesized CdSe/CdS/ZnS core-multi shell QDs is shown in Figure 3.4. The core-shell spectrum showed peak at 3029 cm^{-1} assigned to the –C-H stretching vibration of paraffin. Two peaks at 727cm^{-1} and 1478 cm^{-1} correspond to $–CH_2$ deformation and –C-H bending vibration of the paraffin respectively. The peak at 687 cm^{-1} is the –C-H out of plane bending in paraffin while the peak at 1615 cm^{-1} is the C=C stretching vibration. The $–CH_2$ symmetric and asymmetric stretching of the oleic acid appeared at 2833 cm^{-1} and 2921 cm^{-1} respectively. The –C=O stretching from the –COOH group in oleic acid appeared at 1751 cm^{-1}. The peak at 1459 cm^{-1} is attributed to the in-plane stretching of –the O-H group of –COOH and 1390 cm^{-1} peak correspond to the –C-O stretching in oleic acid (Zhang et al., 2006). The presence of these peaks confirmed successful capping of the QDs by the oleic acid.

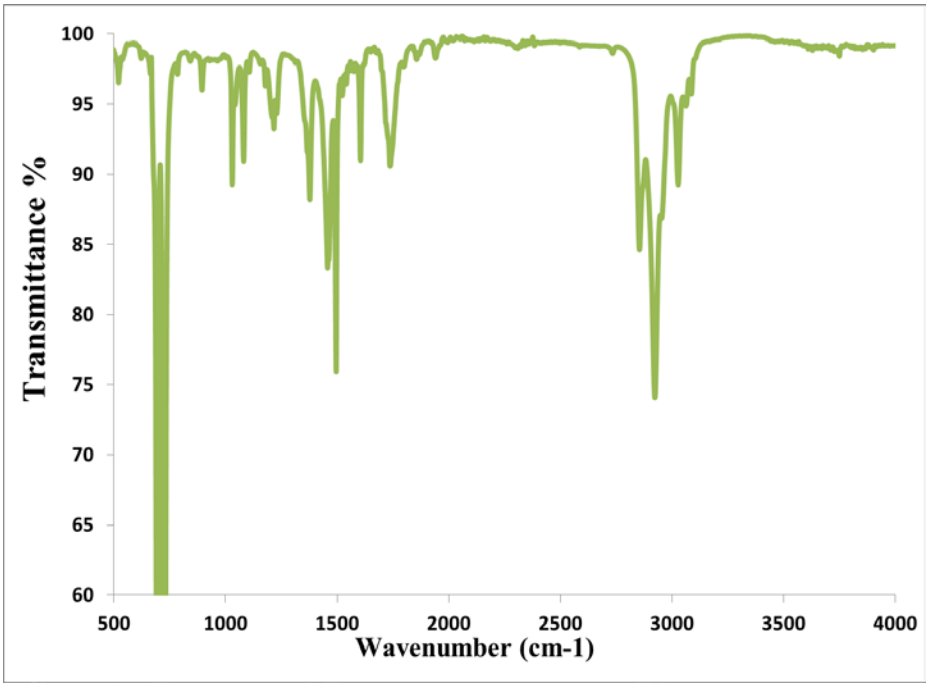

Figure 3.4: FT-IR spectra of CdSe/CdS/ZnS core-multi shell QDs.

3.4.1.1.4. Fluorescent lifetime analysis

The fluorescent life time analysis of the core-multi shell samples at the different stages of the reaction is shown in Figure 3.5. Table 3.2 represents the PL lifetime of CdSe, CdSe/CdS and CdSe/CdS/ZnS QDs. The delay of fluorescence after an excitation by an incident photon obeys a decaying exponential law, which depends on the life time of the excited state. When a fluorophore in solution or bulk is illuminated by a pulsed laser, it will emit a fluorescent signal with an exponential decaying rate, characterized by the lifetimes of the excited transitions. The correlation between the instant of the pulse and the detection of the signal investigated using fluorescence lifetime spectroscopy with characteristic decaying curves is given in Figure.3.5. All decay curves shows multiexponential decay kinetics (Lee et al., 2012). The core-shells shows high lifetime in the order of 10 nano seconds indicating that the particles are highly stable. As the size of the core increases by the addition of various shells, the life time was found to be decreasing. This has been attributed to the decrease in the distance between the donor and the acceptor energy levels (Challa et al., 2011). As the shell grows, the distance between the valence band and conduction band of the shell decreases and the electron-hole is confined in the core which aids the recombination process.

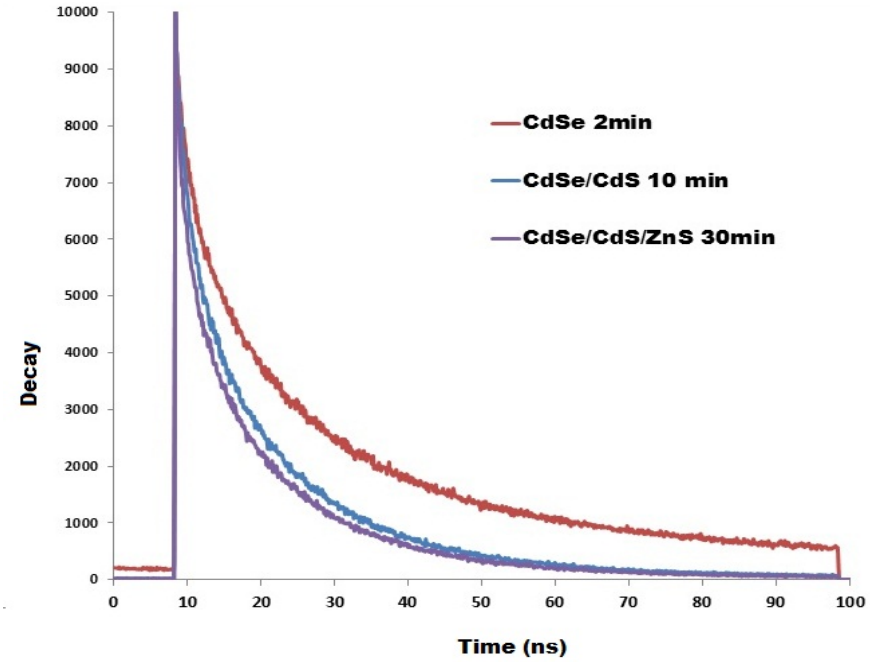

Figure 3.5: Fitted lifetime spectrum for a solution of Core-multi shell QDs.

Table 3.2: PL lifetime of the CdSe/CdS/ZnS core-multi shell QDs

Sample	τ_1	τ_2	τ_3	**B1**	**B2**	**B3**	**A**	χ^2
CdSe 2min	1.6	11.1	34.8	0.4476	0.2851	0.211	329.832	1.0979
CdSe/CdS 10 min	1.58	7.83	17.81	0.4294	0.2115	0.2662	46.67	1.04
CdSe/CdS/ZnS 30 min	1.23	6.8	17.11	0.303	0.2021	0.2299	33.763	1.062

3. 4.1.1.5. Raman spectroscopy analysis

Raman spectra of the as synthesized CdSe/CdS/ZnS core multi shell QDs is shown in Figure 3.6. All the samples were analysed in the liquid state. Because of the very high PL quantum efficiency of QD's as comparison with conventional laser dyes, resonant Raman

spectra were superimposed on a broad luminescence background. This background has been subtracted in all the results. Due to its high fluorescence, much diluted samples were used for the analysis. The sharp peak at 522 cm^{-1} represents the LO phonon Raman signal of the glass substrate. The CdSe, CdSe/CdS and CdSe/CdS/ZnS QDs spectra shows a strong band at 215 cm^{-1} which corresponds to the optical phonon of QD core material – CdSe while the band at 350 cm^{-1} can be interpreted as the TO mode of the ZnS shell(Vega Macotela et al., 2010). In addition to the first-order Raman line, the high-order Raman peaks are also observed at difference mode: 2LO1, the second-order phonon frequency of CdSe is located at 466 cm^{-1} and the third order phonon frequency of CdSe (3LO1) is located at 622 cm^{-1} (Dzhagan et al., 2008).

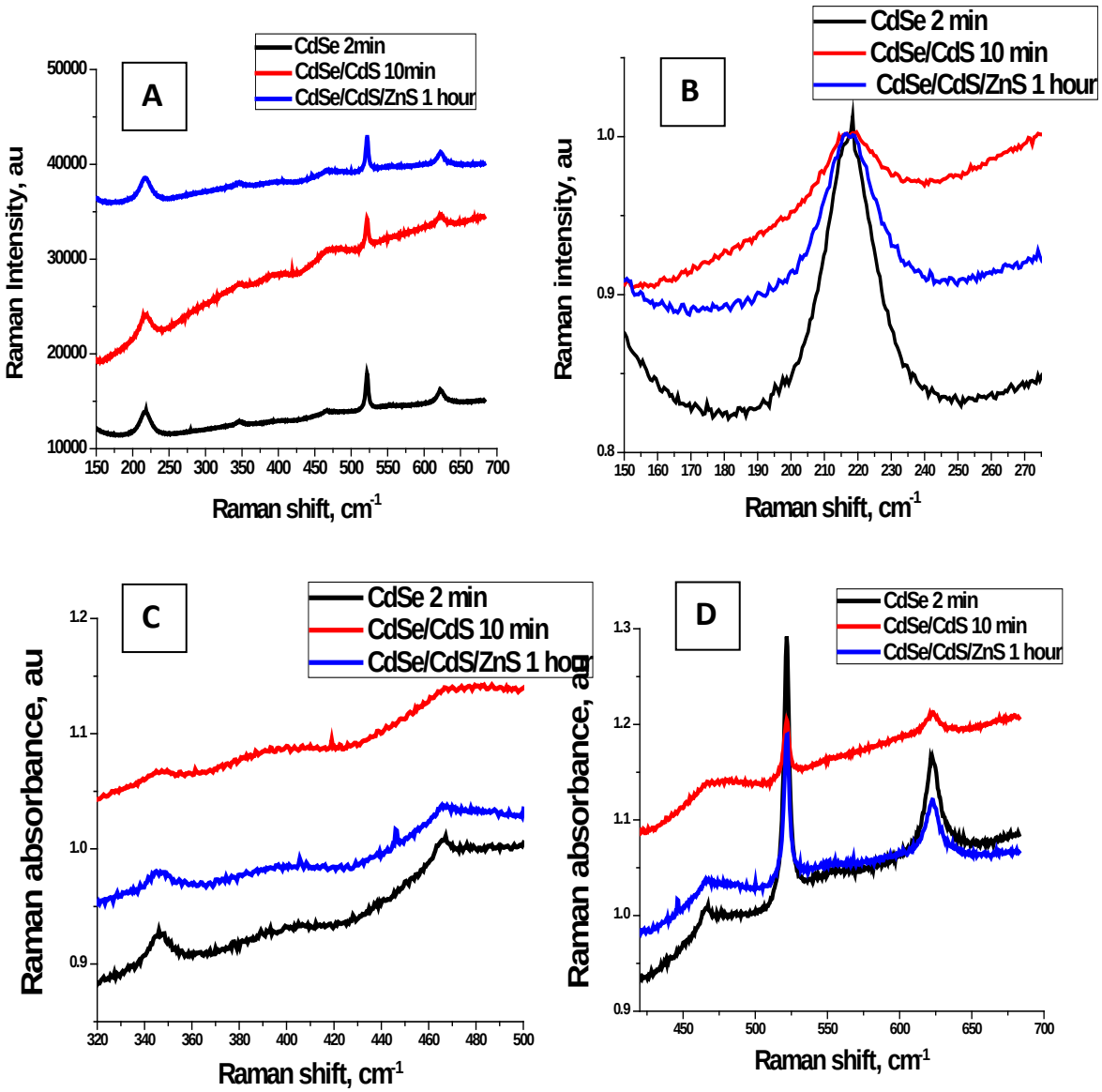

Figure 3.6: (A) Raman spectra of CdSe/CdS/ZnS core multi shell QDs at different reaction time. (B,C,&D) Magnified spectrum at different wavelength range of A.

3.4.1.2. Morphological characterizations

3.4.1.2.1. High resolution transmission electron microscopic analysis

The typical transmission electron microscopy (TEM) of CdSe, CdSe/CdS, CdSe/CdS/ ZnS QDs and high resolution TEM (HRTEM) images of CdSe/CdS/ZnS core-multi shell QDs after 30 minutes are shown in Figures 3.7. The images show that the as-synthesised QDs are, small, spherical and well dispersed with narrow size distribution. The particle size of the CdSe core ranges from 0.33 nm to 0.9 nm with an average diameter of 0.65 ± 0.18 nm and that of CdSe/CdS ranges from 0.98 nm to 3.7 nm with an average diameter of 2.09 ± 0.36 nm. The size distribution curve for the CdSe /CdS/ZnS QDs (Fig 3.8) indicates that the particles are within the range of 1.0 nm to 4.5 nm with an average diameter of 2.97 ± 0.74 nm.

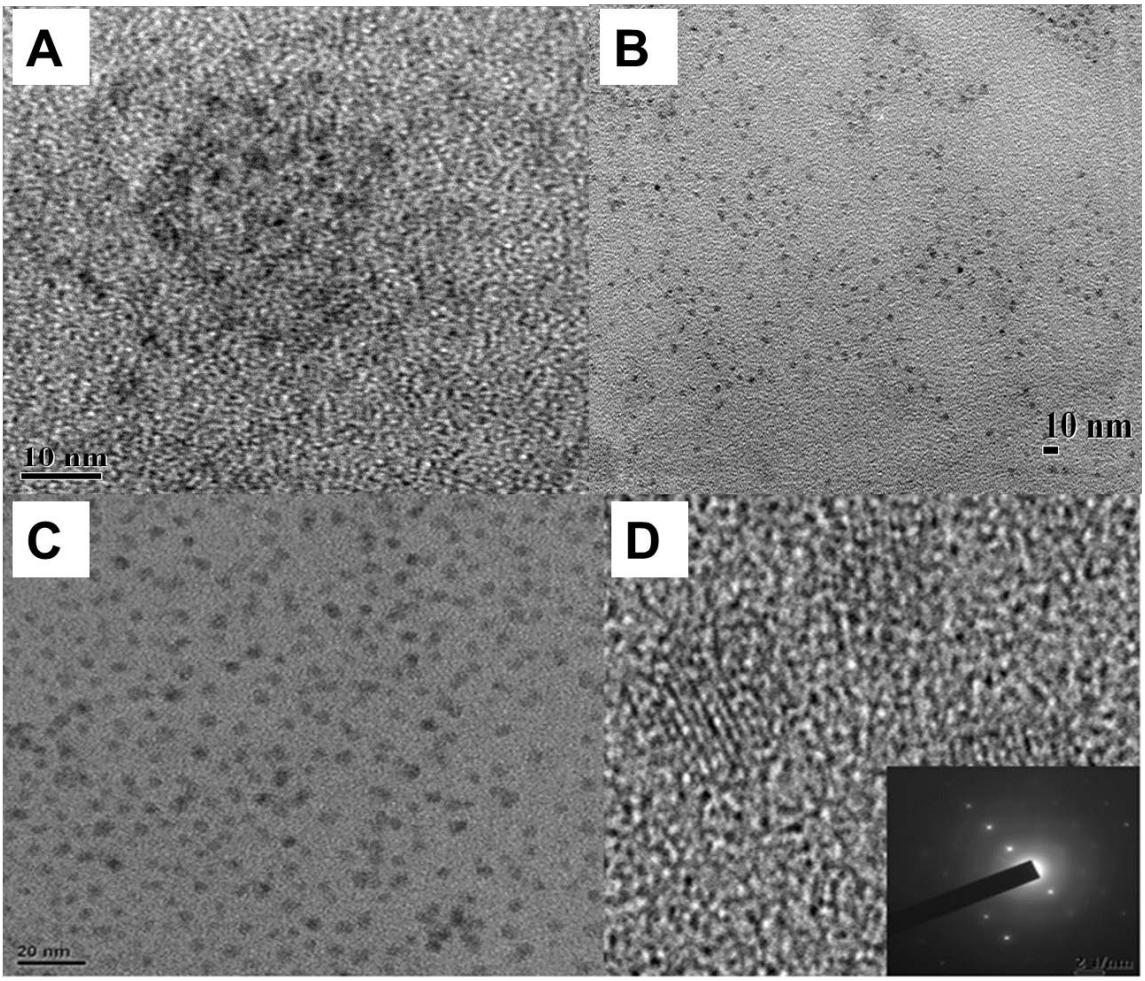

Figures 3.7: (A) TEM Image of CdSe and (B) CdSe/CdS after 30 mins reaction time (C) TEM images of CdSe/CdS/ZnS QDs and (D) the corresponding HRTEM image (inset SAED).

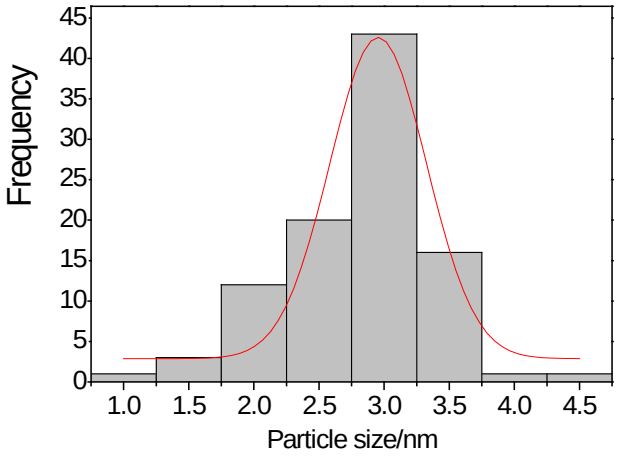

Figure 3.8: Distribution curve of the CdSe/CdS/ZnS QDs.

3.4.1.2.2. Energy dispersive spectroscopy analysis

The electron dispersion spectroscopy (EDS) measurements of the same sample shown in Figure 3.9 confirmed the presence of Cd, Se, Zn and S. The presence of copper is from the sample grid used for the analysis which was made of copper.

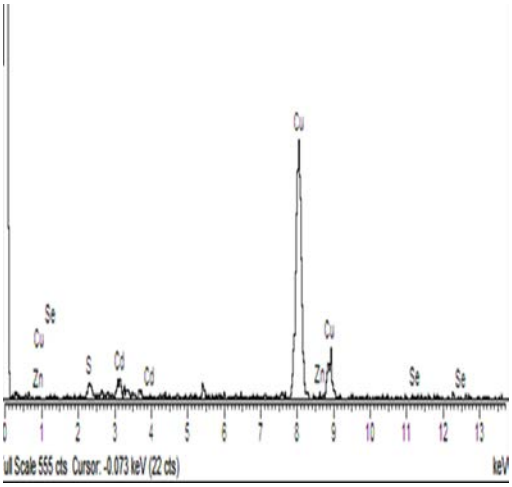

Figure 3.9: Energy dispersive spectroscopy (EDS) of the CdSe/CdS/ZnS QDs.

Summary: A facile and environmentally benign approach for the synthesis of highly fluorescent CdSe/CdS/ZnS core-multi-shell QDs is presented. The CdSe/CdS/ZnS core-multi-shell QDs were prepared via a continual precursor injection and phosphine free method in paraffin liquid and oleic acid without a protective atmosphere. The growth of the QDs from core to multi shell was clearly indicated by the red shift in both UV and PL spectrum. The high crystallinity and monodispersity of the synthesized material was clearly visible from TEM and HRTEM analysis. FTIR spectrum confirmed the passivation of the QDs by the capping agent.

3.4.2. Synthesis of fluorescent Epoxy core-multi shell polymer nanocomposites

3.4.2.1. Photoluminescence spectroscopy

The emission properties of the polymer nanocomposite are presented in Figure 3.10 (A). The maximum emission wavelength of the neat epoxy increased from 456 nm to 526 nm in the epoxy – core-multi shell nanocomposite. This indicates that the QDs have transferred their luminescence property to the neat polymer. Considering the transparency of the composite in Figure 3.10 (B), the core-multi shell nanocomposite is found to be more transparent than the neat epoxy. This can be attributed to the refractive index matching of the polymer and the filler, and the well dispersion of the QDs inside the polymer matrix.

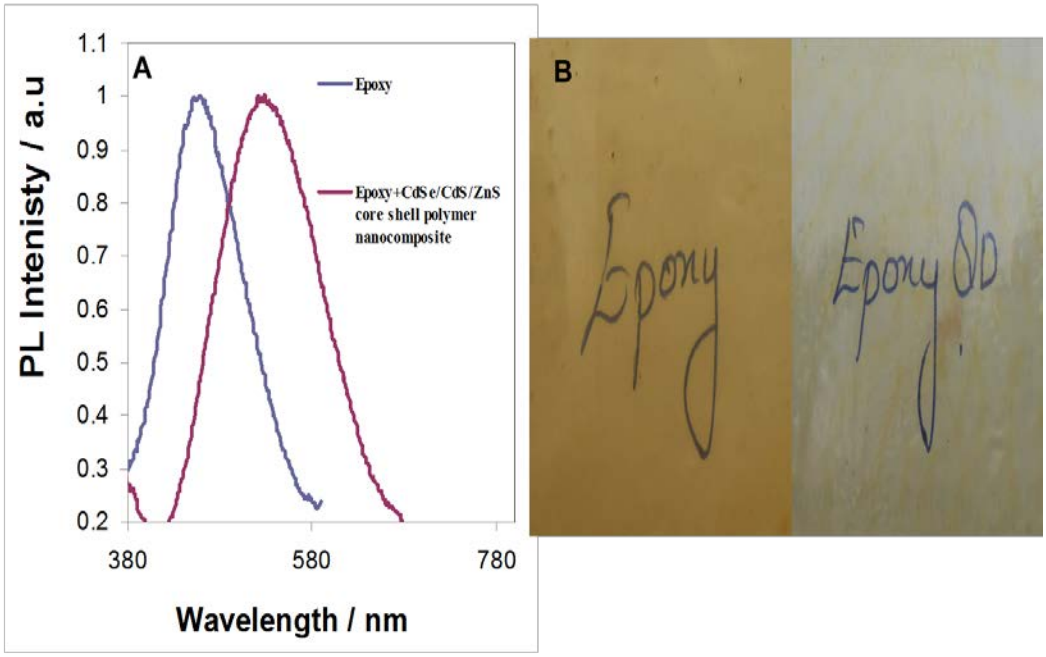

Figure 3.10: (A) Photoluminescence spectra and (B) Photographs of neat epoxy and epoxy- CdSe/CdS/ZnS QD nanocomposites.

3.4.2.2. Fluorescent life time analysis

The life time measurements of the polymer nanocomposite is given in Figure 3.11. The spectra showed that the fluorescent life time of the nanocomposite core-shells decreases when compared to the pure core-multi shells. This has been attributed to the effect of polymer on the surface of the core-multi shells. The surface of the core-multi shells becomes well passivated when it is incorporated into the polymer matrix thereby reducing the number of trap states on the surface of the QDs. Thus, the distance between the energy levels of the donor and acceptor will decrease causing the decrease in the PL life time (Chen et al., 2003). The PL life time values of the nanocomposites are given in Table 3.3.

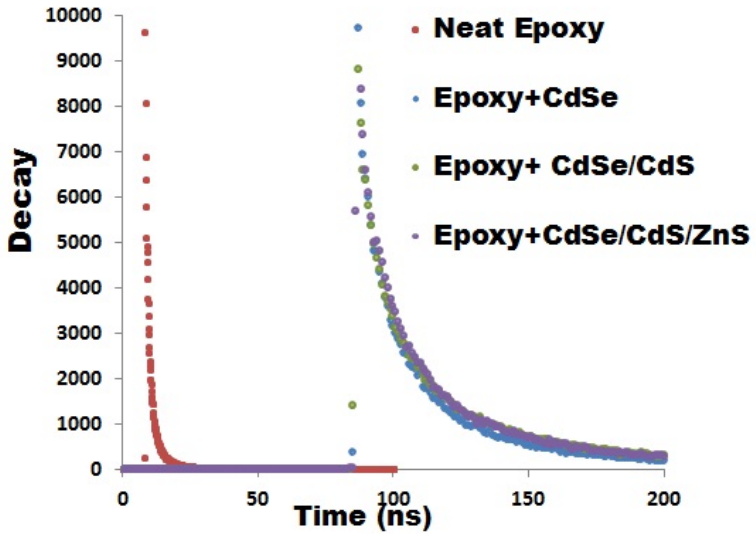

Figures 3.11: Fitted lifetime spectra for CdSe/CdS/ZnS core-multi shell –Polymer nanocomposites.

Table 3.3: PL lifetime of the Epoxy core-multi shell QDs nanocomposites.

Sample	τ_1	τ_2	τ_3	**B1**	**B2**	**B3**	**A**	χ^2
Neat epoxy	86.51	2.61	9.13	0.6968	0.2104	0.0183	0.7964	1.295
Epoxy+ CdSe	34.38	1.74	6.29	1.42	0.4179	0.0739	15.86	1.294
Epoxy + CdSe/CdS	50.32	2.6	0.1096	1.266	0.3298	0.0418	11.48	1.164

3.4.2.3 Brillouin Spectroscopy analysis

Incorporating nanoparticles to plastics or polymer matrix can influence the matrix property in many ways. It can make them stronger, lighter, more durable, and can result in different failure behavior depending on particle size and concentration (Suwanprateeb, 2000; Serenko et al., 2002), interfacial bonding strength (Basaran et al., 2006), relative matrix, and filler strength (Yuan & Misra, 2006). Brillouin light scattering can be

understood as a Bragg reflection in which the inelastic light scattering from a crystal can be an inelastic scattering of a photon from acoustic phonons. In terms of particle description, it is seen as a photon–phonon interaction, where energy and momentum are conserved.

$k_s = k_i \pm q$ --- (1)

where k_s and k_i are the wavevector of the scattered and the incident photon, and q the wavevector of the acoustic phonon. The analysis of the diffused light being realised by an interferometer of Fabry-Perot, this technique makes it possible to measure the propagation velocity of the sound and then enables us to determine elastic constants of studied material.

Brillouin scattering measurements provide the velocity and attenuation of acoustic phonons having frequencies in the range of GHz. The basic experiment consists of measuring the spectrum of the scattered light reflected from the sample. The basic components of this scattered light are a strong elastic peak at the laser frequency with two additional components whose frequencies have been shifted by the inelastic scattering processes. The frequency shift is directly proportional to the acoustic phonon velocity. Figure 3.12 shows the brillouin spectrum of epoxy CdSe polymer nanocomposite with two shifted frequencies due to inelastic scattering. Figure 3.13 shows the variation of acoustic frequency with various filler addition. In the case of neat epoxy, the acoustic frequency was found to be higher than all the composites. In the absence of nanoparticles there is no interference between the polymer chains for the acoustic waves to pass through which is obviously the reason for the better acoustic frequency in neat polymer matrix. When the quantum dots are added, the particles get dispersed between the polymer chains

their by interfering the passage of acoustic phonons which results in low acoustic frequency obtained for the nanocomposites.

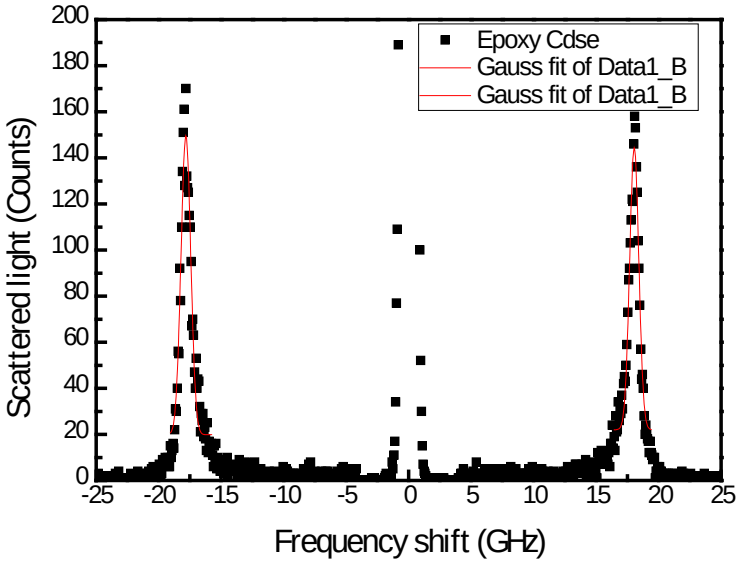

Figure 3.12: Brillouin spectra for Epoxy/CdSe nanocomposite.

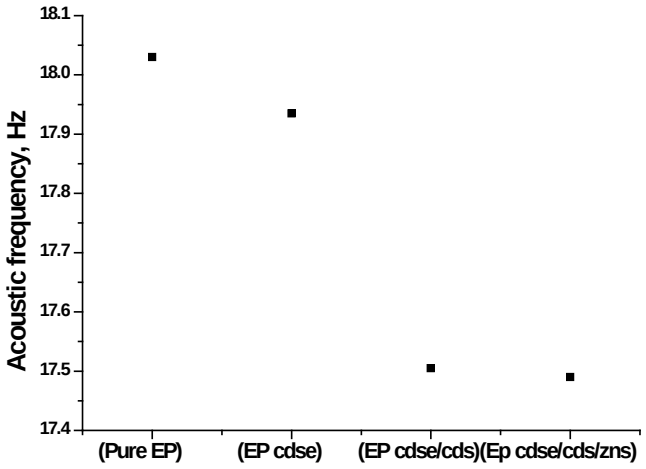

Figure 3.13: Variation of acoustic frequency for neat epoxy and various epoxy core-multi shell nanocomposites.

3.4.2.4. High Resolution Transmission Electron Microscopic Analysis

The TEM micrograph of the as-synthesized CdSe/CdS/ZnS core- multi shell dispersed in epoxy polymer matrix at polymer to QDs ratio of 40:2 is shown in Figure 3.14(A). The TEM image shows that the QDs are well dispersed in the polymer matrix without any changes in their morphology. The particles are spherical in shape thus the dispersion of the QDs in the matrix does not affect their shape. The size distribution curve in Figure 3.14 (B), indicates that the particles are in the range 2.0 nm to 7 nm with an average diameter of 4.95 ± 1.15 nm. The slight increase in the size of the QDs nanocomposite as compared to the QDs has been attributed to the capping of polymer chains around the nanoparticles. The self-assembly of oleic acid on the surface of QDs brings the compatibility and reactive ability to QDs, and aid their dispersion in the polymer (Zou et al., 2011).

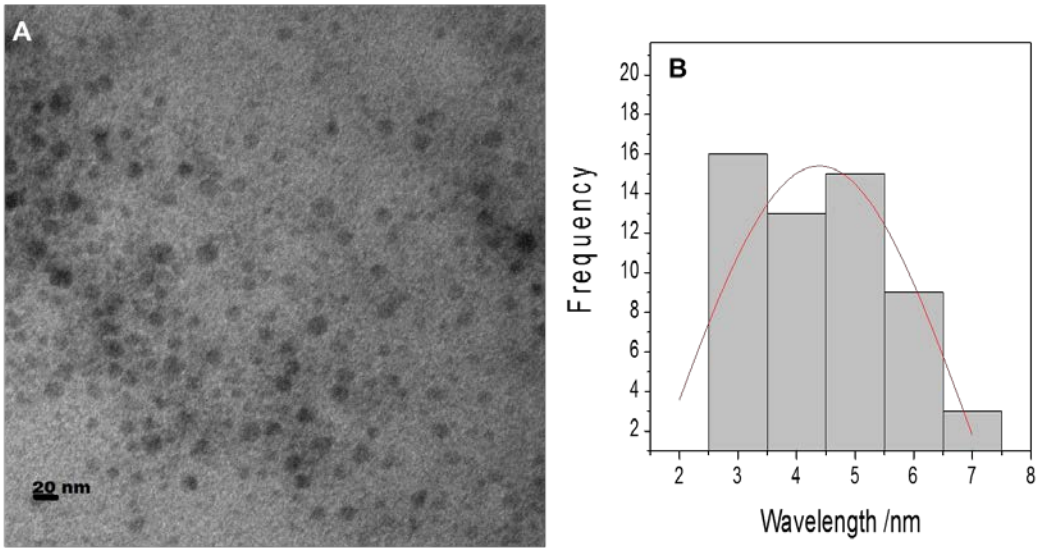

Figures 3.14: (A) TEM image and (B) size distribution of Epoxy- CdSe/CdS/ZnS QDs nanocomposite.

3.4.2.5 Mechanical Analysis

The mechanical properties of the neat epoxy and the epoxy core-shell nanocomposites using the tensile testing with a speed of 1mm/min and the curves are presented in Figure 3.15. The results show that the tensile modulus of the epoxy nanocomposite increases from 1594 MPa in the neat epoxy to 2430 MPa in the epoxy QDs nanocomposite. This indicates that the tensile strength of the nanocomposite is higher than that of the neat polymer matrix.

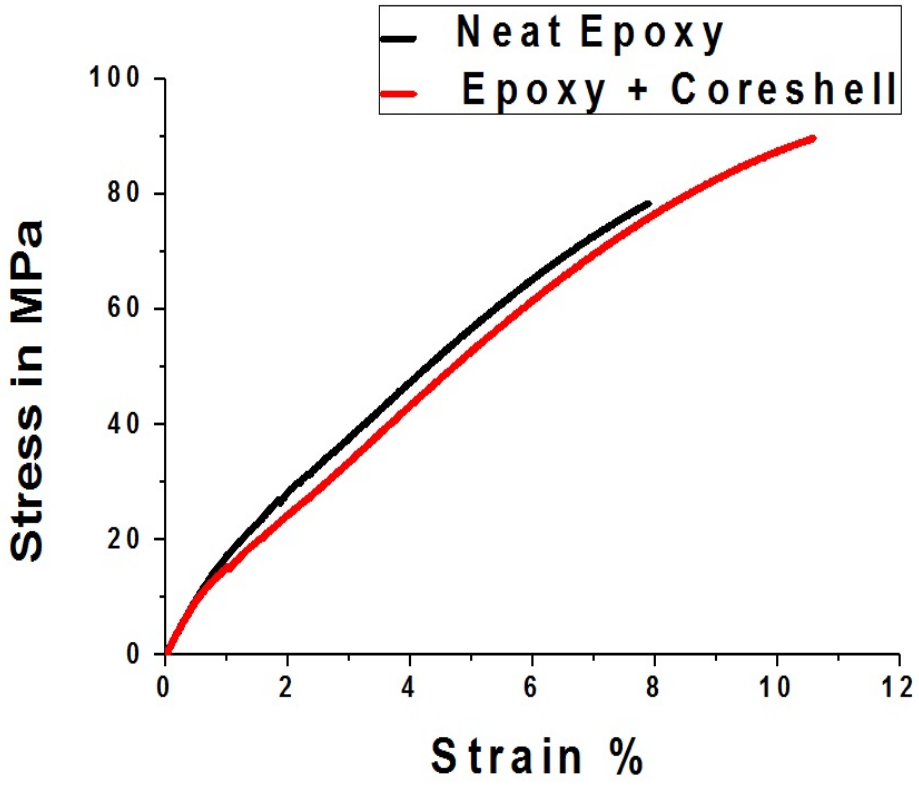

Figure 3.15: The stress strain curves for neat epoxy and epoxy- CdSe/CdS/ZnS core-shell nanocomposite.

Figure 3.16A & B represents a schematic diagram of the epoxy – core-multi shell polymer nanocomposite and the possible interaction between them. The oleic acid capping on the core-multi shell surface make the surface hydrophobic. This in turn makes it compatible with the polymer matrix and hence aided the dispersion of the QDs inside the polymer matrix there by giving a stiffening effect to the polymer chains. The tensile curve (Fig.3.15) indicates that the QD-epoxy nanocomposite shows yield behavior. The area under the tensile curve represents the absorbed energy during stretching which reflects the toughness of the material. Thus, it can be inferred that the toughness of the QD filled polymer is higher than the pure polymer matrix. Therefore, the as-prepared epoxy/QD nanocomposite can be used as encapsulating materials in the fabrication of light emitting diodes devices.

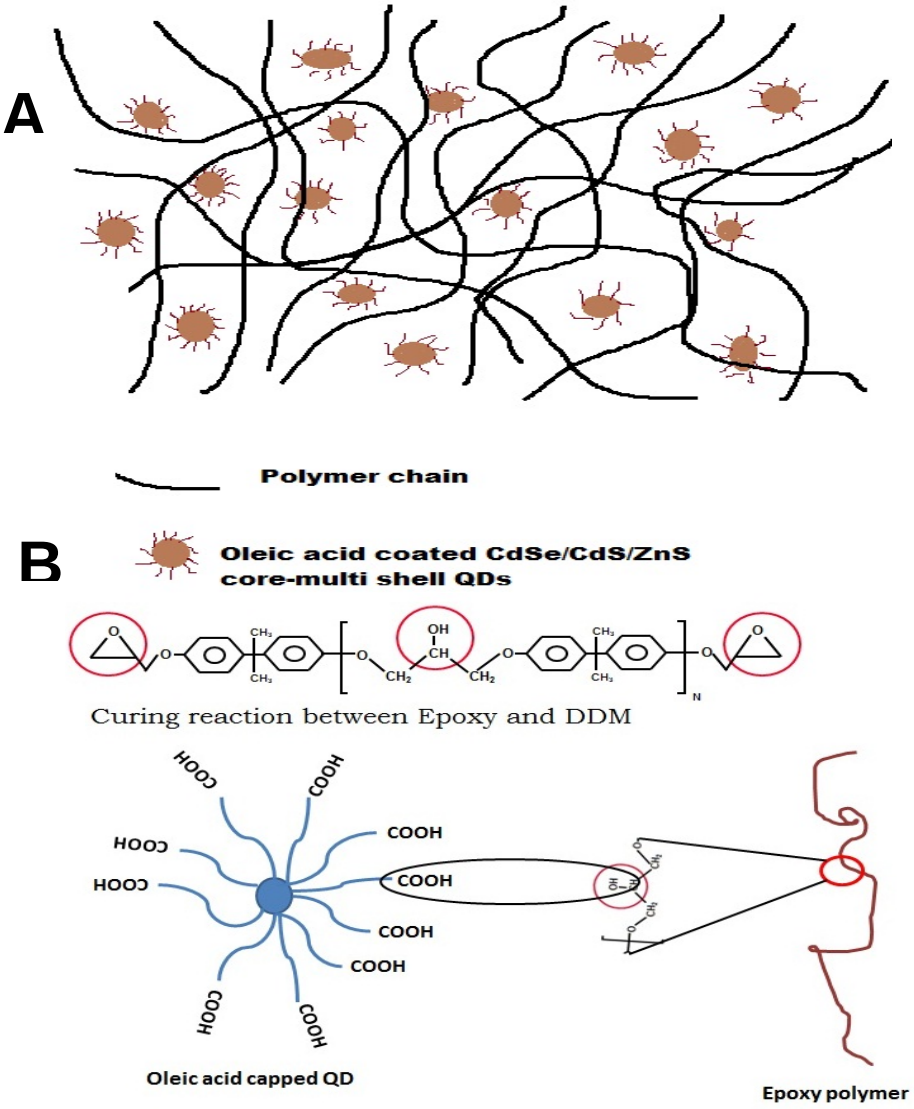

Figure 3.16: (a) Schematic diagram showing the polymer core-multi shell interaction. (b) Mechanism showing the polymer core-multi shell interaction.

Summary: The as-prepared core-multi- shell QDs were dispersed directly in an epoxy polymer matrix via a melt mixing technique. The QDs showed better dispersability and good optical properties in the epoxy matrix. The transmission electron microscope (TEM) images showed that the as-synthesized QDs are small, spherical and are well dispersed

inside the polymer matrix without any change in morphology. It was found that the nanocomposite filled yellow-emitting QDs was more transparent compared to the neat epoxy. The luminescence of the neat polymer shifted from the blue region to yellow region in the nanocomposite. The fluorescent lifetime analysis of the as -prepared core-multi shell and the polymer nanocomposite decreased compared to the core while the tensile measurements showed an increase in the tensile properties of the nanocomposite in comparison with the neat polymer.

3.4.3 Synthesis of CdSe/ZnS core-shell quantum dots

The synthetic method used is a continuous hot precursor injection technique that involved low cost and green reagents in the absence of an inert atmosphere. The synthesis of the core CdSe followed by its coating with the shell layer was done continuously by not separating the core from the reacting solvent. A schematic representation of preparation of CdSe/ZnS core shell is given in Figure 3.17. The as-synthesised nanoparticles were of high quality with high absorption and emission features. During the entire reaction process, the growth of the particles was clearly evident from both the colour change and the shift of absorption spectra to longer wavelengths as the reaction time increases. For the synthesis of the core-shell, the ZnS was added after 20 mins because the absorption and emission maxima remained at the same position at 20 mins and beyond. This indicates particles with the same diameter and signified the end of the CdSe growth.

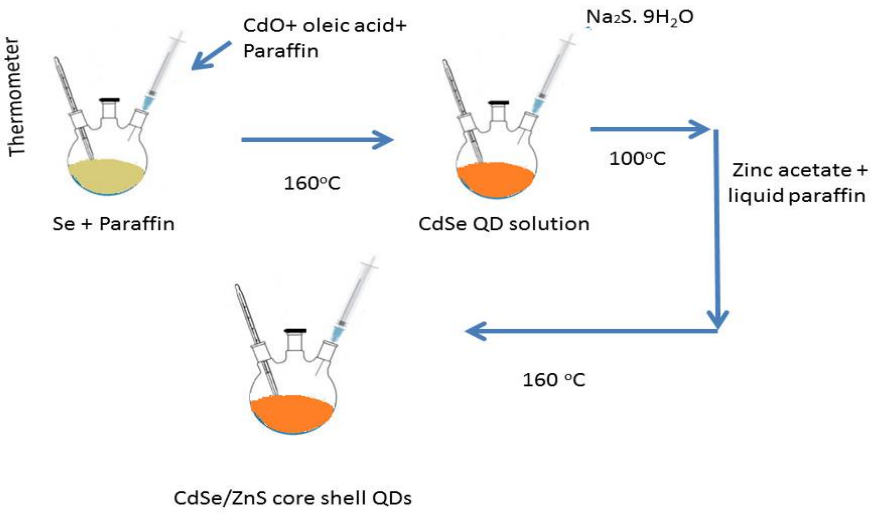

Figure 3.17: Schematic representation for preparation of CdSe–ZnS core-shell QDs.

3.4.3.1. Optical characterizations

3.4.3.1.1. UV-Visible spectroscopy

The absorption spectra of the CdSe/ZnS QDs at different reaction times and different stages of growth are shown in Figure 3.18. The absorption emission peaks were red-shifted as the growth time increased indicating increase in particle size. The absorption band-edges as calculated using the direct band gap method (Pankove, 1990) are showing in table 3.4. The sharp absorption features are indicative of particles with narrow size distributions. The sharpness of the excitonic peak diminishes slightly as the coating increased. This broadening has been attributed to the increase in the particle size distribution (Peng et al., 1997). The particle diameters as-calculated using the Yu *et al.*, 2003 equation, are in the range 2.55 nm to 3.18 nm (Table 3.4).

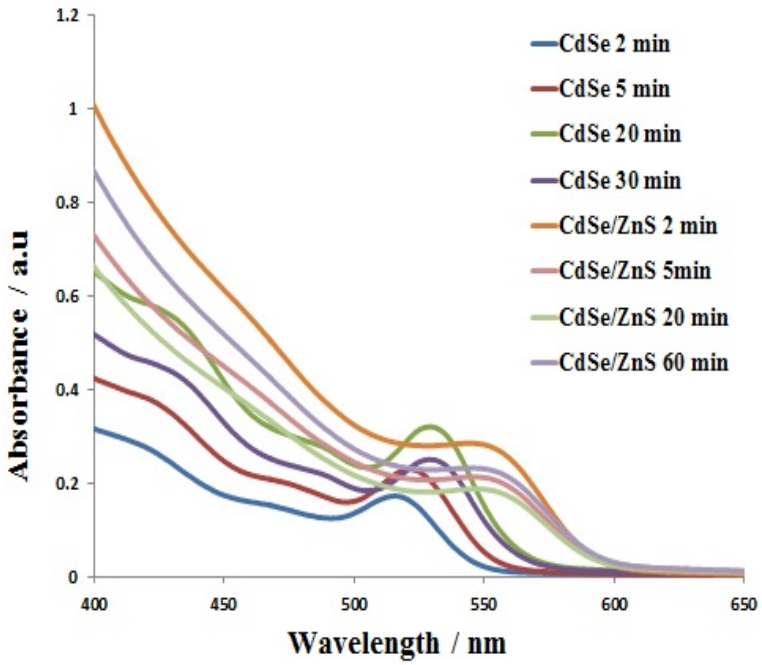

Figure 3.18: UV-Vis absorption spectra of the CdSe/ZnS core- shell QDs at different reaction time and stages of growth.

Table 3.4: Optical properties of the CdSe-ZnS core- shell QDs

Sample code	**Absorption maxima (nm)**	**Emission maxima (nm)**	**Band Gap (eV)**	**Particle size (nm)**
CdSe 2 min	519.5	524	2.28	2.55
CdSe 5 min	522.5	535	2.26	2.62
CdSe 20 min	533.5	537	2.23	2.74
CdSe/ZnS 2 min	550.2	557	2.15	3.05
CdSe/ZnS 5 min	555.2	558.5	2.12	3.16
CdSe/ZnS 20 min	556.5	560	2.1	3.18

3.4.3.1.2 Photoluminescence spectroscopy

The emission spectra of the CdSe/ZnS QDs at different reaction times and different stages of growth are shown in Figure 3.19. The emission maxima of all the as-synthesized particles are red shifted in relation to the corresponding absorption maxima and exhibit band-edge luminescence for excitation at 400 nm with the particles emitting in the green-orange window as the coating layer increased. The formation of the shell was almost instantaneous after the addition of Zn and S precursor as indicated by the large red-shift of the emission maximum from 537 (core CdSe) to 557 (CdSe/ZnS) within 2 min of the shell formation.

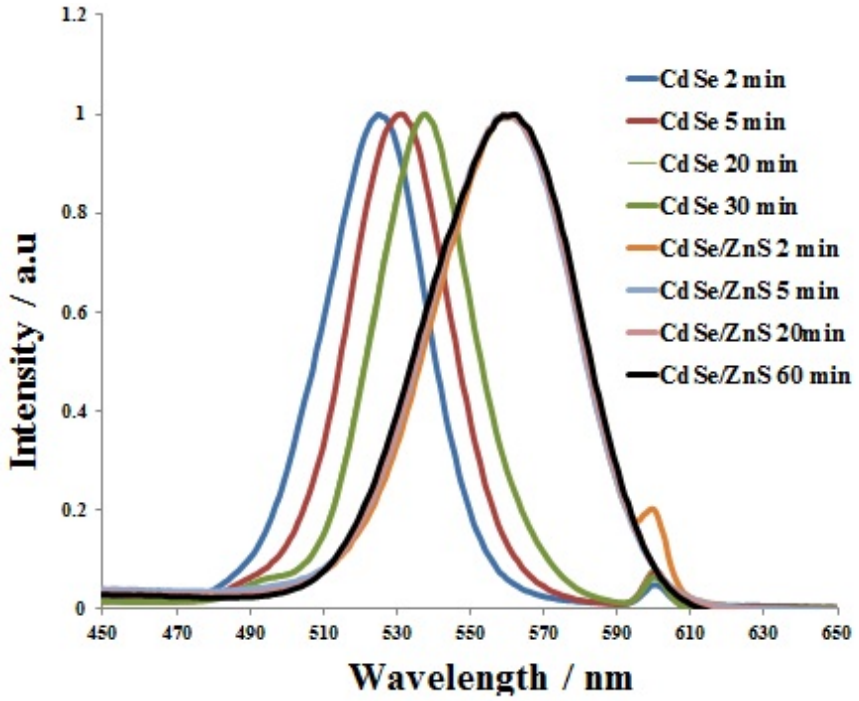

Figure 3.19: Photoluminescence spectra of the CdSe/ZnS core- shell QDs at different reaction time and stages of growth.

After 2 mins, the shift in the emission maximum position was very small indicating slower growth rate. No significant shift was observed after 20 mins thus the reaction could be terminated after 20 mins in the present study. In addition, the PL intensity of the CdSe/ZnS core/shell QDs was obviously superior to the CdSe core QDs. This has been attributed to the formation of a good passivation of ZnS on the CdSe core, which eliminated certain trap states on the QDs surface. In all the samples, the fluorescence peak position remained constant as the excitation wavelength was varied indicating that the origin of the emitting state is similar in all species. The full width at half maximum (FWHM) and PL quantum yield of the CdSe/ZnS core- shell at 60 mins was found to be 50 nm and 74 % respectively.

3.4.3.1.3. Fourier transform infrared spectroscopy

Figure 3.20 shows the FTIR analysis of the as-synthesized organic soluble CdSe/ZnS core-shell quantum dots. The core-shell spectrum shows peak at 3034 cm^{-1} assigned to the –C-H stretching vibration of paraffin. Two peaks at 720 cm^{-1} and 1496 cm^{-1} corresponds to $–CH_2$ deformation and –C-H bending vibration of the paraffin respectively. The peak at 687 cm^{-1} is the –C-H out of plane bending in paraffin while the peak at 1605 cm^{-1} is the C=C stretching vibration. The $–CH_2$ symmetric and asymmetric stretching of the oleic acid appeared at 2908 cm^{-1} and 2930 cm^{-1} respectively. The –C=O stretching from the –COOH group in oleic acid appeared at 1757 cm^{-1} (Talapin et al., 2004). The peak at 1459 cm^{-1} is attributed to the in-plane stretching of –the O-H group of –COOH and 1382 cm^{-1} peak correspond to the –C-O stretching in oleic acid (Bailes et al., 2009). The presence of these peaks, confirmed successful capping of the QDs by the oleic acid.

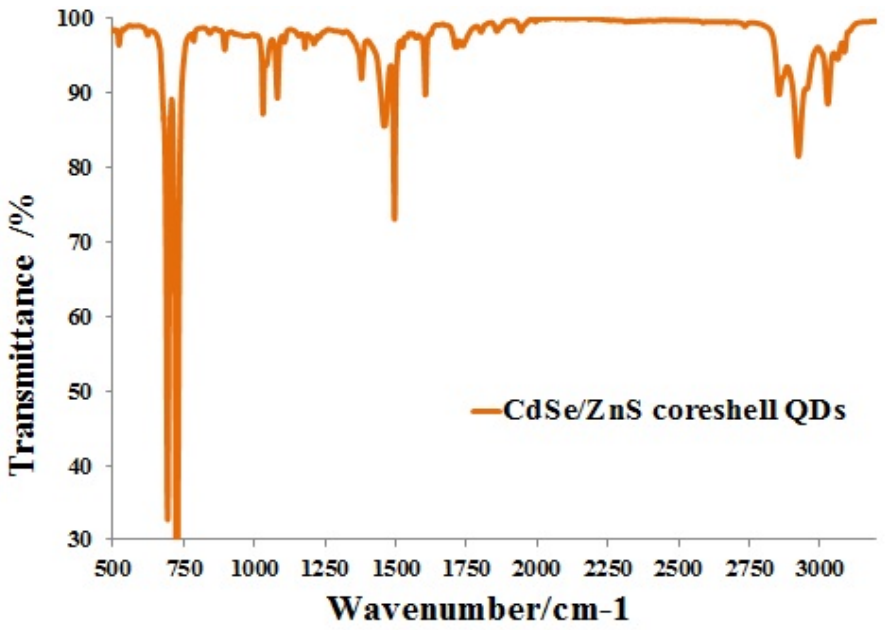

Figure 3. 20: FTIR spectra of organic soluble CdSe/ ZnS core shell QDs .

3.4.3.1.4. Raman spectroscopy analysis

The Raman spectra of the CdSe QDs and CdSe/ZnS core-shell QDs are given in Figure 3.21. The Raman peak of bare core CdSe attributed to the CdSe longitudinal optic phonons, ie the LO phonons appears at 215 cm^{-1}. With bare core CdSe NCs capped by ZnS shell, a new peak appears at 350 cm^{-1} on the right of the LO1 peak (Klein et al., 1990). The new peak is caused by the longitudinal optic phonon of ZnS shell and is denoted as LO2. In addition to the first-order Raman line, the high-order Raman peaks are also observed showing a difference mode: 2LO1, the second-order phonon frequency of CdSe located at 460 cm^{-1} and the third order phonon frequency of CdSe 3LO1 at 620 cm^{-1}. This multi phonon scattering is characteristic of the resonantly excited Raman processes in semiconductor QDs (Bailes et al., 2009). The significant peak at 520 cm^{-1} is due to the Si from the glass cuvette. The shift of the LO peaks of the CdSe core to a

higher wavelength in the core-shell spectrum is attributed to the formation of alloy at the interface of the core shell structure (Siakavellas et al., 1998).

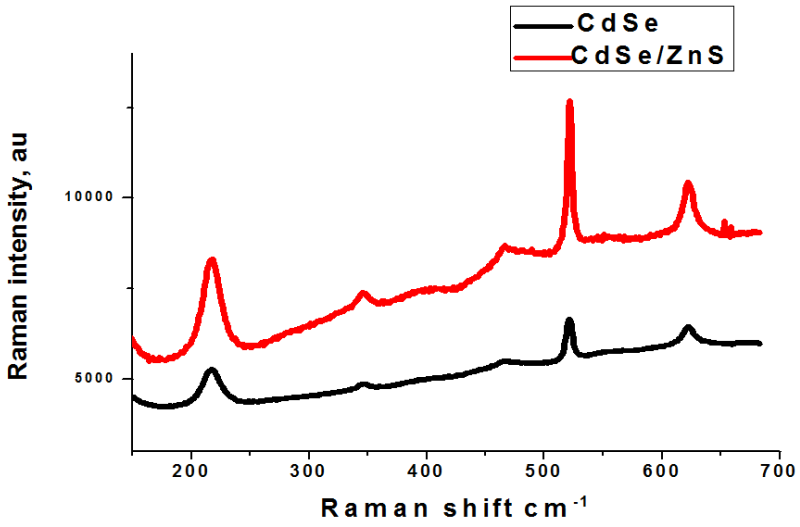

Figure 3.21: Raman spectra of bare CdSe and CdSe/ ZnS core shell QDs.

3.4.3.2. Morphological characterizations

3.4.3.2.1. High Resolution transmission electron microscopic analysis

Figure 3.22 displays the electron microscope images of the CdSe and CdSe/ZnS core/shell NCs. The images show that the as-synthesised QDs are, small, spherical and well dispersed with narrow size distribution. The clear lattice plane observed in the HRTEM (inset Fig. 3.22 B_1) indicates that the materials are of good crystallinity. Moreover, the lattice stretch straight across the QDs with no evidence of an interface, which is consistent with a coherent epitaxial growth mechanism. The size distribution curve (Fig. 3.22 C) indicates that the CdSe particles are within the size range of 1.0 nm to 3.7 nm with an average diameter of 2.24 ± 0.49 nm while the size distribution curve for CdSe/ZnS core-shell QDs (Fig. 3.22 D) indicates that the particles are in the range of 1.98 to 4.9 nm with an average diameter of 3.05 ± 0.52 nm. The ZnS shell thickness as

estimated by the subtraction of the core-shell size observed in Fig. 3.2 B from that of the core CdSe particles in Fig. 3.22 A is found to be approximately 0.55 nm. The formation of the core-shell was further confirmed with the HRTEM image. Fig. 3.22 B_2 indicates that the measured lattice spacing (d) of the core is approximately 3.55 A^0 which corresponds to the (111) plane of Zinc blende (cubic) CdSe while the lattice spacing of the shell is approximately 1.74 A^0 which corresponds to (220) plane of cubic (sphalerite) ZnS.

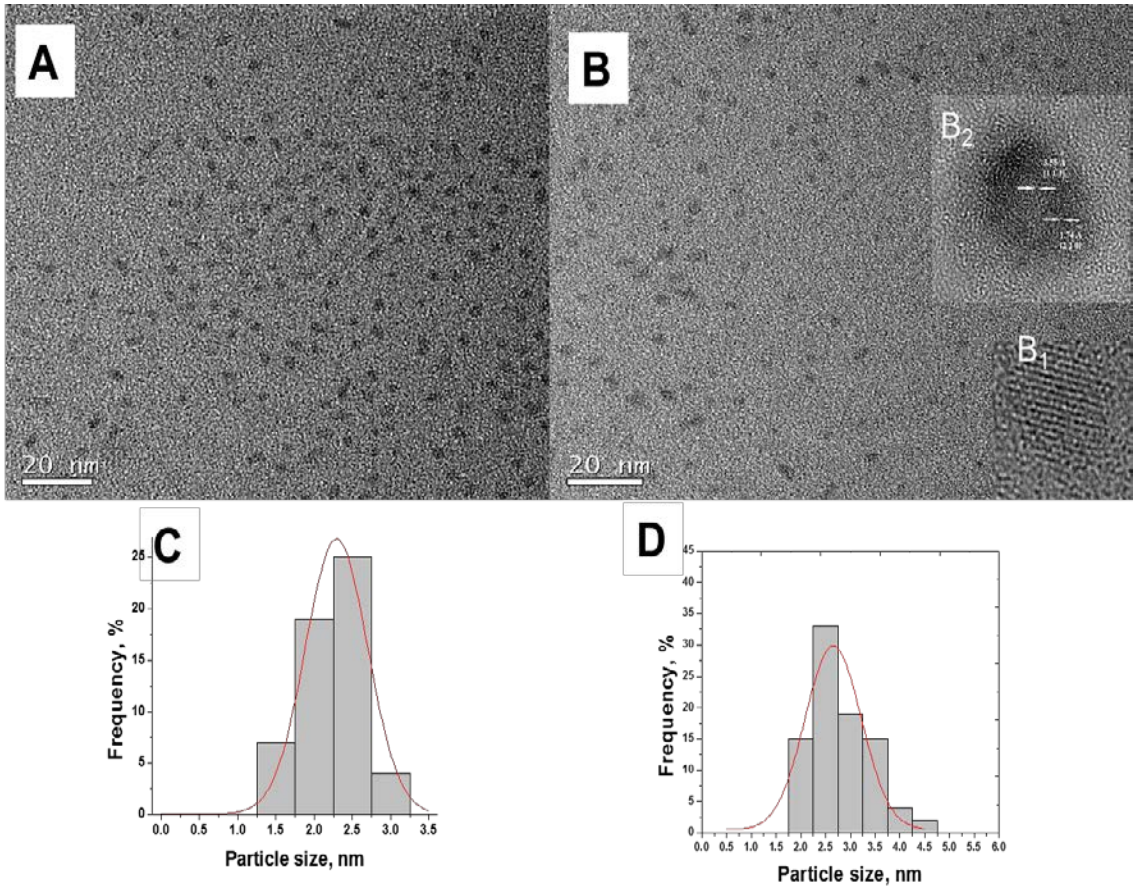

Figures 3.22: TEM image of (A) organic soluble CdSe QDs (B) CdSe/ZnS core-shell QDs (inset HRTEM image). Size Distribution curves of (C) CdSe core and (D) CdSe/ZnS core-shell QDs.

3.4.3.2.2. Energy dispersive spectroscopy

The electron dispersion spectroscopy (EDS) measurements of the CdSe/ZnS core-shell sample (Figure 3.23) confirmed the presence of Cd, Se, Zn and S. The presence of copper is from the sample grid used for the analysis which was made of copper.

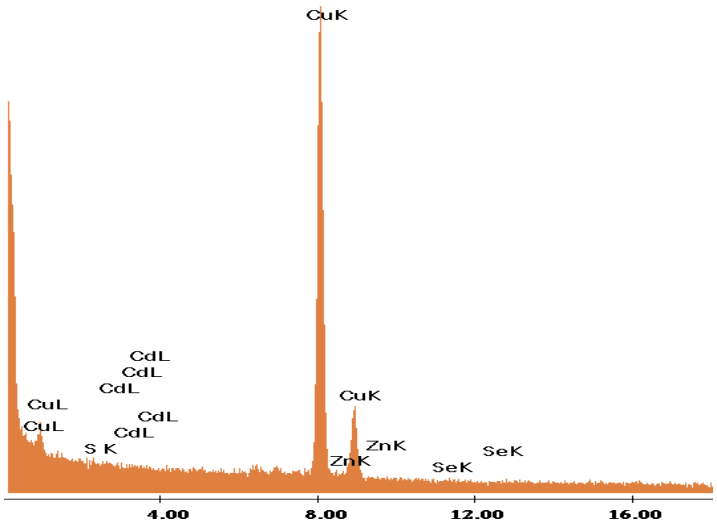

Figure 3.23: EDX of CdSe/ZnS coreshell QDs.

Summary: In this section, the synthesis of CdSe/ZnS core shell QDs synthesised via a simple, non-phosphine and one pot synthetic method in the absence of an inert atmosphere is reported. Optical analysis confirmed that the as-synthesised CdSe/ZnS QDs were of high quality with sharp absorption peaks, bright luminescence, narrow emission width and high PL quantum yield (up to 74 %). The electron microscope images showed that the QDs are small and spherical in shape with narrow size distributions while the HRTEM micrograph confirmed the high crystallinity of the material. The Raman analysis of the QDs revealed the formation of core-shell structure.

3.4.4. PMMA CdSe/ZnS core-shell polymer nanocomposites.

3.4.4.1. Photoluminescence spectroscopy

The emission spectrum of the PMMA-CdSe/ZnS core-shell nanocomposite is given in Figure 3.24(A). The PMMA emission peak occurs at 393 nm. This shows a sharp increase after the dispersion of the CdSe\ZnS QDs in the polymer. The PL emission peak of the PMMA-CdSe/ZnS composite appears at 562 nm. This enormous shift in the emission maxima position is attributed to the presence of the QDs in the polymer. Song and Lee had shown that the colour purity is related to the FWHM of the peak of interest (Song & Lee, 2007). The narrower the FWHM is, the purer the colour becomes. The as-prepared composite film shows a narrow emission bandwidth of ~38 nm indicating material with high colour purity. This is comparable with the FWHM of the QDs-polymer composite film (~35 nm) reported by Song and Lee. Their CdSe/ZnS QDs were prepared via the pyrophoric two pots conventional organometallic phosphine route and were dispersed in a mixture of PMMA, azobisisobutyronitrile (AIBN) and methymethacrylate (MMA). Figure 3.24(B) shows the image of the composite thin film under UV light. This increase in the emission wavelength and decrease in the FWHM of the composite compared to the CdSe/ZnS core-shell QDs (1 h sample) is attributed to the formation of a layer of PMMA over the QDs. The colour changes from colourless for the neat PMMA to a bright yellow for PMMA/CdSe/ZnS core-shell polymer nanocomposite thin film. This indicates that, the as-prepared QD–polymer composites can be applied to flexible coloured filters, full colour displays and for the fabrication of brand new solid state lighting devices.

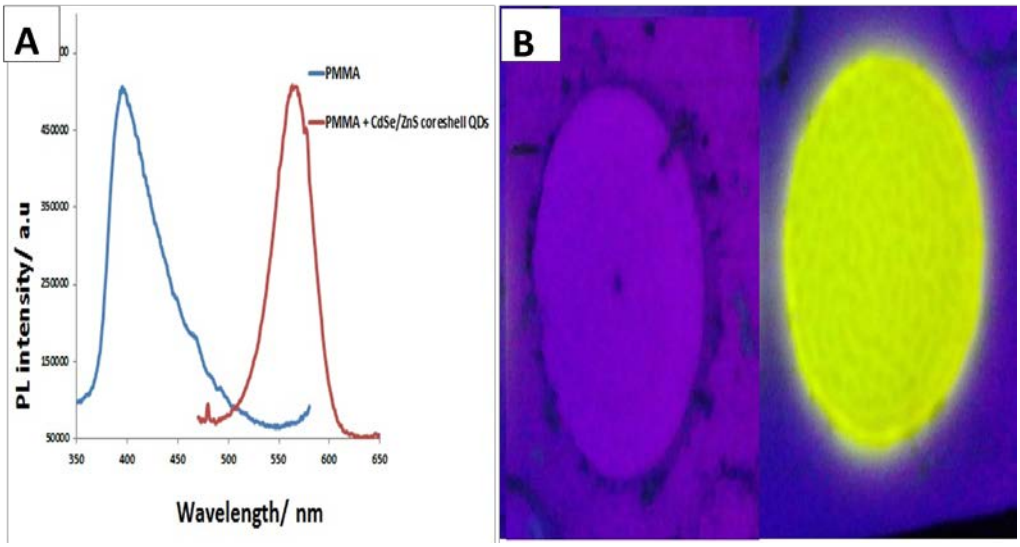

Figure 3.24: Emission spectra of PMMA and PMMA-CdSe/ZnS composite thin film (A) and image of PMMA-CdSe/ZnS composite thin film under fluorescence.

Summary: In this section, the fabrication of highly fluorescent yellow emitting nanophosphors using CdSe/ZnS quantum dots (QDs) dispersed in polymethyl methacrylate (PMMA) is explained. The dispersion of the core-shell QDs in PMMA matrix led to the red-shifting of the emission position from 393 nm in the neat PMMA to 592 nm in the nanocomposite. The fabricated highly fluorescent yellow emitting PMMA-CdSe/ZnS core-shell QDs polymer nanocomposite film display excellent optical properties without loss of luminescence. By dispersing the as-synthesized QDs in PMMA polymer matrix, highly luminescent yellow emitting polymer composite thin films were fabricated.

3.4.5. Synthesis of HDA capped CdSe quantum dots

3.4.5.1. Optical characterizations

3.4.5.1.1. UV-Visible and Emission spectroscopy

The absorption and emission spectra of HDA- capped CdSe QDs after 60 min reaction is given in Figure 3.25. Both the absorption and the emission maxima are blue-shifted from the bulk CdSe band gap due to quantum confinement effect. The UV spectrum show distinct excitonic features which can be attributed to the first electronic transition [$1S_{3/2}$ (h)–1S (e)] occurring in CdSe NPs. The absorption band-edge as calculated using the direct band gap method is. 2.49 (Pankove, 1990). The particle size as calculated using Yu's calibration data equation is 2.78 nm (Yu et al., 2003). The emission spectrum exhibit band-edge luminescence for excitation at 400 nm with the particle emitting in the orange region under the UV light. The symmetric and narrow emission width indicate that, the particle size and shape of the NPs are nearly uniform with few electronic defect. This is in good agreement with the TEM analysis. The emission position, width and intensity remain stable upon ageing under ambient conditions after one year. This indicate the stability of the material due to the effective passivation of the capping group.

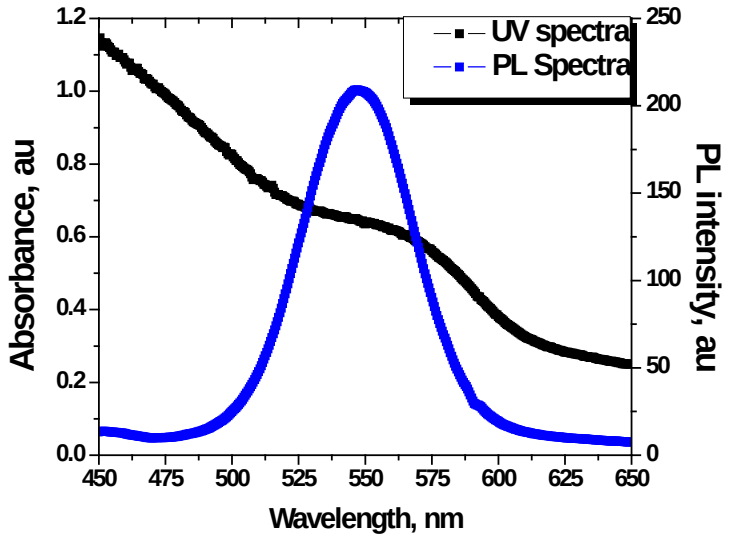

Figure 3.25: Absorption spectra and emission spectra of HDA capped CdSe at 60 minutes reaction time.

3.4.5.1.2 Fourier transform infrared spectroscopy

The surface morphology of the as-synthesised HDA- capped CdSe NPs was investigated using FTIR spectroscopy. FTIR spectrum of the as-synthesized QDs are shown in Figure 3.26. The peaks at 3334 cm^{-1} is assigned to -N-H stretching from amine group of HDA. Two major peaks at 2917 cm^{-1} and 2848 cm^{-1} are due to the $–CH_2$ symmetric stretching of the aliphatic group from HDA (Oluwafemi & Revaprasadu, 2008). A major peak at 1468 cm^{-1} is attributed to the $–CH_2$/-CH_3 bending vibrations from HDA. As compared to the IR spectrum of pure HDA, IR bands of HDA-capped CdSe NPs shifted to higher frequencies which may be due to the coordination of amine to the CdSe nanocrystallites (Trindade et al., 1997). The presence of these peaks confirmed successful capping of the QDs by the hexadecylamine.

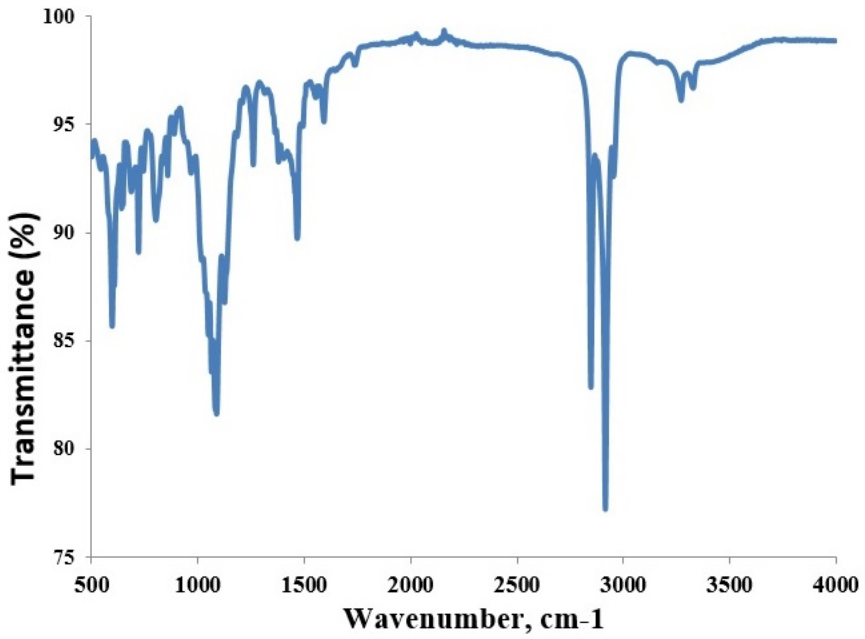

Figure 3.26: FT-IR spectra of HDA -capped CdSe QDs.

3.4.5.1.3. Raman spectroscopy Analysis

The Raman spectrum of HDA-capped CdSe QDs is given in Fig. 3.27. Compared to the oleic acid capped CdSe quantum dots, there was no major change in the Raman peaks despite the change in the capping agent. CdSe longitudinal optic phonons, ie the LO phonons are seen at 215 cm^{-1}. The high-order Raman peaks are also observed showing multi phonon scattering: 2LO1, the second-order phonon frequency of CdSe is located at 460 cm^{-1} and the third order phonon frequency of CdSe 3LO1 is located at 620 cm^{-1}. The significant peak at 520 cm^{-1} is due to the Si from the glass cuvette.

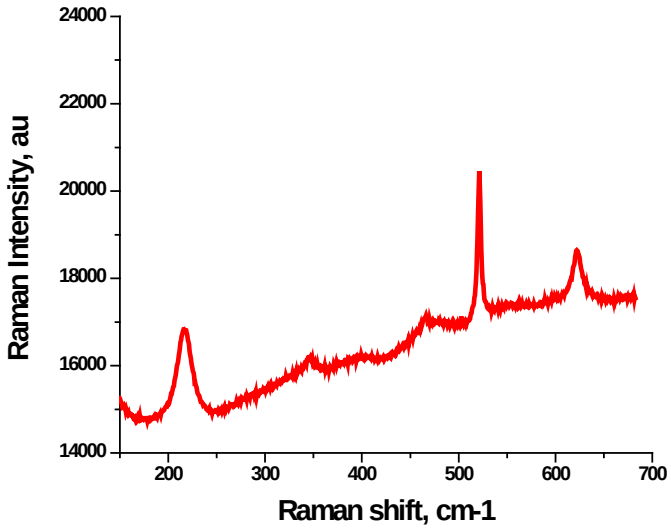

Figure 3.27: Raman spectra of HDA -capped CdSe QDs.

3.4.5.2. Morphological characterizations

3.4.5.2.1. High Resolution transmission electron microscopic analysis

The TEM images of the as-prepared HDA-CdSe QDs is shown in Fig 3.28. The particles are spherical in shape and mono dispersed. The size distribution curve shows that the particle size are within the range of 1.7 to 4.3 nm with average particle diameter of 2.67 ± 0. 43 nm. This particle size corroborates the size calculated using optical measurements. The HRTEM image 3.28 (B) revels that the particles are highly crystalline.

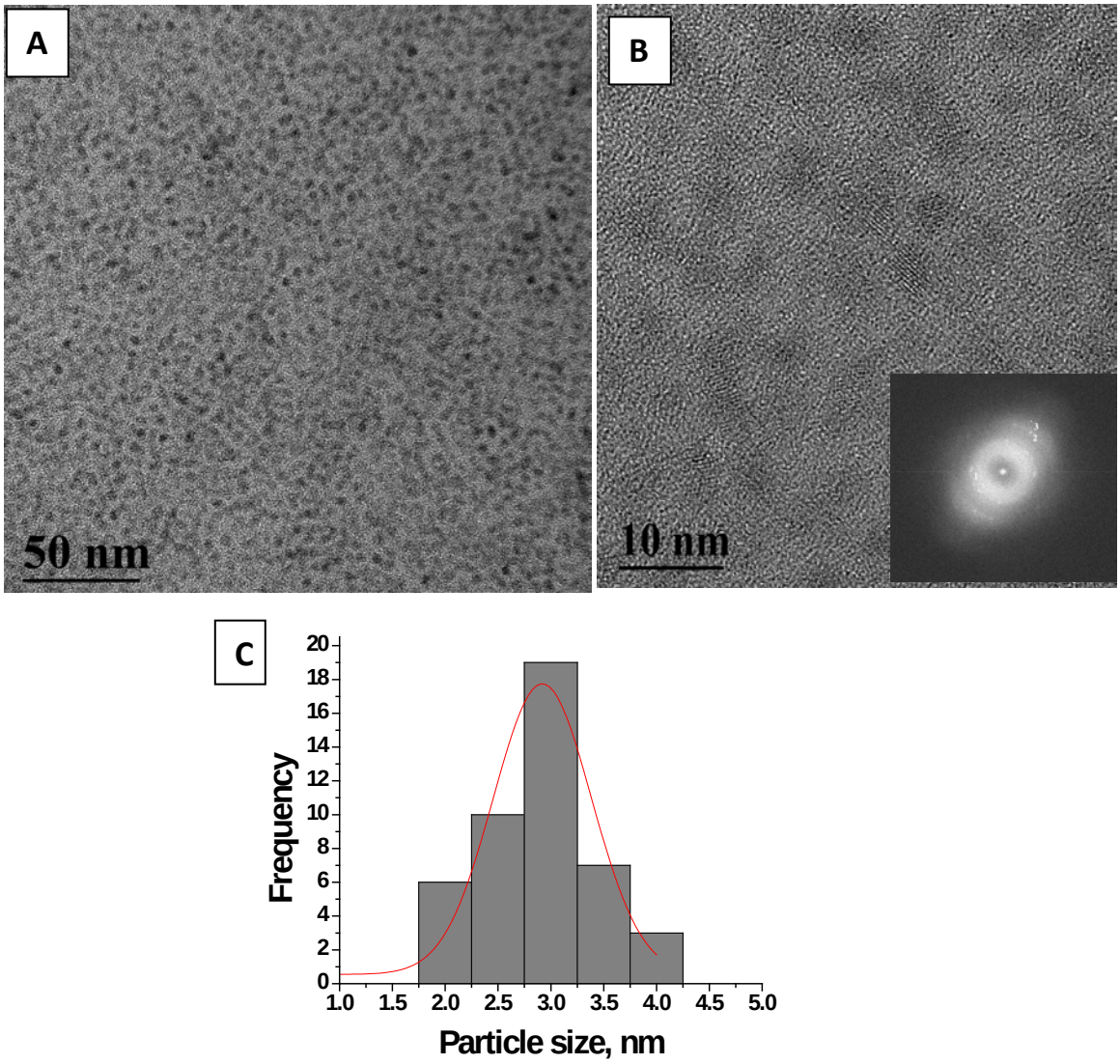

Figures 3.28: TEM image of (A) organic soluble HDA-CdSe QDs (B) HRTEM image of HDA-CdSe (inset SAED image) and (C) size distribution curves of HDA-CdSe QDs.

3.4.5.2.2. Energy dispersive spectroscopy

The EDX spectrum in Fig. 3.29 confirms the presence of respective elements in the as synthesized samples

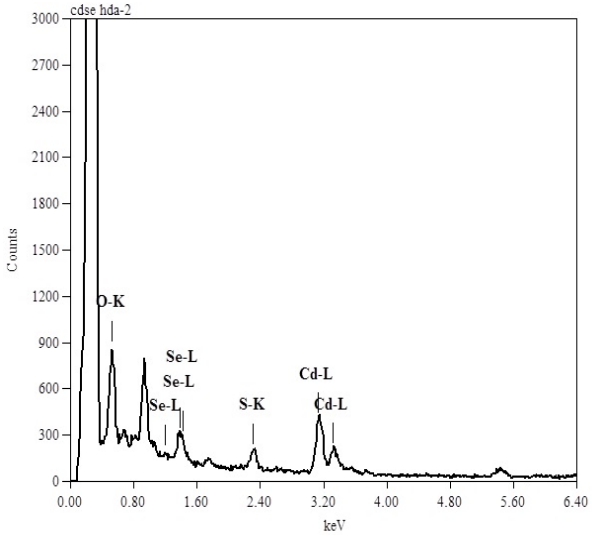

Figures 3.29: EDX spectrum of HDA-CdSe QDs

3.4.5.2.3. X-ray diffraction analysis.

The typical XRD spectrum of the HDA-capped CdSe QDs is given in Figure 3.30. The XRD pattern of the HDA- CdSe nanocrystals shows two distinct diffraction peaks at 2Ɵ values of 38.4 and 44.52, respectively, corresponding to the (102) and (220) crystalline planes of cubic-blende CdSe .

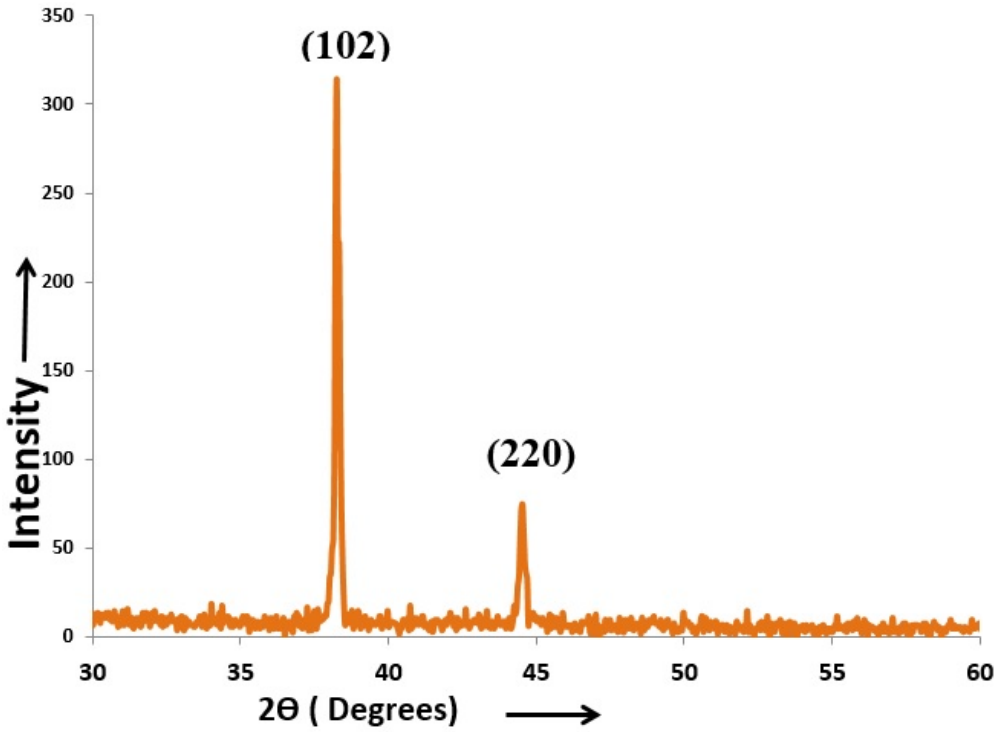

Figure 3.30: X-ray diffraction pattern of HDA-CdSe QDs.

Summary: In this section, the synthesis of small, highly crystalline, monodispersed, HDA capped CdSe QDs via a simple non organometallic and non-TOP based method is reported. The absorption spectrum show that the material possess good optical property while the XRD analysis indicates that the material is of cubic blende structure. The TEM image show that they are monodispersed and highly crystalline spherical nanoparticles (NPs). The FTIR spectra confirmed the capping of the as-synthesised material by HDA while the EDS confirmed the presence of the respective elements.

3.4.6 Synthesis of electrospun polycaprolactone-HDA capped CdSe nanofibres

3.4.6.1. Morphological characterization

3.4.6.1.1 Scanning electron microscopy

The SEM image of the as synthesized PCL-HDA-CdSe nanocomposite nanofibre is given in Fig. 3.31 (A). The fibers obtained were without any bead formation which shows that the viscosity of the QDs-polymer conjugate solution used is suitable for the formation of good fibres. The fiber diameters obtained are non-uniform. The average fiber diameter was found to be 518.96 ± 186 nm (Fig. 3.31 B).

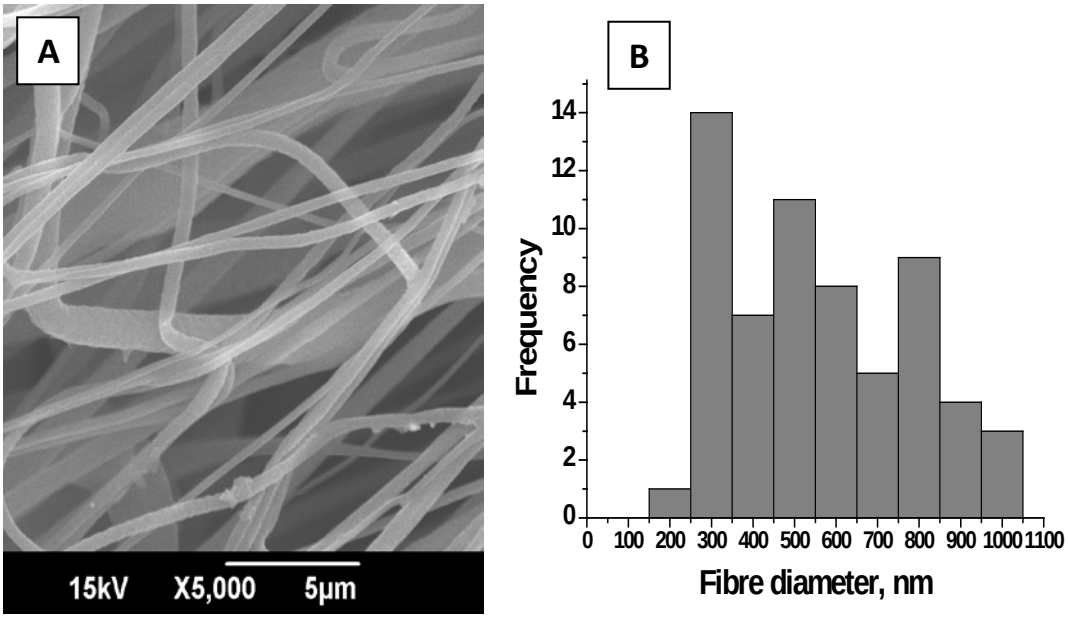

Figure 3.31: (A) SEM image of electrospun PCL-HDA capped CdSe nanocomposite nanofibre (B) size distribution of the electrospun nanofibres.

3.4.6.2 Fourier transform infrared spectroscopy

The FTIR spectrum of neat PCL, HDA-CdSe and PCL-CdSe nanocomposite fibres are given in Figure 3.32. The PCL spectrum shows a very strong band of (–C=O) carbonyl stretching mode around 1727 cm^{-1}. The peak at 2929 cm^{-1} and 2855 cm^{-1} are attributed to the asymmetric –C-H stretching and symmetric –C-H stretching respectively. The peak at 723 cm^{-1} is due to –C-H rocking vibration of the alkanes. The three additional peaks at 3332 cm^{-1}, 1647 cm^{-1} and 1565 cm^{-1} in PCL composite nanofibre indicated the presence of -N–H, C=O (amide I) and -N–H (amide II) respectively. The spectrum of the nanocomposite shows decrease in intensity for some of the peaks indicating the interaction of the polymer with the nanoparticles inside the matrix.

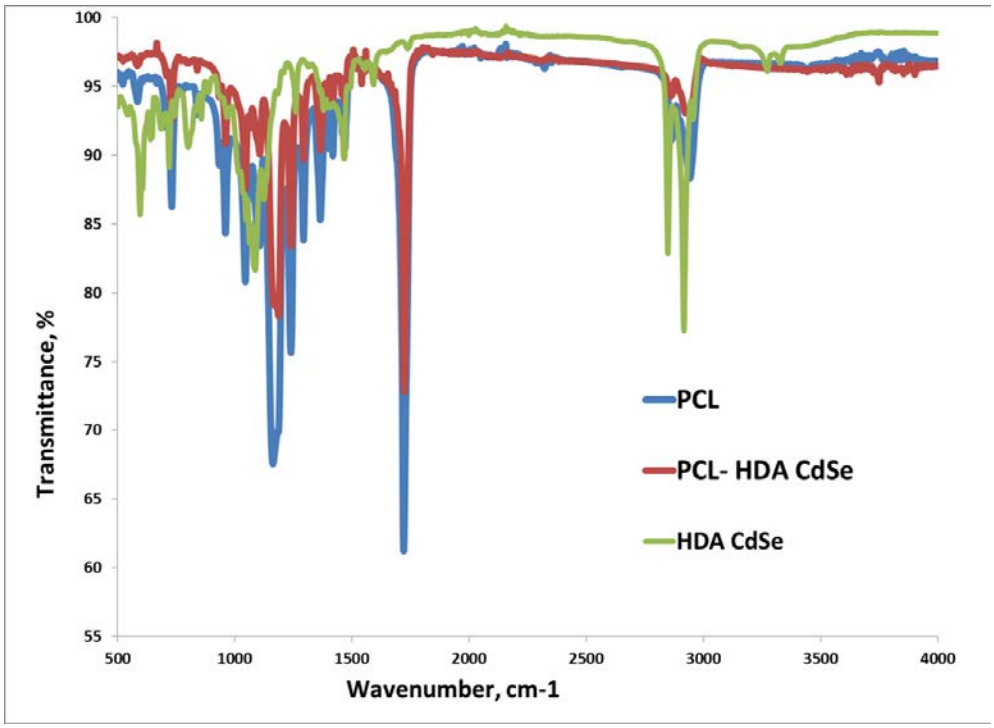

Figure 3.32: FTIR spectrum of neat PCL, HDA-CdSe and PCL-HDA-CdSe nanocomposite nanofibre.

The as-prepared polymer nanocomposite nanofibre thin films were observed under the UV light and the PCL-HDA-CdSe nanofibre gave a reddish orange fluorescent which confirms the presence of HDA-capped CdSe NPs inside the polymer matrix, while neat PCL doesn't show any fluorescence as shown in Fig. 3.33 A & B.

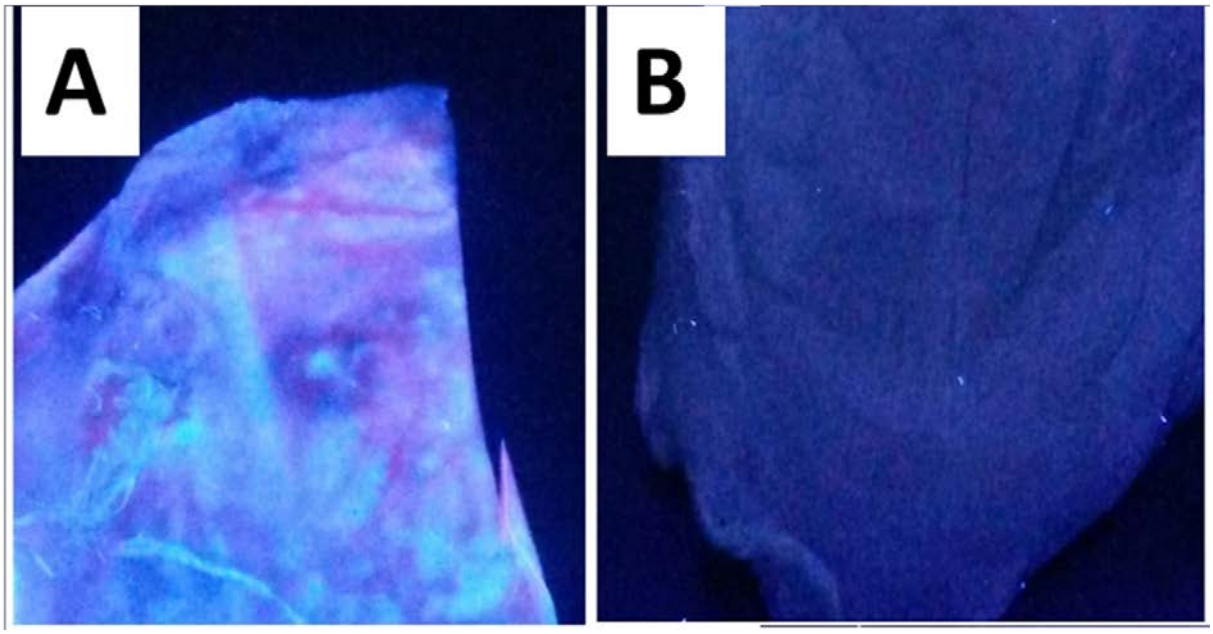

Figure 3.33: (A) Neat PCL nanofibre film (B) PCL-HDA-CdSe nanocomposite nanofibre film under UV light.

Summary: Preparation of fluorescent electrospun nanocomposite nanofibres using polycaprolactone and HDA-CdSe is explained in this section. The formation of the fibre was confirmed from the SEM images obtained. The incorporation of QDs into the polymer matrix was confirmed using FTIR.

3.4.7 Conversion of organic soluble quantum dots to water soluble – Ligand exchange

3.4.7.1. Optical characterizations

The Absorption and emission spectra of the MUA -capped water soluble CdSe/ZnS QDs is shown in Figure 3.34. The absorption and emission maxima are at 552 nm and 557 nm respectively. The slight blue shift in the absorption and emission maxima position of the water soluble compared to the organic –capped core-shell QDs (Abs.555.2 nm and Em.558.5) is attributed to the redistribution of the electronic density and increase in the quantum confinement energy of the water soluble QDs. This is due to the strong bonding of the thiol functionalities (from MUA) over the QDs surface after ligand exchange. Similar observation has been reported recently by Seo et al., for the dispersion of commercial CdSe/ZnS QDs in silicon hydride (Seo et al., 2014). The CdSe/ZnS core-shell retained its optical properties after ligand exchange with MUA. Several reports had shown that retention of the emission property after ligand exchange is a major problem as most of the reported high quality QDs usually lose most or all of their emission properties after surface modification. Thus, this synthetic route for organically soluble QDs is very promising for synthesizing high quality water soluble QDs.

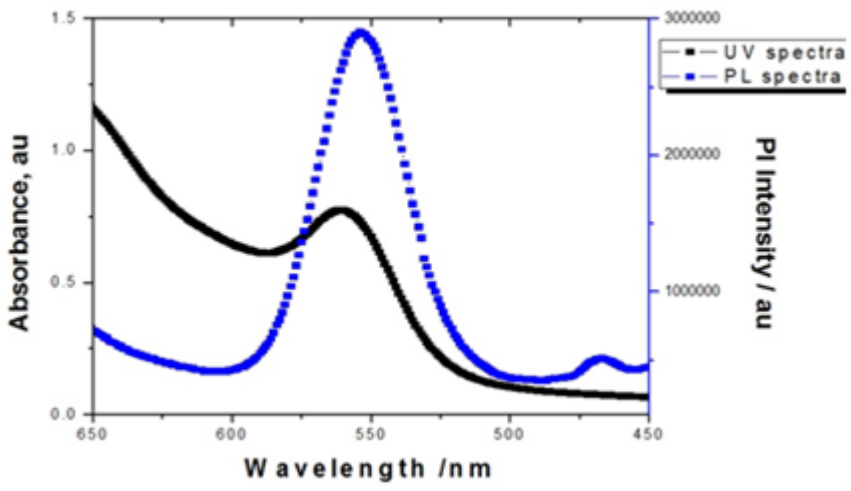

Figure 3.34: Absorption and emission spectra of water soluble MUA capped CdSe/ZnS core-shell QDs.

3.4.7.2. Morphological characterization

3.4.7.2.1. High Resolution transmission electron microscopic analysis

The typical TEM image and size distribution of the MUA capped CdSe/ZnS QDs are given in Figure 3.35. The TEM image (Fig. 8A) shows that the water soluble QDs are, small and spherical in shape with narrow size distribution. The water soluble QDs show a tendency to form oriented alignments. This may be due to the change in the zeta potential of the nanoparticles due to the change in their surface interaction. With organic moieties like oleic acid, the degree of repulsion between two particles is high which in turn results in high zeta potential value and stability. When the oleic acid ligand is replaced with MUA, there is possibility for more interaction due to hydrogen bonds formed by the carboxyl group present on the outer end of the ligand. This will cause a change in zeta

potential to a lower value and this may result in the alignment of the nanoparticles. The size distribution curve (Figure 3.35 B) indicates that the water soluble CdSe/ZnS QDs are within the range of 0.5 nm to 3.5 nm with an average diameter of 1.97 ± 0.74 nm. The lower particle size obtained when compared with the TEM micrograph of the organically-capped CdSe/ZnS core-shell is consistent with the optical analysis results discussed earlier.

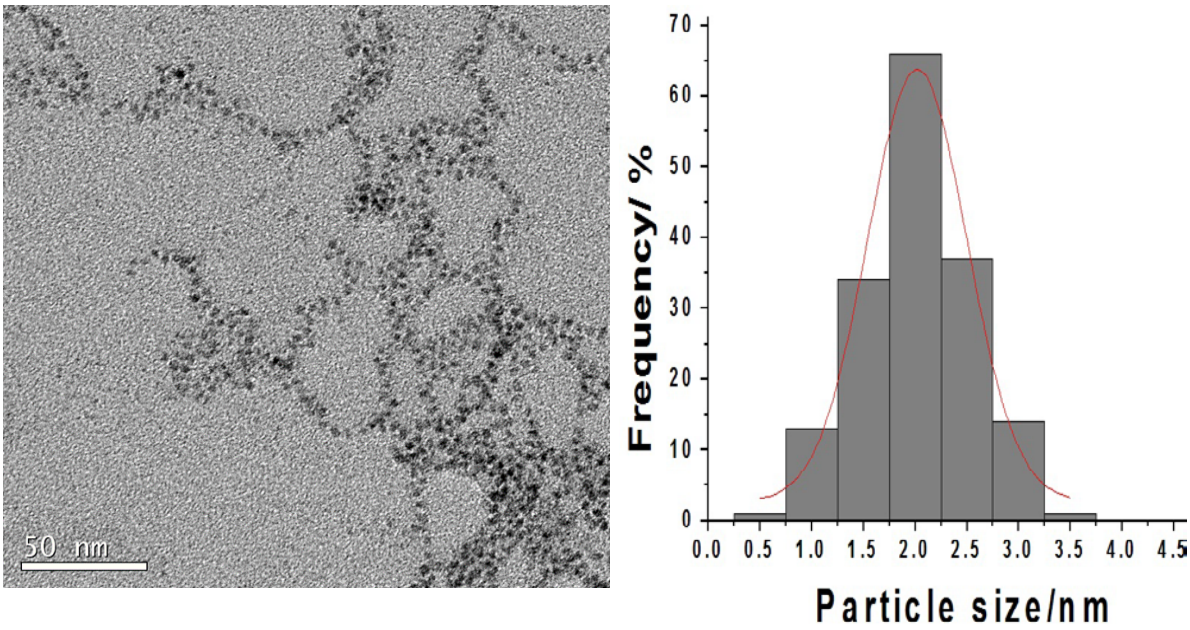

Figure 3.35: (A) TEM images of MUA capped water soluble CdSe/ZnS QDs and (B) its size distribution curves.

3.4.7.3 Fourier transform infrared spectroscopy analysis

The FTIR spectrum of the water soluble core-shell QDs is given in Figure 3.36. The broad peak observed at 3400 cm^{-1} clearly indicates the C-O-H stretching vibrations of the carboxylic group of the MUA. The characteristic peak of the –S-H stretching at 2550 cm^{-1}

is absent which shows that the MUA is successfully attached to the surface of the QDs through the S-R bond.

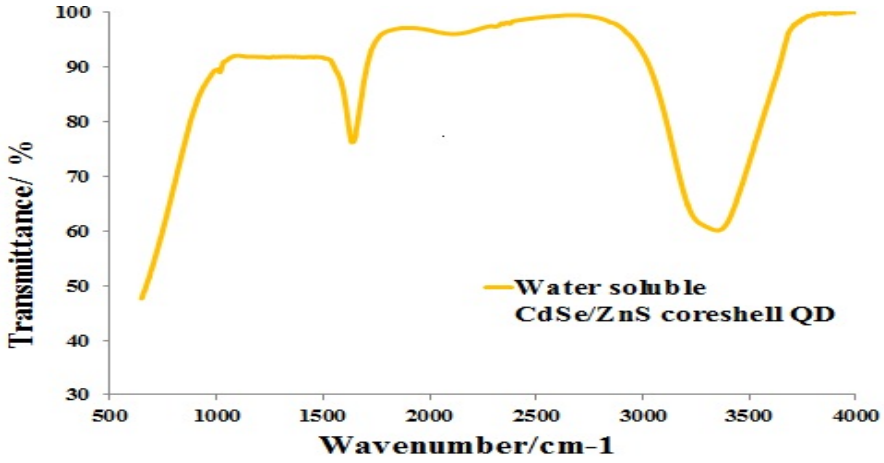

Figure 3.36: FTIR spectrum of water soluble CdSe/ZnS coreshell QDs.

A schematic representation showing the strategy of the ligand substitution is given in Fig. 3.37. This mainly involves the substitution of the native organic cap using bi-functional hydrophilic ligands.

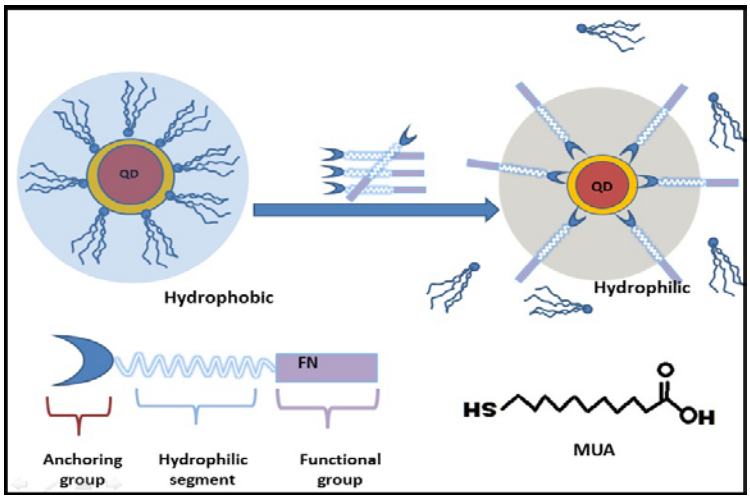

Figure 3.37: Schematic representation showing ligand exchange strategy between QDs and MUA.

Summary: Synthesis of fluorescent water soluble CdSe/ZnS core-shell quantum dots through ligand exchange is explained here. The reaction is simple and was carried out at room temperature. The optical characterization revealed that the as synthesized particles retained the absorption and emission properties of the parent organic soluble core-shell nanoparticles. The TEM images showed small, spherical and aligned nanoparticles with narrow size distribution.

3.5 Conclusions

As an effort to introduce more green synthetic methods, highly fluorescent semiconductor core-multi shell quantum dots were synthesized using ecofriendly reagents without the presence of any inert atmosphere. The optical and morphological characterization showed that the as- synthesized QDs have good optical properties and they are morphologically distinct and stable. Considering the significance of these materials in various applications, polymer nanocomposites using QDs were prepared and characterized. Highly crystalline and monosdispersed CdSe/CdS/ZnS core-multi shell quantum dots with high fluorescent lifetime were synthesized using hot precursor injection techniques. The TEM and HRTEM results revealed the crystallinity of the material. The core-multi shell QDs were successfully dispersed in Epoxy polymer matrix which imparted fluorescence to the composite. The well dispersion of QDs inside the polymer matrix was confirmed by the TEM image of the composite.

Highly fluorescent yellow emitting CdSe/ZnS nanophosphors was successfully fabricated. The CdSe/ZnS QDs were synthesized via a simple and environmentally friendly method. The core-shell QDs were small, monodispersed and highly fluorescent with narrow

FWHM and high quantum yield. The dispersion of the CdSe/ZnS QDs in PMMA led to the fabrication of yellow emitting CdSe/ZnS QD–PMMA polymer composite film. The fabricated yellow emitting CdSe/ZnS QD–PMMA composite film gave good optical properties without luminescence quenching.

Synthesis of crystalline, monodispersed HDA-capped CdSe QDs using an inexpensive and environmentally benign non-organometallic route is also reported. The structural analysis reveals that the materials are highly crystalline with cubic-blende phases. The EDS confirmed the presence of the corresponding elements. Biocomposite nanofibre was prepared using HDA-CdSe dispersed in a biopolymer, polycaprolactone for their possible use in biomedical field as luminescent sensors.

Furthermore, as a model reaction, the as-synthesized organically soluble CdSe/ZnS QDs were successfully converted into highly water soluble QDs using 11-mercaptoundecanoic without the loss of their emission property through ligand exchange. This method is very useful to produce water soluble luminescent QDs which is important for their use in biological systems.

References

Ananthakumar, S., Ramkumar, J. & Moorthy Babu, S. 2014. Synthesis of thiol modified CdSe nanoparticles/P3HTblends for hybrid solarcell structures. *Mater Sci Semicond Process*, 22: 44-49.

Bailes, J., Vidal, L., Ivanov, D.A. & Soloviev, M. 2009. Quantum dots improve peptide detection in MALDI MS in a size dependent manner. *J Nanobiotechnology* 7: 10.

Basaran, C., Nie, S., Hutchinson, C. & Ergun, H. 2006. Failure mechanism in PMMA/ATH acrylic casting dispersion. *J. Mech.Behav. Mater*., 17: 79-95.

Borrelli, N.F., Hall, D.W., Holland, H.J. & Smith, D.W. 1987. Quantum confinement effects of semiconducting microcrystallites in glass. *J Appl Phys*., 61:5399–5409.

Bruchez, M.J., Moronne, M., Gin, P., Weiss, S. & Alivisatos, A.P. 1998. Semiconductor nanocrystals as fluorescent biological labels. *Science*, 281: 2013-2016.

Bullen, C.R. & Mulvaney, P. 2004. Nucleation and Growth Kinetics of CdSe Nanocrystals in Octadecene. *Nano.Lett* .,4: 2303-2307.

Challa, K.K., Goswami, S.K., Oh, E. & Kim, E. 2011. Effect of CdS film thickness on the photoexcited carrier lifetime of TiO_2/CdS core-shell nanowires. *Appl Phys Lett*., 99: 153111.

Chan, W.C.W. & Nie, S. 1998. Quantum Dot Bioconjugates for Ultrasensitive Nonisotopic Detection. *Science*, 281: 2016-2018.

Chen, C.C., Yet, C.P, Wang, H.N. & Chao, C.Y. 1999. Self-Assembly of Monolayers of Cadmium Selenide Nanocrystals with Dual Color Emission. *Langmuir*, 15: 6845-6850.

Chen, X.B., Lou, Y.B., Samia, A.C. & Burda, C. 2003. Coherency Strain Effects on the Optical Response of Core/Shell Heteronanostructures. *Nano Lett*, 3: 799-803.

Correa-Duarte, M.A., Giersig, M. & Liz-Marzan, L.M. 1998. Stabilization of CdS semiconductor nanoparticles against photodegradation by a silica coating procedure. *Chem Phys Lett.*, 286: 497-501.

Cumberland, S.L., Hanif, K.M., Javier, A., Khitrov, G.A., Strouse, G.F., Woessner, S. M., & Yun, C. S. 2002. Inorganic Clusters as Single-Source Precursors for Preparation of CdSe, ZnSe, and CdSe/ZnS Nanomaterials. Chem. Mater. 14: 1576-1584.

Dabbousi, B.O., Rodriguez-Viejo, J., Mikulec, F.V., Heine, J.R., Mattoussi, H., Ober, R., Jensen, K. F. & Bawendi, M.G. 1997. (CdSe)ZnS Core−Shell Quantum Dots: Synthesis and Characterization of a Size Series of Highly Luminescent Nanocrystallites. *J Phys Chem B,* 101: 9463-9475.

Danek, M., Jensen, K.F., Murray, C.B. & Bawendi, M.G. 1996. Synthesis of Luminescent Thin-Film CdSe/ZnSe Quantum Dot Composites Using CdSe Quantum Dots Passivated with an Overlayer of ZnSe. *Chem Mater.*, 8: 173-180.

Deng, Z. T., Cao, L., Tang, F.Q. & Zou, B.S. 2005. A New Route to Zinc-Blende CdSe Nanocrystals: Mechanism and Synthesis. *J. Phys. Chem. B,* 10:9: 16671-16675.

Dzhagan, V.M., Valakh, M.Y., Raevskaya, A.E., Stroyuk, A.L., Kuchmiy, S.Y. & Zahn, D.R.T. 2008. Characterization of semiconductor core–shell nanoparticles by resonant Raman scattering and photoluminescence spectroscopy. *Appl. Surf. Sci.* 255: 725–727.

Hall, D.W. & Borrelli, N.F.1988. Absorption saturation in commercial and quantum-confined CdSexS1-X-doped glasses. *J Opt Soc Am* B, 5:1650–1654.

Hines, M.A. & Guyot-Sionnest, P. 1996. Synthesis and Characterization of Strongly Luminescing ZnS-Capped CdSe Nanocrystals. *J Phys Chem B,* 100: 468-471.

Jasieniak, J., Bullen, C.R., Embden, J. & Mulvaney, P. 2005. Phosphine-Free Synthesis of CdSe Nanocrystals. *J. Phys. Chem. B,* 109: 20665-20668.

Kazes, M., Saraidarov, T. & Banin, U. 2009. Organic–Inorganic Sol–Gel Composites Incorporating Semiconductor Nanocrystals for Optical Gain Applications. *Adv. Mater*., 21: 1716-1720.

Khani, O., Rajabi, H. R., Yousefi, M.H., Khosravi, A.A., Jannesari, M. & Shamsipur, M. 2011. Synthesis and characterizations of ultra-small ZnS and Zn(1−x)FexS quantum dots in aqueous media and spectroscopic study of their interactions with bovine serum albumin. *Spectrochim. Acta, Part A,* 79: 361-369.

Klein, M.C., Hache, F., Ricard, D. & Flytzanis, C. 1990. The size dependence of electron-phonon coupling in semiconductor nanospheres: the case of CdSe. *Phys. Rev. B,* 42:11123-11132.

Kortan, A.R., Hull, R., Opila, R.L., Bawendi, M.G., Steigerwald, M. L., Carroll, P.J., Brus, L.E. 1990. Nucleation and growth of cadmium selendie on zinc sulfide quantum crystallite seeds, and vice versa, in inverse micelle media. *J Am Chem Soc.*, 112: 1327-1332.

Lee, C. W., Chou, C.H., Huang, J.H. & Nguyen, T.P. 2008. Investigations of organic light emitting diodes with CdSe (ZnS) quantum dots. *Mat. Sci. Eng. B Solid,* 147: 307-311.

Lee, S.J., Muthiah, M., Lee, H.J. & Moon, M. 2012. Synthesis and characterization of magnetic nanoparticle-embedded multi-functional polymeric micelles for MRI-guided gene delivery. *Macromol Res.,* 20: 188-196.

Leschkies, K.S., Norris, D.J. & Aydil, E.S. 2007. Photosensitization of ZnO nanowires with CdSe quantum dots for photovoltaic devices. *Nano Lett.,* 7:1793-1798.

Li, J.J., Wang, Y.A., Guo, W.Z., Keay, J.C., Mishima, T.D., Johnson, M.B. & Peng, X.G. 2003. Large-Scale Synthesis of Nearly Monodisperse CdSe/CdS Core/Shell Nanocrystals Using Air-Stable Reagents via Successive Ion Layer Adsorption and Reaction. *J Am Chem. Soc.,* 125: 12567-12575.

Li, Y.Q., Fu, S.Y., Yang, Y. & Mai, Y.W. 2008. Facile Synthesis of Highly Transparent Polymer Nanocomposites by Introduction of Core–Shell Structured Nanoparticles. *Chem. Mater*., 20:2637-2643.

Li, Y.Q., Yang, Y. & Fu, S.Y. 2008. Significant Enhancements in the Fluorescence and Phosphorescence of ZnO Quantum Dots/SiO_2 Nanocomposites by Calcination. *J. Phys. Chem. C*, 112:17397-17401.

Lim, J., Jun, S., Jang, E., Baik, H., Kim, H. & Cho, J. 2007. Preparation of highly luminescent nanocrystals and their application to light-emitting diodes. *Adv Mater.,* 19: 1927– 1931.

Littau, K.A., Szajowski, P.J., Muller, A.J., Kortan, A. R. & Brus, L.E. 1993. A luminescent silicon nanocrystal colloid via a high-temperature aerosol reaction. *J Phys Chem.,* 97: 1224-1230.

Mitchell, G.P., Mirkin, C.A. & Letsinger, R.L. 1999. Programmed assembly of DNA functionalized quantum dots. *J Am Chem Soc.,* 121: 8122-8123.

Mohan, S., Oluwafemi, O. S., Songca, S.P., Osibote, O.A., George, S.C., Kalarikkal, K. & Thomas, S. 2014. Facile synthesis of transparent and fluorescent epoxy–CdSe–CdS–ZnS core–multi shell polymer nanocomposites. *New J. Chem*., 38:155-162.

Novak, B.M. 1993. Hybrid Nanocomposite Materials—between inorganic glasses and organic polymers. *Adv. Mater*., 5: 422-433.

Oluwafemi, O.S. & Revaprasadu, N. 2008. A new synthetic route to organically capped cadmium selenide nanoparticles. *New J. Chem*., 10: 1432–1437.

Ouyang, J.Y., Zaman, M.B., Yan, F.J., Johnston, D., Li, G., Wu, X.H., Leek, D., Ratcliffe, C.I., Ripmeester, J.A., Yu, K. 2008. Multiple Families of Magic-Sized CdSe Nanocrystals with Strong Bandgap Photoluminescence via Non injection One-Pot Syntheses. *J. Phys. Chem. C*, 112: 13805-13811.

Pankove, J.I. 1990. MRS Symp Proc, 162: 515.

Peng, X.G., Schlamp, M.G., Kadavanich, A.V. & Alivisatos, A.P. 1997. Epitaxial Growth of Highly Luminescent CdSe/CdS Core/Shell Nanocrystals with Photostability and Electronic Accessibility. *J Am Chem Soc*., 119: 7019-7029.

Rogach, A.L., Dattatri, N., Ostrander, J.W., Giersig, M. & Kotov, N.A. 2000. "Raisin Bun"-Type Composite Spheres of Silica and Semiconductor Nanocrystals. *Chem Mater.*, 9: 2676-2685.

Schlamp, M.C., Peng, X.G. & Alivisatos, A.P. 1997. Improved efficiencies in light emitting diodes made with CdSe(CdS) core/shell type nanocrystals and a semiconducting polymer. *J Appl Phys.*, 82: 5837–5842.

Seo, Y.S., Raj, C.J., Kim, D.J., Kim, B.C. & Yu, K.H. 2014. Effect of CdSe/ZnS quantum dots dispersion in silicone based polymeric fluids. Mater. *Lett*., 130: 43-47.

Serenko,O., Goncharuk, G. & Bazhenov, S. 2002. Deformability of particle- filled composites at brittle fracture. *Dokl. Phys*., 47: 822 -824.

Siakavellas, M., Kontos, A.G. & Anastassakis, E. 1998. Strain dependent optical phonon frequencies of cubic ZnS. *J. Appl. Phys*., 84: 517 -521.

Somers, R.C., Bawendi, M.G. & Nocera, D.G. 2007. CdSe nanocrystal based chem-/bio-sensors. *Chem Soc Rev.*, 36: 579–591.

Song, H. & Lee, S. 2007. Photoluminescent (CdSe)ZnS quantum dot–polymethyl methacrylate polymer composite thin films in the visible spectral range. *Nanotechnology*, 18: 055402.

Sperling, R.A. & Parak, W.J. 2010. Surface modification, functionalization and bioconjugation of colloidal inorganic nanoparticles. *Phil Trans R Soc A,* 368: 1333–1383.

Sun, D.Z., Sue, H.J. & Miyatake, N. 2008. Optical Properties of ZnO Quantum Dots in Epoxy with Controlled Dispersion. *J. Phys. Chem. C,* 112: 16002-16010.

Suwanprateeb, J. 2000. Instrumented impact behaviour of particulate filled composites. *Polym. Plast. Technol. Eng.*, 39: 83-94.

Talapin, D.V., Mekis, I.,Gotzinger,S., Kornowski, A., Benson, O. & Weller, H. 2004. CdSe/CdS/ZnS and CdSe/ZnSe/ZnS Core−Shell−Shell Nanocrystals. *J Phys Chem B*, 108: 18826-18831.

Trindade, T., Brien, P.O. & Zhang, X. 1997. Synthesis of CdS and CdSe Nanocrystallites Using a Novel Single-Molecule Precursors Approach. *Chem. Mater.,* 9: 523-530.

Uddin, M.A. & Chan, H.P. 2008. Materials and process optimization in the reliable fabrication of polymer photonic devices. *J Optoelectron Adv Mater.,* 10: 1.

Vega Macotela L.G., Torchynska, T.V., Douda, J. & Peña Sierra, R. 2010. Variation of Raman spectra of CdSe/ZnS quantum dots at the bioconjugation. *Phys. Status Solidi C,* 7(3–4): 1192– 1195

Wageh, S., Shu-Man, L., You, F.T. & Xu-Ronga, X. 2003. Optical properties of strongly luminescing mercaptoacetic-acid-capped ZnS nanoparticles. *J. Lumin*., 2003, 102, 768-773.

Wang, X., Li,W. & Sun,K. 2011. Stable efficient CdSe/CdS/ZnS core/multi-shell nanophosphors fabricated through a phosphine-free route for white light-emitting-diodes with high color rendering properties. *J. Mater. Chem*., 21: 8558-8565.

Yu, W.W., Qu, L., Guo, W., Peng, X. 2003. Experimental Determination of the Extinction Coefficient of CdTe, CdSe, and CdS Nanocrystals. *Chem Mater.,* 15: 2854-2860.

Yuan, Q. & Misra, R.D.K. 2006. Impact fracture behavior of clay–reinforced polypropylene nanocomposites. *Polymer,* 47:4421-4433.

Zhang, L., He, R. & Gu, H. 2006. Oleic acid coating on the monodisperse magnetite nanoparticles. *Appl. Surf. Sci.,* 253: 2611-2617.

Zhao, Y., Yan, Z., Liu, J. & Wei, A. 2013. Synthesis and characterization of CdSe nanocrystalline thin films deposited by chemical bath deposition. *Mater Sci Semicond Process,* 16: 1592-1598..

Zou, W., Du, Z., Li, H. & Zhang, C. 2011. Fabrication of carboxyl functionalized CdSe quantum dots via ligands self-assembly and CdSe/epoxy fluorescence nanocomposites. *Polymer*, 52: 1938-1943.

Zou,W., Du, Z.J., Li, H.Q. & Zhang, C. 2010. Fabrication of surface-modified CdSe quantum dots by self-assembly of a functionalizable comb polymer. *Polym. Int.,* 60:751-757.

Chapter 4

Synthesis and characterization of biopolymer capped silver nanoparticles

4.1 Introduction

Noble metals in quantum size regime have generated a lot of interest among researchers from various disciplines over the last decades (Kim et al., 2007; Hermanson et al., 2001; Zhenhua et al., 2003; Jennifer et al., 2007). This is due to the unique and attractive, optical and electronic properties of metal nanoparticles (NPs) such as silver (Ag), gold (Au), platinum (Pt) etc. which is significantly different from those of bulk materials. These properties are being influenced by several parameters, most importantly their size and shape. Among these materials, interest in Ag- NPs is very high due to their outstanding plasmonic activity, bacterial inhibitory and bactericidal effects compared with the other metal nanoparticles. The design of Ag-NPs especially using the bottom-up technique has been widely investigated for various applications and researchers are continuously developing newer methods for the synthesis of highly monodispersed and stable nanoparticles. Conventionally, stable metal nanomaterials are synthesized using either chemical or physical methods. In chemical methods, reducing agents such as sodium borohydrides, hydroxylamine hydrochloride, trisodium citrates, dimethyl formamide etc are usually used (Lee & Meisel, 1982; Creighton et al., 1979). The two main problems normally associated with the chemical synthetic route are the aggregation of the nanoparticles formed and the toxicity of the reagents used. As part of developing eco-friendly method, in order to address these concerns, new synthetic route based on green chemistry principle are being developed (Raveendran et al., 2006; Bozanic et al., 2010).

Studies have shown that doping of metal nanoparticles in polymer matrices improves their stability (Godovsky, 1995; Beecroft & Ober, 1997). and potential applications in nanoelectronic devices, sensors, molecular optical devices, optoelectronic applications and engineering nanocomposites with well-defined properties (Schneider, 2001; Magdassi et al., 2003; Misiakos et al., 2004; Haes et al., 2005; Nie & Emory, 1997). There has been an upsurge interest in implementing green chemistry principles into the synthesis of silver nanoparticles in order to maximize safety and efficiency, and minimize environmental and societal impact of these materials. In the green synthesis of silver nanoparticles, three important factors to be considered are: (i) use of green solvents, (ii) use of an eco-friendly benign reducing agent, and (iii) use of a nontoxic material as a stabilizer. One of the green methods for preparing silver nanoparticles is the polysaccharide method. In this method, water is normally used as an eco-friendly benign solvent and polysaccharides as capping agents. Raveendran *et al*., 2003 reported the first completely green synthesis of Ag nanoparticles using water, starch and β-D-glucose as the solvent, capping agent and reducing agent respectively. The use of starch makes it possible to avoid the use of relatively toxic organic solvents. Based on the modification of this method, there has been several reported synthesis of Ag-NPs using different sugars as reducing agent (Panacek et al., 2006) and biopolymer such as starch (Batabyal et al., 2007), gelatin (Darroudi et al., 2011) polyvinylpyrolidone (PVP) (Filippo et al., 2010) and so on as passivating agent with or without accelerating agent such as NaOH (Darroudi et al, 2011; Stevanovic et al., 2011; Filippo et al., 2010). Oluwafemi *et. al*.,2013 also reported the synthesis of very small, highly stable and monodispersed Ag-NPs using maltose, a disaccharide sugar as reducing agent while gelatin and starch were used as passivating agent without the use of any accelerating agent. In another development, Eid and Azzay reported the synthesis of

anisotropic Ag-NPs using dextrose, trisodium citrate and NaOH as reducing agent, capping agent and accelerating agent respectively (Eid & Assay, 2012). Different sizes of robust hollow flower-like nanostructures were produced by changing the concentration of the $AgNO_3$, dextrose, NaOH and trisodium citrate. However, such capping and accelerating agent may be associated with environmental toxicity or biological hazards. In this context, synthesis of nanoparticles using completely green methods is highly significant.

Although, extensive studies have already been done on the green synthesis of silver nanoparticles, there are still many aspects of this synthetic route that still require attention in order to produce stable and efficient nanoparticles for various applications. Hence, we studied the synthesis of highly monodispersed, water soluble, stable and smaller sized biopolymer capped-silver nanoparticles (Ag-NPs) via a completely green method by using dextrose as reducing agent without any accelerating agent. Detailed optical and structural characterizations were done using UV-Visible spectroscopy, Raman spectroscopy, XRD, and TEM. Various applications of as synthesized silver nanoparticles were also analyzed which will be discussed in the following chapter.

4.2 Materials and Methods

4.2.1 Materials

All the chemicals were of analytical grade and used as purchased without any further purification. $AgNO_3$ was purchased from Alba CHEME, gelatin, starch and dextrose were from Merck. All glasswares used in the experiment were cleaned and washed thoroughly

with double distilled water and dried with acetone before use. A cultivating medium, Mueller-Hinton broth, used in the antibacterial assays was supplied by HIMEDIA CHENNAI. *Escherichia coli* ATCC 10536, and two *Pseudomonas aeruginosa* bacterial strains (PA 27853) and (PA.MDR) isolated from human clinical material were used. Human THP-1 monocyte cell line was obtained from American Type Culture Collection (ATCC, TIB-202TM, Manassas, VA, USA).

4.2.2 Method of synthesis

4.2.2.1 Synthesis of dextrose reduced gelatin capped Ag-NPs

For the synthesis of Ag-NPs, 1.0 g of gelatin was added to 95 mL of distilled water in a round bottom flask and heated at 40 ^{o}C to get a clear solution. 0.07 M (10 mL) dextrose solution was added to the gelatin solution followed by the addition of aqueous $AgNO_3$ (5 mL, 1M) under continuous stirring to obtain Ag^{+}/gel-sol. The reaction was maintained at 70 ^{o}C and allowed to continue for several hours. Aliquots were taken at different time intervals to monitor the growth of the particles.

4.2.2.2 Synthesis of dextrose reduced starch-capped Ag-NPs

In a typical reaction, 1.0 g of starch was added to 95 mL of distilled water in a round bottom flask and warmed to 40 ^{o}C to obtain a clear solution. 0.07 M (10 mL) dextrose solution was added to the starch solution followed by the addition of aqueous $AgNO_3$ (5 mL, 1 M) under continuous stirring. The reaction temperature was elevated to 70 ^{o}C and allowed to react for several hours. Aliquots were taken at different time intervals to monitor the growth of the particles.

4.2.3 Characterization techniques used

4.2.3.1 Ultraviolet-visible (UV-Vis) spectroscopy

The absorption properties of the as-synthesized materials were analysed by using SHIMDTH UV2401PC spectrophotometer at room temperature in the 300-700 nm wavelength range. The liquid samples were diluted and the measurements were taken in a quartz cuvette.

4.2.3.2 Fourier transform Infrared spectroscopy (FTIR)

Various functional group present in the biopolymer capped Ag-NPs were analysed using Fourier transform infrared spectroscopy (Nicolet-Nexus 670 FTIR spectrophotometer), by spanning along a frequency range from 400 to 4000 cm^{-1}.

4.2.3.3 Raman spectroscopy analysis

The Raman signature peaks of the nanoparticles were analysed using Horiba Jobin Vyon LabRAM HR at laser wavelength of 633 nm. The diluted samples were taken in a glass cuvette and scanned to get the significant peaks.

4.2.3.4 X-ray diffraction (XRD) analysis

The crystallinity of the materials synthesized was analyzed using XRD. XRD measurements were performed on the Bruker D8 Advance diffractometer operating in the reflection mode with Cu-Kα radiation (40 kV, 20 mA) at a wavelength of 1.5418 Å and diffracted beam monochromator. The samples for the XRD measurements were prepared by drying the sample and obtaining the powder. The particle size of the nanomaterial was calculated using Bragg's equation.

4.2.3.5 Energy dispersive x-ray spectroscopy (EDX) Analysis

Energy dispersive X-ray spectroscopy (EDX) system Oxford INCA Energy 200 Premium was used to analyse the material composition of the prepared nanoparticles.

4.2.3.6 High resolution transmission electron microscopic (HRTEM)

The detailed morphology and crystallinity analysis of the Ag-NPs were done by using JEOL JEM- 3010 electron microscope operating at 200 kV. The samples for TEM and HRTEM analyses were prepared by putting a drop of the solution of the Ag-NPs onto an amorphous carbon substrate supported on a copper grid and then allowing the solvent to evaporate at room temperature.

4.2.3.7 Antibacterial study

4.2.3.7.1 Evaluation of antibacterial activity of nanoparticles

Antibacterial activity was evaluated using disc diffusion method. 18 h Mueller Hinton broth (MHB) cultures of two clinical isolates of E. coli and P. aeruginosa were evaluated in this study. 10 mg of the compound was dissolved in 1 mL sterile milliQ water. 10 µL of the Ag-NPs solution was added on filter paper disc and dried at 300 ^{o}C in an incubator. A stock solution of $AgNO_3$ was made with same concentration and checked for the purpose of comparison. Strict aseptic conditions were maintained throughout the procedure. Bacterial cultures were swabbed on Mueller-Hinton agar (MHA) plate and surface of the media was allowed to dry for 30 mins, then the nanoparticles incorporated

discs were pressed gently on the agar surface at specified distance. Ciprofloxacin (5 µg) and imipenem (10 µg) discs were also pressed separately on the agar surface for the purpose of comparison. After incubation at 37 ºC overnight, formation of inhibition zone was checked and diameter of zone was measured.

4.2.3.7.2 Determination of minimum inhibitory concentration (MIC) and minimum bactericidal concentration (MBC)

MHB broth culture (18 h) of clinical isolates of *E.coli* and *P.aeruginosa* isolates were selected for the evaluation of MIC. The assay was performed in 96-well microtitre plates. Inoculum density of the test organisms was adjusted to that of 0.5 Mc Farland standards (10 µL. 1x 108 CFU/mL). Broth was dispensed into the wells of micro-titre plate followed by addition of the Ag-NPs solution and inoculum. Serial dilutions were performed by addition of various quantities of Ag-NPs solution to the microtitre wells with MHB to reach concentrations of 10 µg/mL- 100 µg/mL. The antibiotic imipenem and ciprofloxacin was also serially diluted with broth at a concentration ranging from 8 µg/mL– 128 µg/mL. Microtitre wells containing fresh medium served as a negative control and that containing bacterial growth served as a positive control. Total volume of the assay system in each well was kept at 200 µL. Plates were incubated at 37 ºC for 18 h and read at 600 nm in a plate reader (BIORAD 680). MIC was recorded as the lowest concentration at which growth was observed. The measurements were done in triplicate. The content of the wells showing no visible growth as well as the positive and negative controls were subcultured on nutrient agar plates by streaking and incubated at 37 ºC overnight. On incubation of the plates, the dilution from the minimum concentration from

those streaks showing no growth was considered as MBC. The highest dilution showing at least 99% inhibition is taken as MBC.

4.2.3.8 Toxicity Analysis (Evaluation of cell viability)

Human THP-1 monocyte cells were grown in RPMI 1640 medium, supplemented with 2 mM of L-glutamine, 10 % of heat-inactivated fetal bovine serum, 100 U/mL of penicillin, 100 μg/mL of streptomycin and 0.25 μg/mL of amphotericin B. Cells were grown at 37 °C under 5 % CO_2 atmosphere and split every 3 days. Cells were seeded in 96-well plates with 5×10^3 cells per well. After overnight incubation, plates were centrifuged (300 x g, 20 min) and the medium removed well by well by aspiration. A fresh medium was added and cells were incubated for 24 h with 0, 0.002, 0.02, 0.2, 2, 20 and 200 μg/mL of ENP. Six wells were used per culture condition and experiments were repeated thrice. After 24 h the cell viability was checked using WST-1 assays, performed according to manufacturer's protocols. Absorbance was measured at 450 nm with reference wavelengths of 620 nm.

4.3 Results and Discussions:

4.3.1 Gelatin capped silver nanoparticles

4.3.1.1 Optical characterizations

During the reaction, the colour of the Ag+/gelatin solutions in the reaction flasks changed from colourless to light brown and then dark brown as the reaction time increased, indicating the formation of dextrose reduced gelatin-capped Ag-NPs of different particle sizes. Dextrose reduce silver to metallic silver and become oxidized to gluconic acid.

$Ag^{+}_{(aq)}$ + gelatin $(gel)_{(aq)}$ ⟶ $[Ag\ (gel)^{+}_{(aq)}]$ (1)

$C_6H_{12}O_{6\ (aq)}$ ⟶ $C5\ H_{11}O_5$-CHO (2)

$[Ag\ (gel)^{+}_{(aq)}]$ + $C_5H_{11}O_5$-CHO ⟶ Gelatin capped Ag-NPs + $C_5H_{11}O_5$-COOH (3)

4.3.1.1.1 UV-Visible spectroscopy

The gradual formation and growth of silver nanoparticles at different reaction times were studied using UV- visible spectroscopy. The UV-visible spectra of the as-prepared samples at different reaction times are shown in Figure 4.1. The obtained Ag-NPs displayed absorption maxima peaks characteristic of surface plasmon resonance (SPR) band for silver. The shift in the SPR peak can be related to the formation of silver nanoparticles of different particle sizes. The characteristic absorption maximum peak of the as-synthesised Ag-NPs was gradually blue-shifted from 424 nm to 400 nm with increase in intensity as the reaction time increased. This indicates that as the reaction time increased, the particle size of the silver nanoparticles decreased. The increase in the intensity of the SPR peak as the reaction time increased indicates continued reduction of silver ions and increase in the concentration of the Ag-NPs. The broadness of the SPR peak also decreased with reaction time indicating particles with narrow size distribution.

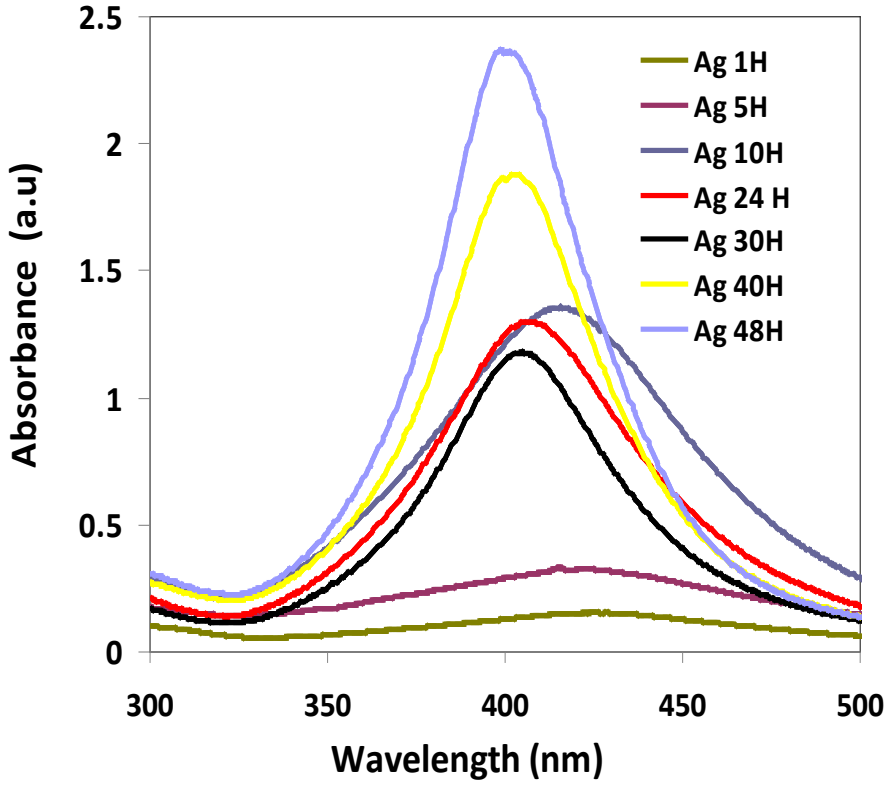

Figure 4.1: Absorption spectra of dextrose reduced gelatin-capped Ag-NPs.

4.3.1.1.2 Fourier transform infrared spectroscopy

The surface chemistry of the as-synthesized dextrose reduced gelatin-capped Ag-NPs was investigated using FT-IR spectroscopy to confirm the capping by gelatin (Fig. 4.2). The peak at 1045 cm^{-1} is attributed to the –C-O vibrations from the gelatin. Two small peaks at 1084 cm^{-1} and 1377 cm^{-1} are attributed to the –C-O stretching and O-H stretching respectively. A small peak at 1465 cm^{-1} is due to the amide linkage vibration, i.e –N-H stretching of the gelatin. A significant peak at 1641 cm^{-1} is due to the –C=O stretching of the -COOH group of the gluconic acid. This confirmed the reducing action of the dextrose. The broad peak at 3342 cm^{-1} is due to the –O-H stretching vibration. The slight shift in the OH and N-H bands of the gelatin-capped Ag-NPs compared to free gelatin

indicated that, there is electrostatic crosslinking between the Ag-NPs and the gelatin, thus confirming the capping of the Ag-NPs by gelatin. Such interaction also enhances the interaction between gelatin molecules and ameliorates the stability of the as-synthesized gelatin capped Ag-NPs (Oluwafemi et al., 2013).

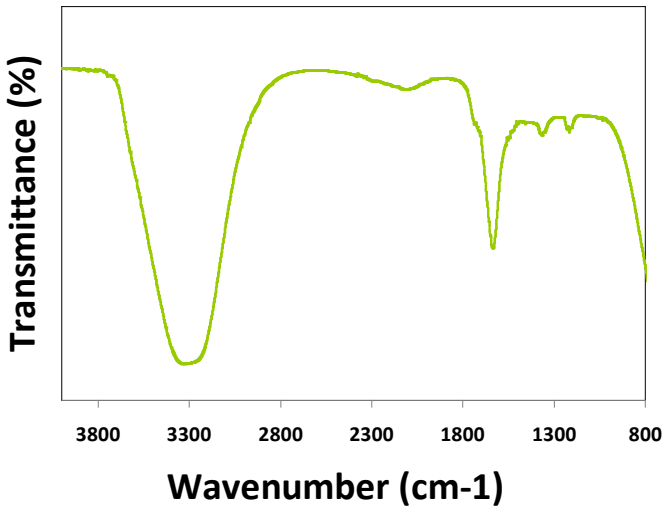

Figure 4.2: FTIR spectrum of dextrose reduced gelatin capped Ag-NPs at 48 h.

4.3.1.2 Morphological characterizations

4.3.1.2.1 X- ray diffraction analysis

The typical XRD pattern of the as-synthesised Ag-NPs is shown in Figure 4.3. Five diffraction peaks at 2Θ value of 19.8º, 38.9º, 45º, 64.º and, 76.0º were observed. The broad peak between 15-20º is due to the amorphous gelatin phase used as the capping agent. The four peaks at 38.9º, 45º, 64.1º and, 76.0º are attributed to the (111), (200), (200) and (311) crystalline planes of the face centered cubic (*fcc*) crystalline structure of metallic silver, respectively (JCPDS file No. 00-004-0783). The broad nature of the XRD peaks could be attributed to the nanocrystalline nature of the Ag-NPs.

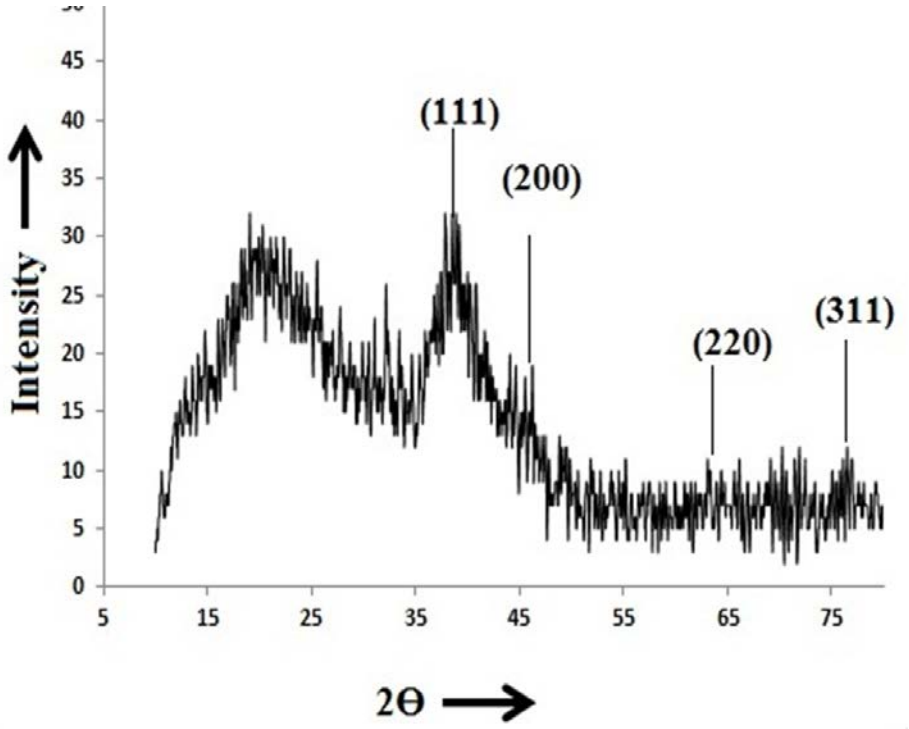

Figure 4.3: Typical XRD pattern of dextrose reduced gelatin -capped Ag-NPs at 48 h.

4.3.1.2.2 High resolution transmission electron microscopic analysis

The typical TEM morphologies of the as-prepared Ag-NPs at different reaction times of 1h, 24 h and 48 h are shown in Figure 4.4 A-C. The TEM results indicate that the particles are well dispersed and spherical in shape. The average particle diameter, as determined from the TEM images are 18.01 ± 5.54 nm (1 h), 9.98 ± 4.61 nm (24 h) and 9.68 ± 1.44 (48 h). The decrease in the average particle diameter and size distribution (σ), as the reaction time increases, is in agreement with the absorption spectra. The results also indicate that samples obtained over a long period of time retained a narrower particle size distribution with high level of uniformity. Similar observation has been reported by

Darroudi et al., 2011. The HRTEM images (Figure. 4.5A) gives further insight into the microstructure (shape) and crystallinity of the as-prepared Ag-NPs. The HRTEM image shows that the as-synthesized materials are spherical and consist of well ordered single crystals with distinct lattice fringes confirming the crystalline nature of the silver nanoparticles. The micrograph shows the presence of well separated individual lattice fringes with the measured lattice spacing (d) of 0.227 nm corresponding to the d(1 1 1) spacing for face-centered cubic *(f c c)* silver. The selected area electron diffraction (SAED) pattern in Figure 4.5B further confirmed the crystalline nature of the particles and indicate that they are single crystals with *fcc* structure.

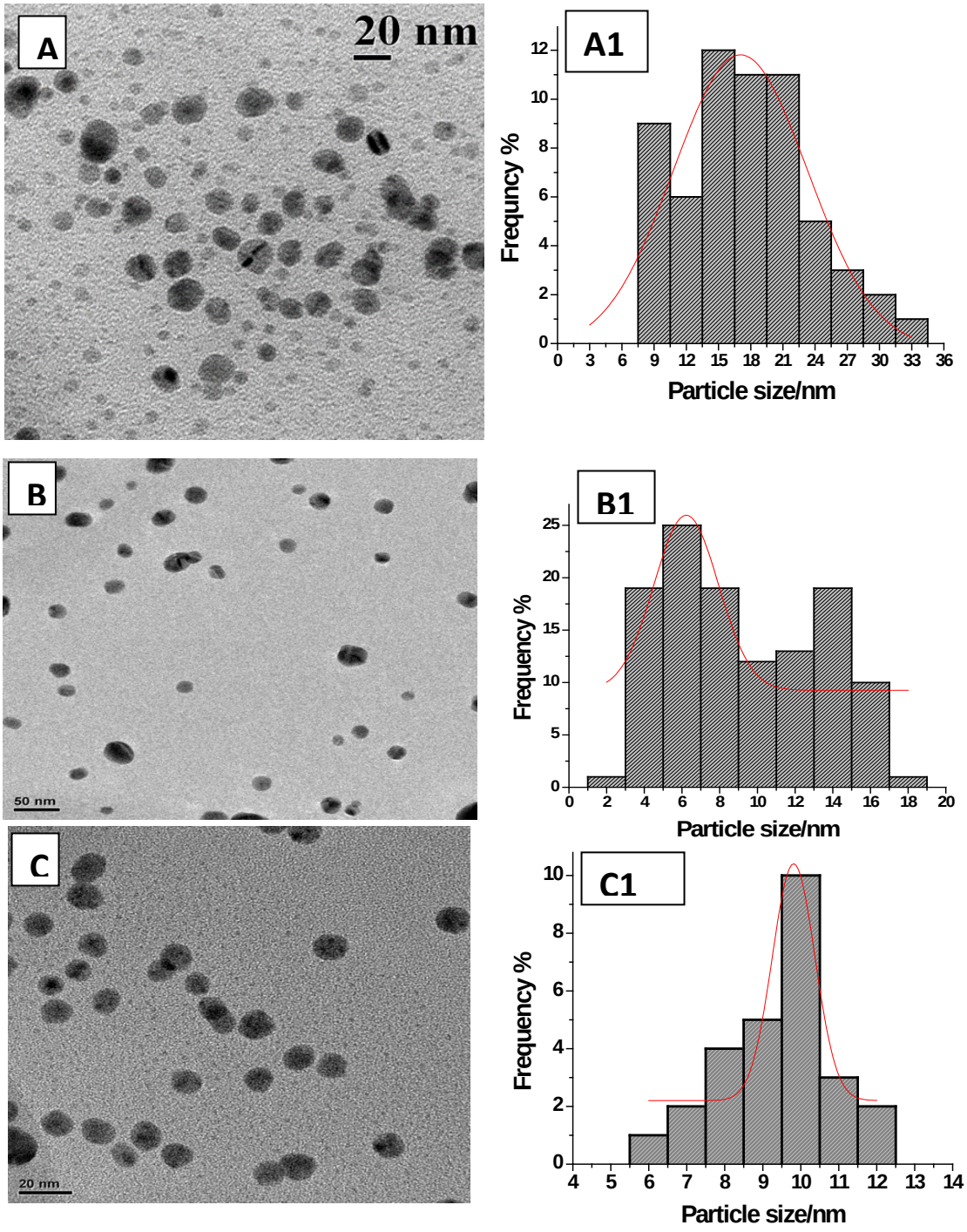

Figure 4.4: TEM Images and the corresponding size distribution curves of dextrose reduced gelatin capped- Ag-NPs at 1 h (A), 24 h (B) and 48 h (C).

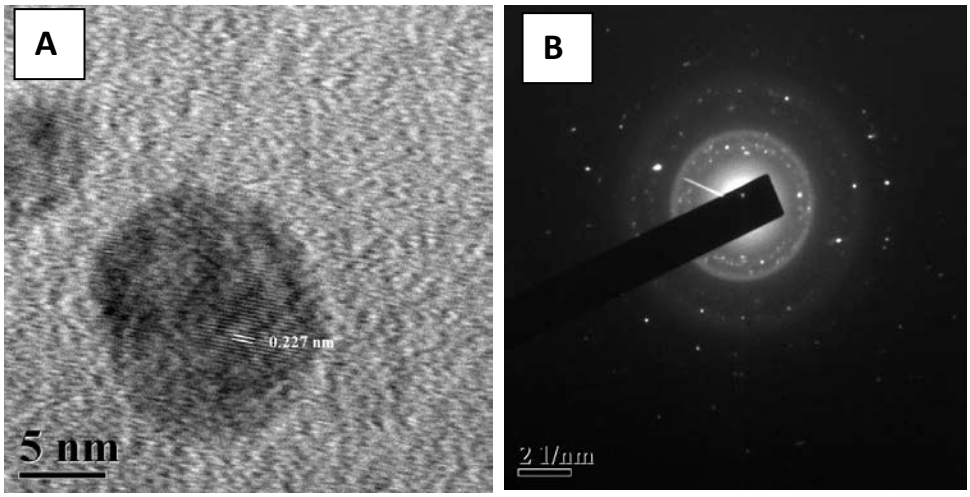

Figure 4.5: Typical HRTEM image (A) and SAED (B) of dextrose reduced gelatin capped Ag-NPs.

4.3.1.2.3 Electron diffraction spectroscopy analysis (EDS)

The EDS spectrum given in Fig. 4.6 clearly confirmed the formation of silver nanoparticles without any impurity. The presence of copper comes from the copper grid used for the EDS sample preparation.

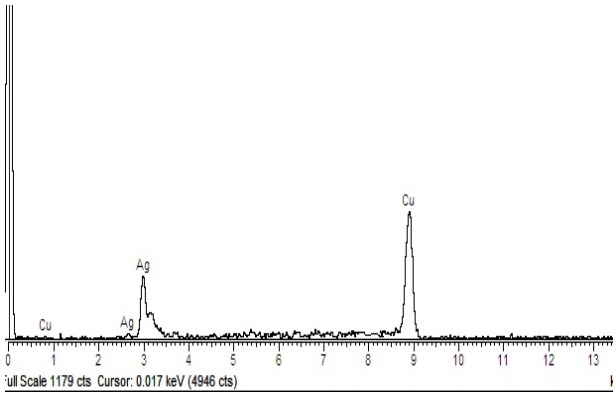

Figure 4.6: EDS spectrum of dextrose reduced gelatin -capped Ag-NPs.

4.3.1.3. Antibacterial study

Inhibition zone values were obtained for the as- synthesized Ag-NPs tested against two Gram negative bacteria (*E.coli* and *P. aeruginosa*). Fresh silver nitrate solution was used as control. On incubation, the plates in which disc diffusion was carried out were checked for the presence of inhibition zone around the antibiotic discs and those discs loaded with nanoparticles. Figure 4.7 illustrate the images of each inhibition zones. The diameter of each inhibition zones measured and the results of the finding are shown in Table 4.1. The results show that, there was zone of growth inhibition around all the discs tested against the E. coli except for the ciprofloxacin disc. In case of *P. aeruginosa*, there was zone of inhibition around all the discs except the two antibiotic discs.

The preliminary disc diffusion method indicated that all the as-synthesized Ag-NPs showed antibacterial activity against the two bacteria under study. At the same time both bacteria were shown to be resistant to the present drug of choice ciprofloxacin. *E coli* were found to be sensitive to imipenem, whereas *P.aeruginosa* was resistant to the antibiotic highlighting its drug resistant nature. The MIC of the samples were evaluated using the microtube broth dilution technique and the results of the finding are shown in Table 4.2.

The MIC of the silver nanoparticles at different reaction times was found to be between 10 - 12.5 µg/mL against *E.coli* and between 6-18.37 µg/mL against *P.aeruginosa*. The MBC were between 12.5-18.37 for both E.coli and P. aeruginosa respectively. The MIC of the antibiotics was also evaluated and was found to be 16 µg/mL for both *E.coli* and *P.aeruginosa* in case of imipenem. For the ciprofloxacin, the MIC was found to be 10 and 20 µg/mL respectively for *E.coli* and *P.aeruginosa*. The as-synthesized Ag-NPs at

different reaction times show better efficacy against the two bacteria than imipenem and silver nitrate, and a better efficacy against *P.aeruginosa* than ciprofloxacin. However, the antibiotic, ciprofloxacin showed a stronger antibacterial activity against *E.coli* than most of the as-synthesized Ag-NPs. Contrary to the reports that, the smaller the Ag-NPs the higher the antimicrobial activity, the results of this analysis showed that, the smaller Ag-NPs produced at higher reaction time showed lower antibacterial activity. This anomaly has been attributed to the effective passivation of the smaller Ag-NPs surface by the gelatin, thus reducing its antimicrobial activity as well as its toxicity. However, the antimicrobial activity is still stronger than silver nitrate except for Ag-NPs produced at 30 h reaction time. Furthermore, the as-synthesised Ag-NPs also have bactericidal effects resulting not only in inhibition of bacterial growth but also in killing bacteria. This irreversible inhibition of bacterial growth has been reported to be desirable to prevent bacterial colonization of silver-containing medical devices, such as catheters (Rupp et al., 2004; Samuel & Guggenbichler, 2004) where bacteria-killing activity is required. The MBC of the as-synthesised Ag-NPs against Gram-negative bacteria were the same as MIC for some of the samples (Table 4.2) and were higher than the value obtained for silver nitrate except for 30 h sample. These results clearly show that the as-synthesised dextrose reduced, gelatin capped-Ag-NPs can inhibit the growth and multiplication of the tested bacteria.

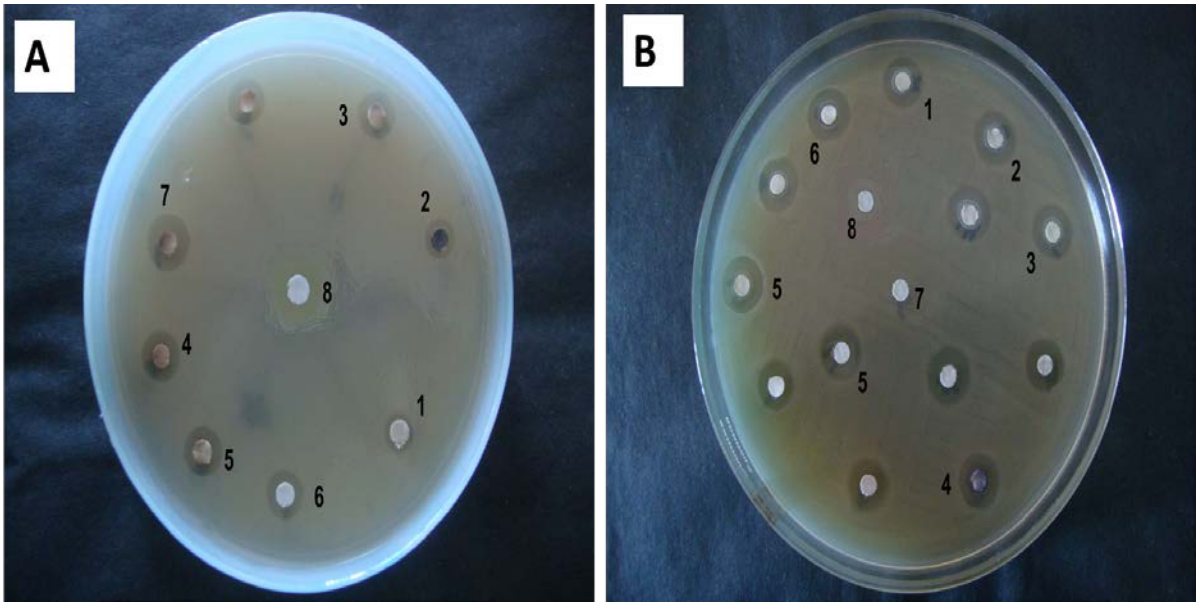

Figure 4.7: Comparison of the inhibition zone test for Gram-negative bacteria (a) *E.coli* and (b) *P.aeruginosa*

Table 4.1: Average diameter of inhibition zone for dextrose reduced gelatin capped Ag-NPs against *E.coli* and *P aeruginosa.*

Sl No	Sample	Diameter of zone of inhibition (mm)	
		E. coli	P. aeruginosa
1	1 hour	8	12.5
2	5 hour	11	13
3	18 hour	12	13
4	24 hour	13	12
5	30 hour	12	14
6	$AgNO_3$	11	13
7	Imipenem (10mg)	15	Not Appearing
8	Ciprofloxacin (5 mg)	Not Appearing	Not Appearing

Table 4.2: MIC and MBC values of the dextrose reduced gelatin capped Ag-NPs against *E.coli* and *P.aeruginosa*

Sl No	Sample Code	E coli ATCC	E coli ATCC	*P.aeruginosa*	*P.aeruginosa*
		MIC (µg/ml)	MBC (µg/ml)	MIC (µg/ml)	MBC (µg/ml)
1	1 hour	10	12.5	6	12.5
2	5 hour	12.5	12.5	6	12.5
3	18 hour	12.5	12.5	12.5	12.5
4	24 hour	12.5	12.5	12.5	12.5
5	30 hour	12.5	18.37	18.37	18.37
6	$AgNO_3$(fresh)	18.37	18.37	18.37	18.37
7	Imipenem	16	-	16	-
8	Ciprofloxacin	10	-	20	-

4.3.1.4 Toxicity study

The cell viability study for the gelatin capped-Ag-NPs at different concentration is given in Figure 4.8. Compared to the control, the as-synthesised Ag-NPs are less toxic at lower concentrations (less than 10 µg/ml). The presence of gelatin layer over the nanoparticles protect its environment and reduces the release of silver ions thereby reducing the toxicity. It has been reported that the interaction of metal ions with cells can cause a phenomena bacterial aggregation, inhibiting microbial colonization and invasion (Ryan et al., 2006). The metal ions get attached to the negative cell wall and further depleting it which causes the bacteria to aggregate. Silver in its nano size possess large surface area for the microbe to be exposed to. Though silver nanoparticles find use in many antibacterial applications, the action of this metal on microbes is not fully known. It has

been hypothesized that silver nanoparticles can cause cell lysis or inhibit cell transduction.

Silver nanoparticles have the ability to penetrate into the bacterial cell wall thereby forming ‘pits’ which cause structural changes in the cell membrane and accumulation of the nanoparticles on the cell surface (Sondi & Salopek, 2004). The formation of free radicals by the silver nanoparticles when in contact with the bacteria have the ability to damage the cell membrane and make it porous which can ultimately lead to cell death (Danilcauk et al., 2006; Kim et al., 2007). It has also been proposed that there can be release of silver ions by the nanoparticles, and these ions can interact with the thiol groups of many vital enzymes and inactivate them (Matsumura et al., 2003). The bacterial cells in contact with silver take in silver ions, which inhibit several functions in the cell and damage the cells.

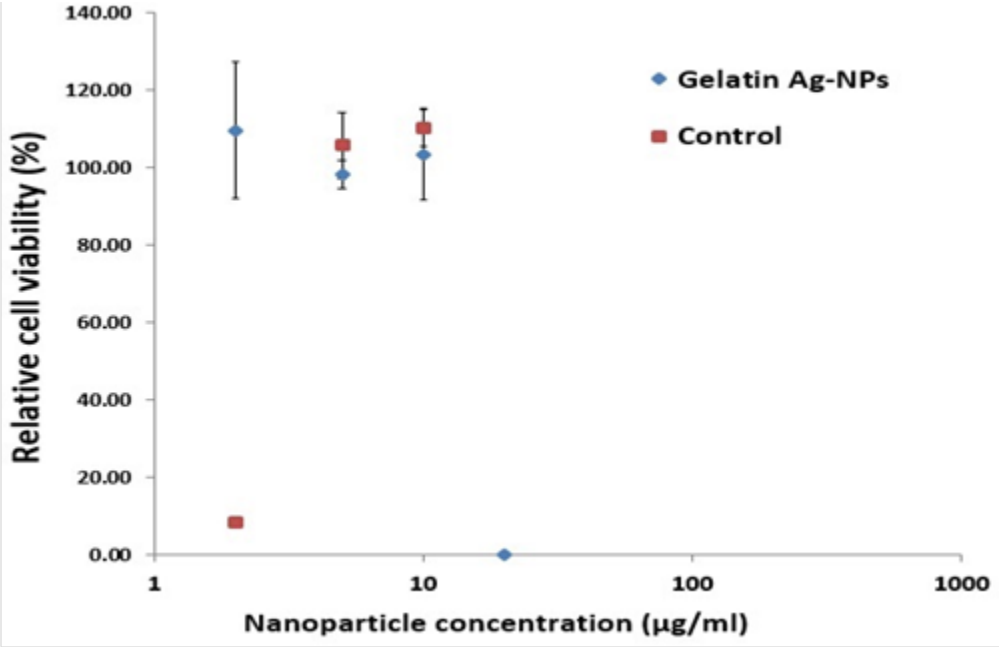

Figure 4.8: Relative cell viability of the dextrose reduced gelatin capped Ag-NPs against human HTP-1 cell line.

Summary: Green synthesis of highly monodispersed, water soluble, stable and smaller sized dextrose reduced gelatin -capped-silver nanoparticles (Ag-NPs) via an eco-friendly, completely green method is discussed. By varying the reaction time, the temporal evolution of the growth, optical and antimicrobial properties of the as-synthesised Ag-NPs were investigated. The nanoparticles were characterized using UV-vis absorption spectroscopy, Fourier transform infra-red spectroscopy (FTIR), X-ray diffraction (XRD), transmission electron microscopy (TEM) and high resolution transmission electron microscopy (HR-TEM). The absorption maxima of the as-synthesized materials at different reaction time showed characteristic silver surface plasmon resonance (SPR) peak. The antimicrobial properties of the gelatin capped Ag-NPs at different reaction times where tested against *Escherichia coli* and *Pseudomonas aeruginosa.*

4.3.2 Dextrose reduced Starch -capped silver nanoparticles

4.3.2.1. Optical characterizations

During the reaction, the colour of the Ag+/starch solutions of the reaction changes from colourless to light brown and then dark brown as the reaction time increases. This indicates the formation of dextrose reduced starch-capped Ag-NPs of different particle sizes due to the reduction of silver cations to metallic silver by dextrose. The gradual formation and growth of silver nanoparticles at different reaction times were studied using UV- visible spectroscopy.

4.3.2.1.1 UV-Visible spectroscopy

The UV-Visible spectra of the as-prepared samples at different reaction times are shown in Figure 4.9. The obtained Ag-NPs displayed absorption maxima peaks characteristic of surface plasmon resonance (SPR) band for silver. The shift in the SPR peak can be related to the formation of silver nanoparticles of different particle sizes. The characteristic absorption maximum peak of the as-synthesised Ag-NPs was gradually blue-shifted from 421 nm to 412 nm with increase in intensity as the reaction time increased. This indicates that as the reaction time increased, the particle size of the silver nanoparticles decreased. The increase in the intensity of the SPR peak as the reaction time increased indicates continued reduction of silver ions and increase in the concentration of the Ag-NPs. The broadness of the SPR peak also decreased with reaction time indicating particles with narrow size distribution.

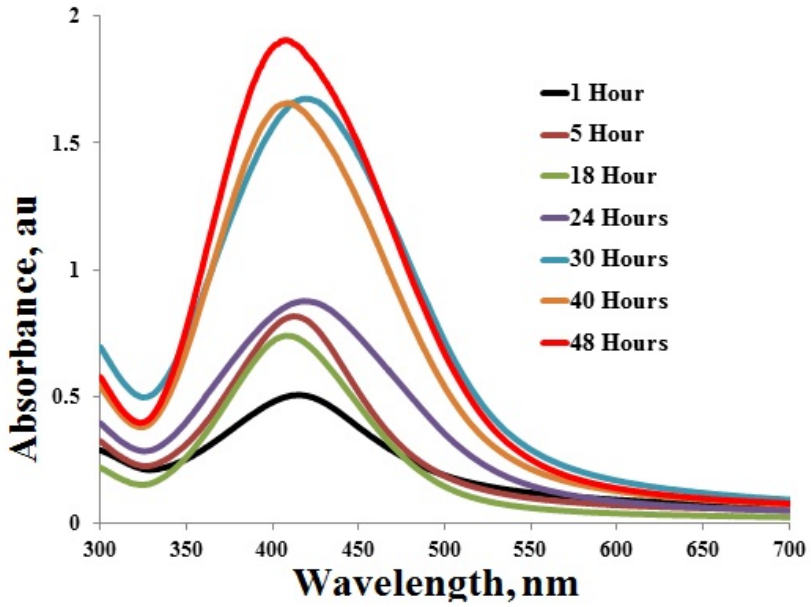

Figure 4.9: Absorption spectra of dextrose reduced starch-capped Ag-NPs at different reaction time.

4.3.2.1.2 Raman spectroscopy Analysis

Figure 4.10 gives the selective enhancement of Raman bands of the organic capping agents bound to the nanoparticles. The spectrum shows a strong and sharp band at 220 cm^{-1}, which can be attributed to the stretching vibrations of Ag–O bonds or to the ionic species sorbed onto the metal surface (Ghaseminezhad et al.,2012). The peak indicates the formation of a chemical bond between silver and hydroxyl groups of starch molecules. The broad peak at 1351 and 1523 cm^{-1} correspond to symmetric and asymmetric C=O stretching vibrations of carboxylate group, respectively (Mohan et al., 2014). The broad band at 1040 cm^{-1} and a sharp peak at 1123 cm^{-1} comes from the C–H in plane bending while the peak at 827 cm^{-1} is assigned to C-H out of plane wag from the saccharide structure of starch. Thus, from the preferential enhancement of these bands; it

can be concluded that hydroxyl groups of the starch are involved in the capping of the silver nanoparticles. The schematic diagram for the reaction is shown in Fig. 4.11.

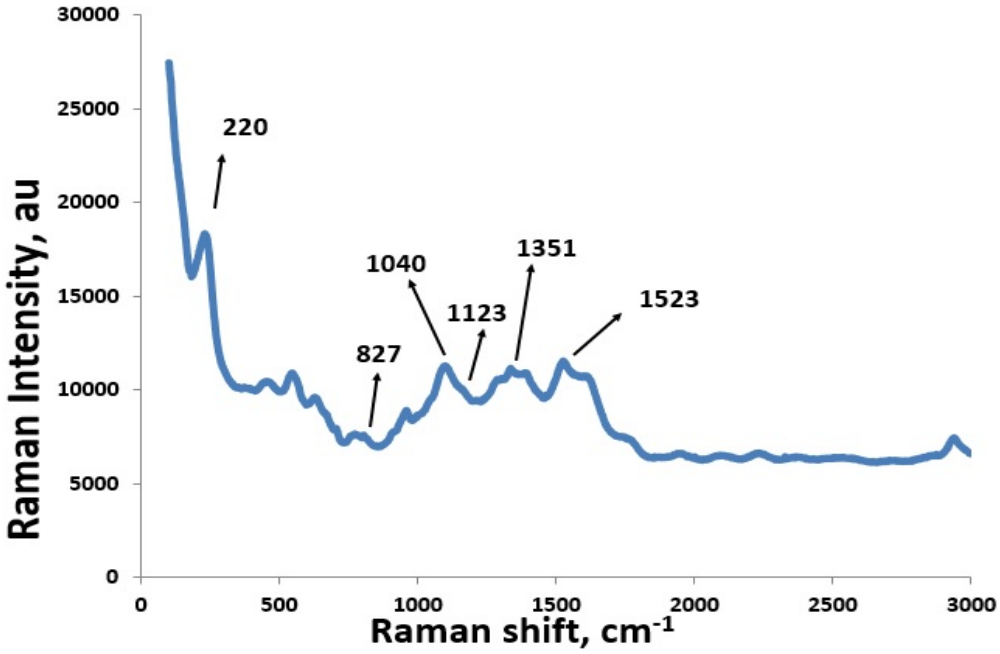

Figure 4.10: Raman spectrum of dextrose reduced starch- capped Ag-NPs.

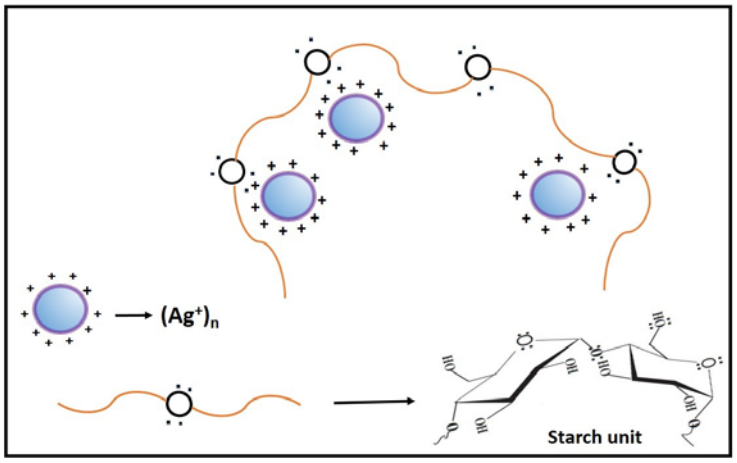

Figure 4.11: Schematic representation for the formation of starch -capped silver nanoparticles.

4.3.2.1.3 Fourier transforms infrared spectroscopy

The surface chemistry of the as-synthesized dextrose reduced starch capped - Ag-NPs was investigated using FT-IR spectroscopy (Fig. 4.12). A weak peak at around 990 cm^{-1} is due to the glycosidic linkage. Two small peaks at 1208 cm^{-1} and 1402 cm^{-1} are attributed to the –C-O stretching and O-H stretching from the starch. The broad peak at 3342 cm^{-1} is due to the –O-H stretching vibration.

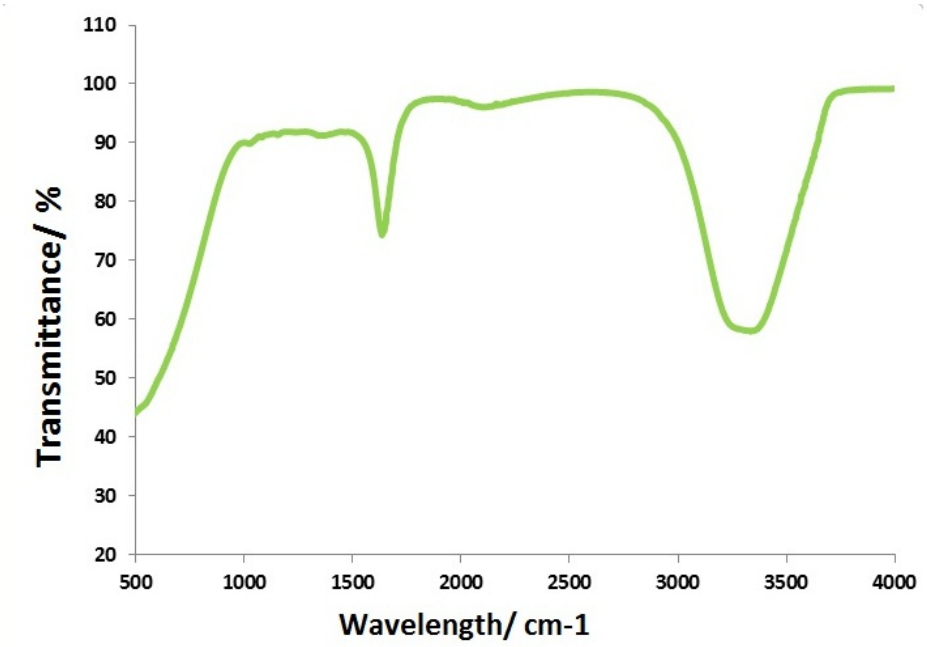

Figure 4.12: FTIR spectrum of dextrose reduced starch capped Ag-NPs at 48 h

4.3.2.2 Morphological characterizations

4.3.2.2.1 X- ray diffraction analysis

The typical XRD pattern of the as-synthesised Ag-NPs is shown in Figure 4.13. Five diffraction peaks at 2Ɵ values of 21.1º, 37.6º, 43.8º, 63.85º and 77.15º were observed.

The broad peak between 15-20 degree is due to the amorphous starch phase used as the capping agent. The four peaks at 37.6º, 43.8º, 63.85º and 77.15º are attributed to the (111), (200), (220) and (311) crystalline planes of the face centered cubic (fcc) crystalline structure of metallic silver, respectively (JCPDS file No. 00-004-0783). The broad nature of the XRD peaks could be attributed to the nanocrystalline nature of the Ag-NPs.

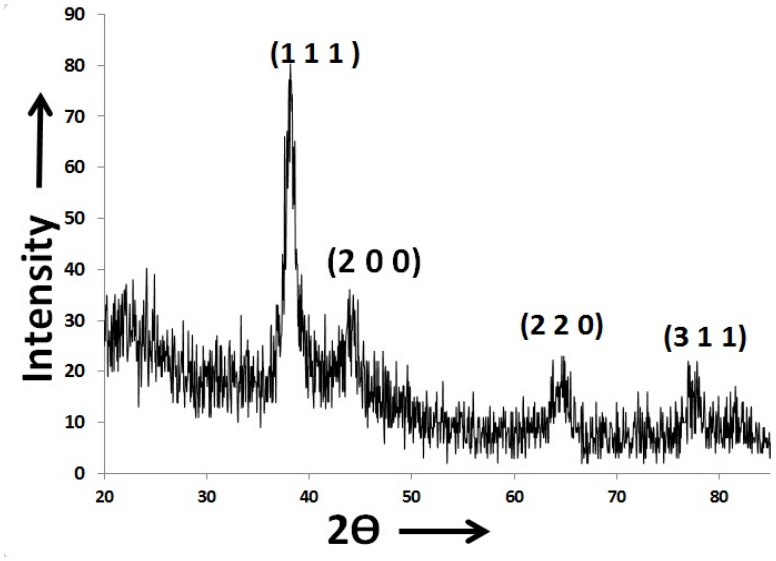

Figure 4.13: Typical XRD pattern of dextrose reduced starch capped Ag-NPs at 48 h

4.3.2.2.2 High resolution transmission electron microscopic analysis

The typical TEM morphologies of the as-prepared Ag-NPs at different reaction times of 1 h, 24 h and 48 h are shown in Figure 4.14 (A-C). The TEM results indicate that the particles are well dispersed and spherical in shape. The average particle diameter, as determined from the TEM images are 19.41 ± 3.44 nm (1 h), 8.13 ± 1.9 nm (24 h) and 6.27 ± 1.63 (48 h). The decrease in the average particle diameter and size distribution (σ), as the reaction time increases, is in agreement with the absorption spectra. The results also indicate that samples obtained over a long period of time retained a narrower particle size distribution with high level of uniformity. The HRTEM images (Figure 4.15A) give

further insight into the microstructure (shape) and crystallinity of the as-prepared Ag-NPs. The HRTEM image shows that the as-synthesised materials are spherical and consist of well-ordered single crystals with distinct lattice fringes confirming the crystalline nature of the as-synthesised silver nanoparticles. The micrograph shows the presence of well separated individual lattice fringes with the measured lattice spacing (d) of 0.210 nm corresponding to the d (1 1 1) spacing for face-centered cubic (*f c c*) silver. The selected area electron diffraction (SAED) pattern in Fig. 4.15 B further confirmed the crystalline nature of the particles and indicate that they are single crystals with *fcc* structure.

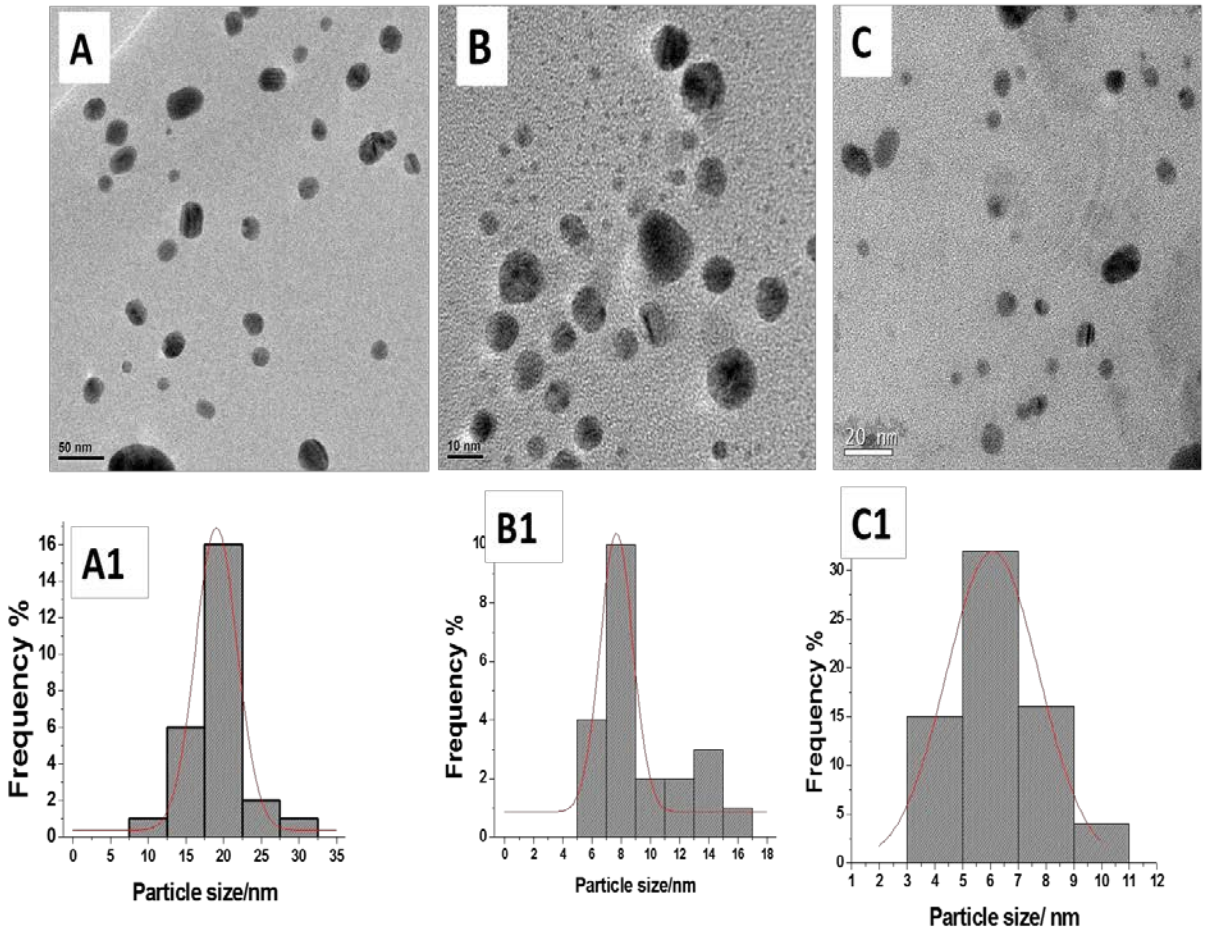

Figure 4.14: TEM Images at 1 h (A), 24 h (B), 48 h (C) and corresponding distribution curves (A1, B1 and C1) for dextrose reduced starch -capped Ag-NPs.

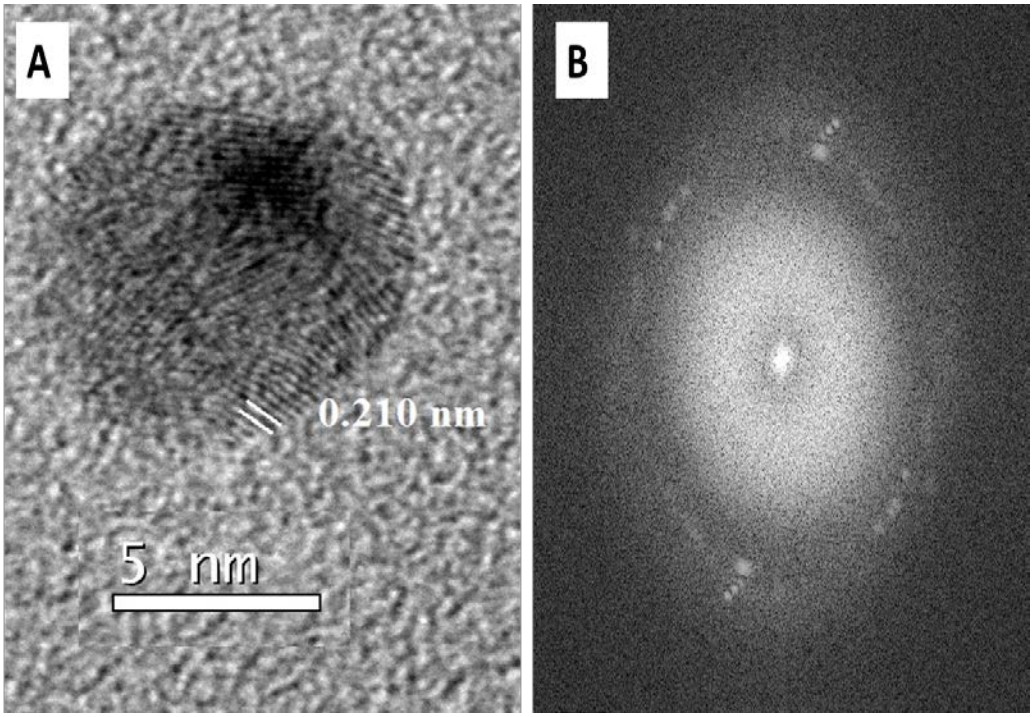

Figure 4.15: Typical HRTEM image (A) and SAED (B) of dextrose reduced starch - capped Ag-NPs.

4.3.2.2.3 Electron diffraction spectroscopy analysis (EDS)

The EDS spectrum shown in Fig. 4.16 clearly confirmed the formation of silver nanoparticles without any impurity. The presence of copper comes from the copper grid used for the EDS sample preparation.

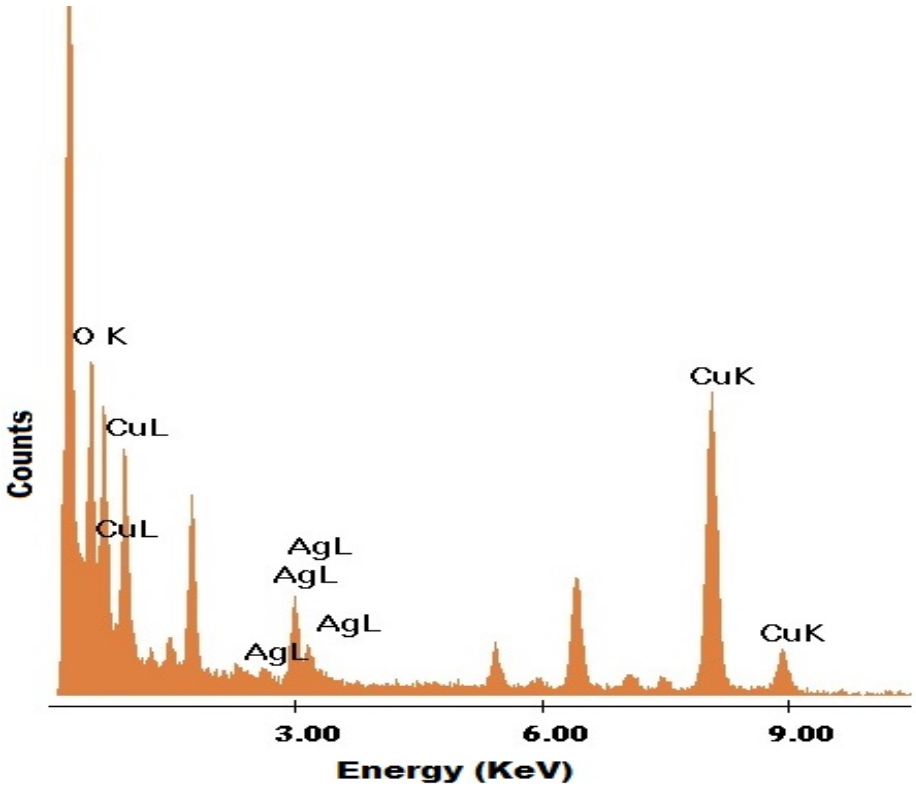

Figure 4.16: EDS spectrum of dextrose reduced starch-capped Ag-NPs.

4.3.2.3 Antibacterial study

After 18 hours of incubation, the plates in which disc diffusion was carried out were checked for the growth of inhibition zone around the antibiotic discs and those discs loaded with nanoparticles. Figure 4.17 illustrate the images of each inhibition zones. The diameter of each inhibition zones was measured and the results of the finding are shown in Table 4.3.

The results showed that, there was zone of growth inhibition around all the discs tested against the *E. coli*. and the two strains of *P. aeruginosa*. The preliminary disc diffusion

method showed that all the as-synthesized Ag-NPs had antibacterial activity against the three bacteria under study.

The MIC of the samples was evaluated using the microtube broth dilution technique and the results of the finding are shown in Table 4.4. The MIC of the silver nanoparticles at different reaction times was found to be between 48-98 µg/mL against E. coli and P. aeruginosa. The MBC for both E. coli and P. aeruginosa were 98 µg/ml. The antibiotic gentamycin, showed a stronger antibacterial activity against E. coli than most of the as-synthesised Ag-NPs. The results of the antibacterial results were in agreement with the reported results i.e the smaller the Ag-NPs the higher the antimicrobial activity. The 48 h sample which has the smallest size showed the highest inhibition zone and MIC values. As compared to the previous reported work on gelatin coated silver nanoparticles (Mohan et al., 2014), this anomaly has been attributed to the less effective passivation of the smaller Ag-NPs surface by the starch, thus increasing its antimicrobial activity (Oluwafemi et al., 2013). The antimicrobial activity of all the samples were stronger than silver nitrate. Furthermore, the as-synthesised Ag-NPs also have bactericidal effects resulting not only in inhibition of bacterial growth but also in killing bacteria. The MIC and MBC results clearly show that the starch-capped Ag-NPs can effectively inhibit the growth and multiplication of the tested bacteria

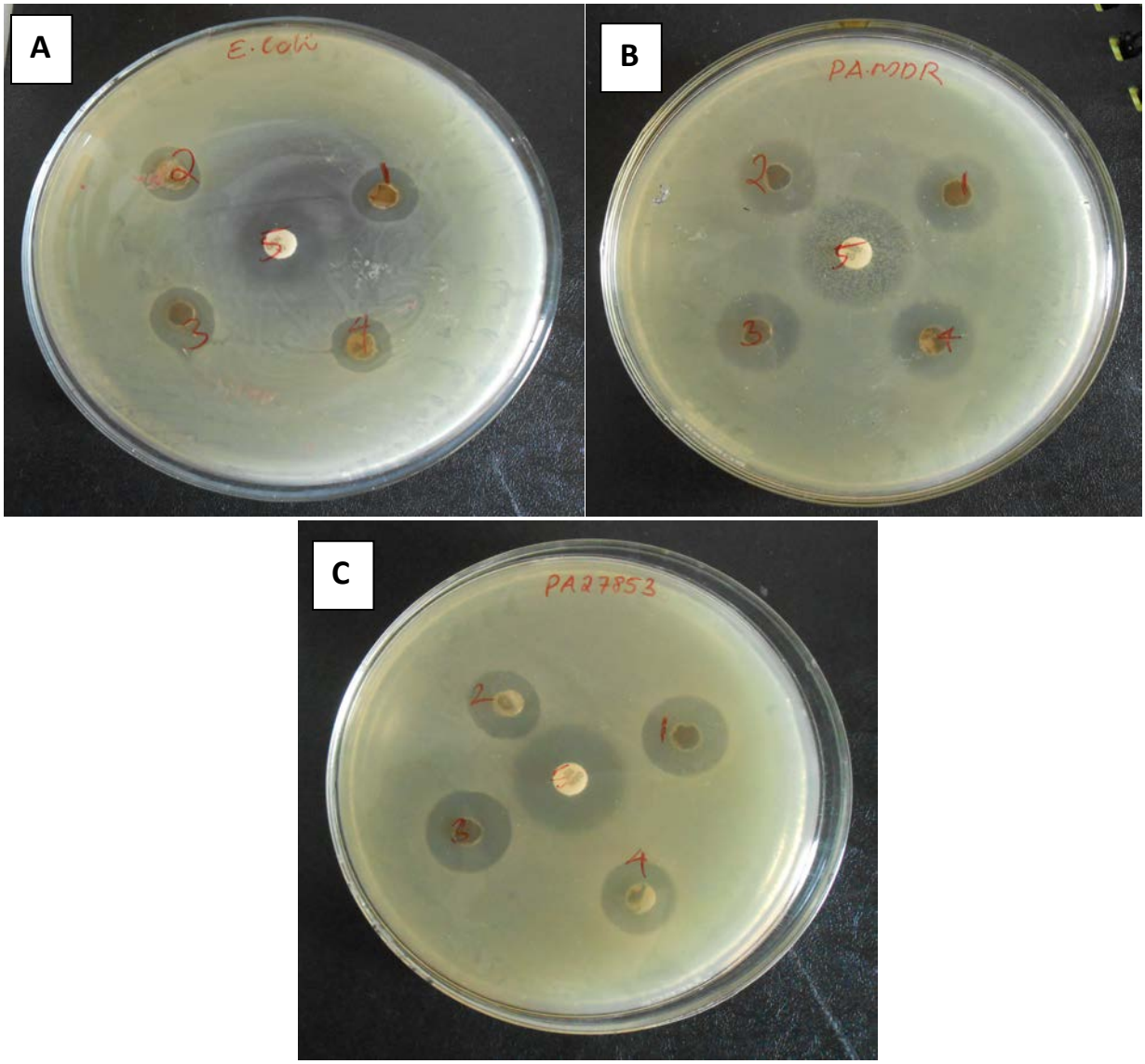

Figure 4.17: Comparison of the inhibition zone test for the dextrose reduced starch – capped Ag-NPs against Gram-negative bacteria (a) *E. coli* and (b) *P. aeruginosa* (PA27853) (c) *P. aeruginosa* (PAMDR)

Table 4.3: Average diameter of inhibition zone for dextrose reduced starch - capped Ag-NPs against *E. coli* and *P. aeruginosa*.

Sl No	sample	Diameter of zone of inhibition (mm)		
		E. coli (ATCC 25922)	*P. aeruginosa (PA 27853)*	*P. aeruginosa (PA MDR)*
1	1 hour	12	16	16
2	24 hour	11	15	16
3	48 hour	14	17	16
4	Silver nitrate	11	13	14
5	Gentamycine	16	20	22

Table 4.4: MIC and MBC values of dextrose reduced starch –capped Ag-NPs against *E. coli* and *P. aeruginosa*

S.No	Sample code	*E. coli* ATCC		*P. Aeruginosa (PA 27853)*	
		MIC (µg/ml)	MBC (µg/ml)	MIC (µg/ml)	MBC (µg/ml)
1	1 h	10.7± 0	21.4± 0	21.4± 0	21.4± 0
2	24 h	21.4± 0	21.4± 0	21.4± 0	21.4± 0
3	48 h	21.4± 0	21.4± 0	10.7± 0	21.4± 0
4	$AgNO_3$ fresh	42.8± 0	42.8± 0	42.8± 0	42.8± 0

4.3.2.4 Toxicity study

The preliminary screening of cell viability study result for the starch capped Ag-NPs at different concentration is given in Fig. 4.18. The results clearly shows that the as-synthesised Ag-NPs are less toxic than its control i.e. silver nitrate at lower concentrations (less than 10 µg/ml). This has been attributed to the presence of starch capping, which serve as a protective layer and reduce the release of deleterious silver ions. It has already been reported that the surface modified nanoparticles had good biocompatibility when compared to those of pristine nanoparticles (Kumar et al., 2014). Therefore, capping with polymer is protective for the mitochondrial activity thereby improving the viability of cells exposed to nanoparticles.

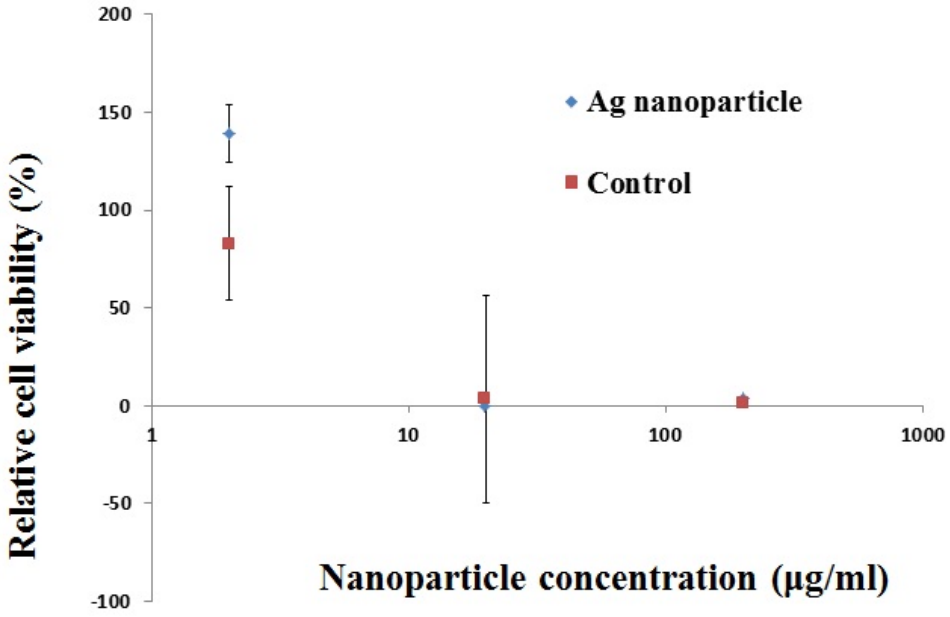

Figure 4.18: Relative cell viability of the dextrose reduced starch-capped Ag-NPs against human HTP-1 cell line.

Summary: The synthesis of water soluble, stable and smaller sized starch capped-silver nanoparticles (Ag- NPs) via a completely green method by using dextrose as reducing agent without any accelerating agent is discussed. The optical and structural characterizations of the as- prepared Ag-NPs were carried out using UV visible spectroscopy, Raman spectroscopy, XRD and TEM. The antibacterial property of the as-synthesised dextrose reduced, starch-capped Ag-NPs at different stages of growth were tested for the first time against *Escherichia coli* and two strains of *Pseudomonas aeruginosa*, which are multidrug resistant bacteria and were compared with antibacterial drug gentamycin using disc diffusion method. In addition, the minimum inhibitory concentration (MIC) and minimum bactericidal concentration (MBC) of the as-synthesised Ag-NPs were also evaluated.

4.4 Conclusions

Metal nanoparticles possess unique features and extensive application in various fields. For the synthesis of these metal nanoparticles, developing cost effective methods for large scale synthesis and easy processing with less impact on environment is a major challenge. In this context, we have synthesized small, stable, monodispersed silver nanoparticles capped with biopolymers through a completely green synthetic protocol. Gelatin and starch were used as the capping agent while dextrose and water were used as reducing agent and solvent respectively. The as-synthesized Ag-NPs were small, spherical, nearly monodispersed and highly crystalline with face centered cubic crystal structure. FTIR confirmed the presence of functional groups in gelatin and starch capped silver nanoparticles. The as -synthesized Ag-NPs shows high antibacterial activity against gram negative bacteria such as *E.coli* and *P. aregunosa* and can inhibit the growth and

multiplication of the tested bacteria. In addition, the antibacterial study of starch capped Ag-NPs also indicates that, the time of reaction does not have a significant effect on the on the inhibitory and bactericidal activities. Compared to starch-capped Ag-NPs, gelatin-capped Ag-NPs showed lower MBC concentration which shows that gelatin capped Ag-NPs are having better interaction with cells hence higher bactericidal property than its counterpart. The cell viability test against human HTP-1 cell line indicates that as-synthesised Ag-NPs are less toxic than $AgNO_3$. The biopolymer capping around the nanoparticles may result in the slower release of silver ions from the Ag-NPs which results in comparatively less toxicity of these materials.

References

Batabyal, S.K., Basu, C., Das, A.R., Sanyal, G.S. 2007. Green Chemical Synthesis of Silver Nanowires and Microfibers Using Starch. *J Biobased Mater Bio*., 1:143-147.

Beecroft, L.L. & Ober, C.K. 1997. Nanocomposite Materials for Optical Applications. *Chem. Mater*., 9: 1302-1317.

Bozanic, D.K., Trandafilovic, L.V., Luyt, A.S. & Djokovic, V. 2010. 'Green'synthesis and optical properties of silver–chitosan complexes and nanocomposites. *React. Funct. Polym*., 70: 869-873.

Creighton, J.A., Blatchford, C.G. & Albrecht, M.G. 1979. Plasma resonance enhancement of Raman scattering by pyridine adsorbed on silver or gold sol particles of size comparable to the excitation wavelength. *J. Chem.Soc., Faraday Trans*. 2, 75: 790-798.

Danilcauk, M., Lund, A., Saldo, J., Yamada, H. & Michalik, J. 2006. Conduction electron spin resonance of small silver particles. *Spectrochim. Acta Part A*, 63: 189–191.

Darroudi, M., Ahmad, M.B., Abdullah, A.H., Ibrahim, N.A. 2011. Green synthesis and characterization of gelatin-based and sugar-reduced silver nanoparticles. *Int. J. Nanomedicine*, 6: 569.

Darroudi, M., Ahmad, M.B., Zamiri, R., Zak, A., Abdullah, A.H., Ibrahim, N.A. 2011. Time-dependent effect in green synthesis of silver nanoparticles. *Int. J. Nanomedicine*, 6:677-681.

Eid, K.A. & Assay, H.M. 2012. Controlled synthesis and characterization of hollow flower-like silver nanostructures. *Int. J. Nanomedicine*, 7: 1543-1550.

Filippo, E., Serra, A., Buccolieri, A. & Manno, D. 2010. Green synthesis of silver nanoparticles with sucrose and maltose: Morphological and structural characterization. .*J Non-Cryst. Solids*, 356: 344-350.

Ghaseminezhad, S.M., Hamedi, S. & Shojaosadati, S.A. 2012. Green synthesis of silver nanoparticles by a novel method: Comparative study of their properties. *Carbohydr. Polym.*, 89: 467–.472.

Godovsky, D.Y. 1995. *Adv. Polym. Sci.*, 119: 79-85.

Haes, A.J., Hall, W.P. & Van Duyne, R.P. 2005. Detection of a biomarker for Alzheimer's disease from synthetic and clinical samples using a nanoscale optical biosensor. *Laser Focus World*, 41:105-109.

Hermanson, K.D., Lumsdon, S.O., Williams, J. P., Kaler, E. W. & Velev, O. D. 2001. Dielectrophoretic assembly of electrically functional microwires from nanoparticle suspensions. *Science*, 294: 1082-1086.

Jennifer, A.D., Bettye, L.S.M., & James, E.H. 2007. Toward Greener Nanosynthesis. *Chem Rev.*, 107: 2228-2269.

Kim, J.S., Eunye, K., Kim, J. H., Park, S. J. & Park, Y.H. 2007. Antimicrobial effects of silver nanoparticles. *Nanomed.: Nanotechnol., Biol. Med.*, 3: 95-101.

Kumar, S.R., Marianna, L.F., Gianni,S., Nathanael,A.J., Hong,S.I., Oh, T.H., Mangalaraj, D., Viswanathan,C. & Ponpandian,N. 2014. Hydrophilic polymer coated monodispersed Fe_3O_4 nanostructures and their toxicity. *Mater. Res. Exp.*, 1: 015015-1-15.

Lee, P.C. & Meisel, D.1982. Adsorption and surface-enhanced Raman of dyes on silver and gold sols. *J. Phys. Chem*., 86: 3391-3395.

Magdassi, S., Bassa, A., Vinetsky, Y. & Kamyshny, A. 2003. Silver Nanoparticles as Pigments for Water-Based Ink-Jet Inks. *Chem Mater*., 15: 2208-2217.

Matsumura, Y., Yoshikata, K., Kunisaki, S. & Tsuchido, T. 2003. Mode of bacterial action of silver zeolite and its comparison with that of silver nitrate. *Appl. Environ. Microbiol*. 69: 4278–4281.

Misiakos, K., Kakabakos, S.E., Petrou, P.S. & Ruf, H.H. 2004. A Monolithic silicon optoelectronic transducer as a real-time affinity biosensor. Anal. Chem. 76: 1366-1373.

Mohan, S., Oluwafemi, S.O., George, S.C., Jayachandran, V.P., Lewu, F.B., Songca, S.P., Kalarikkal, N. & Thomas, S. 2014. Completely green synthesis of dextrose reduced silver nanoparticles, its antimicrobial and sensing properties. Carbohydr. Polym., 106: 469-474.

Nie, S. & Emory, S.R. 1997. Probing Single Molecules and Single Nanoparticles by Surface-Enhanced Raman Scattering. *Science* 275 (1997) 1102- 1106.

Oluwafemi, S.O., Lucwaba,Y., Gura,A., Masabeya,M., Ncapayi,V., Olujimi,O.O. & Songca, S.P. 2013. A facile completely 'green' size tunable synthesis of maltose-reduced silver nanoparticles without the use of any accelerator. *Colloids Surf., B,* 102:718– 723.

Oluwafemi, S.O., Ncapayi, V., Scriba, M. & Songca, S.P. 2013. Green controlled synthesis of monodispersed, stable and smaller sized starch-capped silver nanoparticles. *Mater. Lett.*, 106: 332–336.

Panacek, A., Kvitek, L., Prucek, R., Kolar, M., Vecerova R., Pizurova, N., Sharma, V.K., Nevena, T. & Zboril, Z. 2006. Silver colloid nanoparticles: synthesis, characterization, and their antibacterial activity. *J. Phys. Chem. B,* 110: 16248-16253.

Raveendran, P., Fu, J. & Wallen, S.L. 2003. Completely “Green” synthesis and stabilization of metal nanoparticles. *J. Am. Chem. Soc*., 125: 13940-13941.

Raveendran, P., Fu, J. & Wallen, S.L. 2006. A simple and “green” method for the synthesis of Au, Ag, and Au–Ag alloy nanoparticles. *Green Chem.,* 8:34-38.

Rupp, M.E., Fitzgerald, T., Marion, N., Helget, V., Puumala, S., Anderson, J.R. & Fey, F.D. 2004. Effect of silver-coated urinary catheters: efficacy, cost-effectiveness, and antimicrobial resistance. *Am. J. Infect. Control*, 32: 445-450.

Ryan, M. A., Akinbi, H. T., Serrano, A. G., Perez-Gil, J., Wu, H., McCormack, F. X. & Weaver, T. E. 2006. Antimicrobial activity of native and synthetic surfactant protein B peptides. *J Immunol*., 176 (1): 416-425.

Samuel, U. & Guggenbichler, J.P. 2004. Prevention of catheter-related infections: the potential of a new nano-silver impregnated catheter. *Int. J. Antimicrob. Agents*, 23: S75.

Schneider, J.J. 2001. Organometallic Synthesis. *Adv. Mater*., 13: 529-533.

Sondi, I. & Salopek-Sondi, B. 2004. Silver nanoparticles as antimicrobial agent: a case study on E. coli as a model for Gram-negative bacteria. *J. Colloid Interface Sci., 275*: 177–182.

Stevanovic, M., Kovacevic, B., Petkovic, J., Filipic, M. & Uskokovic, D. 2011. Effect of poly-α, γ, L-glutamic acid as a capping agent on morphology and oxidative stress-dependent toxicity of silver nanoparticles. *Int. J. Nanomedicine*, 6: 2837-2847.

Zhenhua, Z., Wang, S., Zhou, W., Wang, G., Jiang, L., Li,W., Song, S., Liu, J., Sun, G. & Xin, Q. 2003. Novel synthesis of highly active Pt/C cathode electrocatalyst for direct methanol fuel cell. *Chem.Commun*., 394-395.

Chapter 5

Applications of silver nanoparticles: hybrid nanocomposite, sensing and catalytic activity

5.1 Introduction

Introducing the topic of green chemistry has been emphasized in recent research techniques in order to fabricate environmentally benign synthetic routes for chemical products that will reduce or eliminate the use and generation of hazardous substances (Wang et al., 2009). In recent years, nanotechnology has successfully applied green chemistry principles in the synthesis and application of various nanomaterials. In the green synthetic strategy for nanomaterials, utilization of non-toxic chemicals and environmentally friendly solvents have attracted considerable attention due to their advantage in reducing environmental risks (Horvath & Anastas, 2007; Lu et al., 2008). Among various metal nanoparticles, silver nanoparticles (Ag-NPs) have received considerable attention among researchers and companies alike. It has been used in various applications due to its outstanding plasmonic activity, broad spectrum of antibacterial activities, chemical stability, good thermal and electrical conductivity, catalytic properties and recently as sensors for detecting reactive oxygen species (ROS) that possess a serious threat to biological systems (Morones et al., 2005; Ehre et al., 2009; Li et al., 2010; Sharma et al., 2009; Vasileva et al., 2011; Mohan et al., 2014). Though the antibacterial activity of Ag-NPs have led to their wide applications in various fields especially biomedical research and incorporation in many products by various companies, their potential hazards to health and environments have become a source of concern. Another critical challenge is the enhancement of the antibacterial properties while maintaining

their biocompatibility. A scientific approach to this is the development of new hetero-structured nanomaterials with novel properties using non-toxic reagents via environmentally benign synthetic routes. Integration of Ag-NPs into multi -walled carbon nanotubes (MWCNTs) will not only enhance their antibacterial efficacy, biocompatibility and durability, it will also reduce their bio-toxicity and their absorption into the body as well as excretion into the environment.

Carbon nanotubes (CNTs) have attracted much attention due to their remarkable electronic and mechanical properties, thermal stability and high aspect ratio (Iijima , 1991; Hostenson et al., 2001). In order to enhance their chemical compatibility and dispersability for potential applications in biomedicine and biotechnology, extensive research has been focused on the surface modification of CNTs (Hu et al., 2006; Lin et al., 2004). Multiwalled carbon nanotubes (MWCNTs) are more commonly used because of their low cost compared with single-walled carbon nanotubes (SWCNTs). The bulk viscosity of CNT-based materials is high due to its long and tangled structure and this phenomenon will limit the application of MWCNTs. Therefore, in order to solve these problems, it is very important to obtain short and functionalized MWCNTs. Functionalization of the pristine MWCNTs will result in the presence of various functional groups like carboxylic acid (–COOH) and amine ($-NH_2$) on the surface of MWCNTs, while the length of raw MWCNTs will be shortened and debundled simultaneously (Kar & Choudhury, 2013; Khalili et al., 2013). Furthermore, the defects and surface area of functionalized MWCNTs increase and this makes it possible for it to couple other materials (Park et al., 2005; Bahr & Tour, 2002; Liu et al., 2003). The unique properties of both MWCNTs and nanoparticles make them desirable to create novel

MWCNTs/nanocrystal nanohybrids in order to develop novel properties due to interactions between the two materials. In line with this innovation, different approaches have been developed to prepare such nanohybrids (Zhan et al., 2005; Georgakilas et al., 2005; Li et al., 2011; Liu et al., 2012; Akhavan et al., 2011). But they are usually characterized by lengthy synthetic protocols, many complicated steps, degradation of MWCNTs and the use of environmentally hazardous reducing agents and complexants such as $NaBH_4$, formamide, hydroxylamine, dimethylformamide, ammonia or hydrazine. These are not suitable for commercial scale synthesis and will cause negative environmental impacts during application. Several studies on the preparation, characterization, and antibacterial activities of carbon nanostructures combined with Ag nanoparticles have been reported recently. Li *et al.*, 2011 synthesized Ag-NPs supported on MWCNTs by calcinations of the complexes of Ag cation and acid-treated MWCNTs under sparging N_2 with favorable stability and bactericidal properties. Liu *et al.*, 2012reported Ag–Fe-decorated CNTs using DC hydrogen arc discharge method. Akhavan *et al.*, 2011 prepared Ag-NPs entrapped into MWCNTs arrays by treating MWCNTs with $AgNO_3$ and ethanol and carried out antibacterial activity against E. coli. Seo *et al.*, reported the integration of Ag-NPs into MWCNTs using ethyl alcohol as the reducing agent (Seo et al., 2014). The as-synthesised nanoparticles at 30 µg/mL showed high biocompatibility with negligible cytotoxicity to mammalian liver cells. However, the reaction was carried out at small scale and involved the degradation of MWCNTs during the transformation of Ag ions to Ag-NPs. Furthermore, the use of ethyl alcohol as reducing agent raises a lot of biological and environmental concerns for large scale synthesis. As far as we know, the catalytic property of these hybrid structures are not yet exploited.

Hydrogen peroxide one of the reactive oxygen species has been reported as potential pollutant to both aquatic environment and biological system. It is a product of the reactions catalyzed by various oxidase enzymes in biological systems and when presence in excess contributes to DNA damage in living systems (Watt et al., 2007). Therefore its detection especially at trace ppm level concentration has become essential for remedial /control processes. Though there are several reports available for the detection of H_2O_2 using various analytical instruments (Hanaoka et al., 2001; Sunil & Narayana, 2008) which offer excellent sensitivity however, these methods are not cost effective, involve time-consuming procedures, and are skill dependent and use non portable accessories. On the other hand, the use of NPs as colorimetric sensors have proven to be a promising approach for simple and cost-effective protocols with high sensitivity for tracking environmental pollutants in biological systems. Though there have been several reports on the use of Ag-nanocomposite for the detection of H_2O_2 (Seo et al., 2014; Endo et al., 2008), most of these methods have been characterised with the use of toxic reagent like NH_3 and $NaBH_4$ as reducing agent for the preparation of the Ag-nanocomposite, longer detection time and limited detection limit. Therefore, there is need to study the sensing property of green synthesized gelatin capped Ag-NPs and starch capped Ag-NPs against H_2O_2.

As part of utilizing the as-synthesized biopolymer capped silver nanoparticles for various applications, we prepared hybrid nanocomposite by decorating the MWCNTs with Ag-NPs and studied its antibacterial and catalytic properties. The starch capped Ag-NPs and gelatin capped Ag-NPs were screened for their sensing activity against H_2O_2.

5.2 Materials and Methods

5.2.1 Materials

All the chemicals were of analytical grade and used as purchased without any further purification. MWCNTs were purchased from Nanoshell, Chennai. $AgNO_3$ was purchased from Alba cheme, while gelatin, dextrose, P-nitro phenol, sodium borohydride, sulphuric acid, nitric acids and H_2O_2 were from Merck. All glasswares used in the experiments were cleaned and washed thoroughly with double distilled water and dried before use. A cultivating medium, Mueller-Hinton broth, used in the antibacterial assays was supplied by HIMEDIA chennai. Escherichia coli ATCC 10536, and Pseudomonas aeruginosa bacterial strains isolated from human clinical material were used.

5.2.2 Methods

5.2.2.1 Functionalization of MWCNTs (F-MWCNTs)

In a typical procedure, 1.0 g of raw MWCNTs were first treated with a 3:1 mixture of 40 mL concentrated sulfuric and nitric acid. This mixture was stirred for 8 hours under room temperature and then sonicated for 3 hours in an ultrasonic bath to introduce carboxylic acid groups on the MWCNTs surface. The resultant solution was diluted with water, filtered and washed with deionized water until the pH of the filtrate is equal to 7. The prepared F-MWCNTs were then dried in vacuum at 40 ^{0}C overnight.

5.2.2.2 Preparation of silver decorated MWCNTs nanocomposite

In a typical reaction, 1.0 g of gelatin was added into 95 mL of distilled water in a round bottom flask and heated to 40 ^{o}C to get a clear solution. 5 mL of $AgNO_3$ solution (1 M) was added to the gelatin solution with continuous stirring to obtain Ag+/gelatin solution. This was followed by the addition of 10 mL dextrose solution (0.07 M) under continuous stirring. The reaction was maintained at 70 ^{o}C. After 1 hour reaction time, 1.0 g of the F-MWCNTs was added into the solution under continuous stirring. After 48 hours, the solution was filtered to obtain Ag-MWCNTs which were then dried for characterization.

5.2.2.3 Catalytic activity analysis

Catalytic activities of the as synthesized Ag-MWCNTs were carried out by measuring $NaBH_4$ reduction of p-nitrophenol (p-NP) in the presence of Ag-MWCNTs. 10 mL of p-NP (0.4 µM) was mixed with a freshly prepared aqueous solution of $NaBH_4$ (0.10 mL, 0.3 M) under constant stirring in a 25 mL conical flask. Then, 0.3 mL of Ag-MWCNTs-solution was added to the mixture under vigorous shaking. The colour of the solutions changed gradually from yellow to colourless as the reaction time increased. The progress of the reaction was monitored by recording the UV–vis spectra of the solution at a time interval of 60 s. The controlled experiment was also carried out without Ag-MWCNTs for comparison.

5.2.2.4 Study of H_2O_2 sensing by gelatin and starch capped silver nanoparticles

The sensing property of the as-synthesized silver NPs was evaluated following the Endo *et al*., 2008 method with slight modification. Different concentrations of hydrogen peroxide solutions (1000 µL) were introduced into the silver nanoparticle solution in a quartz cuvette at a ratio of 1: 1.5. The change in the UV –Vis spectrum with varying

concentrations of H_2O_2 due to the catalytic reaction between silver nanoparticles and hydrogen peroxide was monitored.

5.2.3 Characterization techniques.

5.2.3.1 Fourier transform Infrared spectroscopy (FTIR)

FTIR spectra of the non-functionalized, acid functionalized and Ag-MWCNTs were recorded with Nicolet-Nexus 670 by spanning along a frequency range from 400 to 4000 cm^{-1}.

5.2.3.2 Raman spectroscopy analysis

The Raman signature peaks of the functionalized samples were analysed using Horiba Jobin Vyon LabRAM HR at laser wavelength of 633 nm. The diluted samples were taken in a glass cuvette and scanned to get the significant peaks.

5.2.3.3 X-ray diffraction (XRD) analysis

The crystallinity of the materials synthesized was analyzed using XRD. XRD measurements were performed on the Bruker D8 Advance diffractometer operating in the reflection mode with Cu-Kα radiation (40 kV, 20 mA) at a wavelength of 1.5418 Å and diffracted beam monochromator. The samples for the XRD measurements were prepared by drying the sample and obtaining powder.

5.2.3.4 High resolution transmission electron microscopic (HRTEM)

The detailed morphology and crystallinity analysis of the samples were done by using JEOL JEM- 3010 electron microscope operating at 200 kV. The samples for TEM and HRTEM analyses were prepared by putting a drop of solution onto an amorphous carbon

substrate supported on a copper grid and then allowing the solvent to evaporate at room temperature.

5.2.3.5 Ultraviolet-visible (UV-Vis) spectroscopy

The absorption properties of the as-synthesized materials were analysed using SHIMDTH UV2401PC spectrophotometer at room temperature. The liquid samples were diluted and the measurements were taken in a quartz cuvette. For the catalytic and sensing property analysis, the absorption measurements were taken to monitor the process.

5.2.3.6 Antimicrobial and bactericidal assays.

Antibacterial activity was evaluated using disc diffusion method. Mueller Hinton broth (MHB) (18 hrs) cultures of two clinical isolates of *E. coli* and *P. aeruginosa* were evaluated in this study. 10 µL of the Ag-NPs and Ag-MWCNTs solutions were added to a filter paper disc and dried at 30 ^{0}C in an incubator. A stock solution of $AgNO_3$ was prepared with same concentration and checked for the purpose of comparison. Strict aseptic conditions were maintained throughout the procedure. Bacterial cultures were swabbed on Mueller-Hinton agar (MHA) plate and surface of the media was allowed to dry for 30 minutes. This was followed by pressing the nanoparticles incorporated discs gently on the agar surface at specified distance. After incubation at 37 ^{o}C overnight, formation of inhibition zones was checked and the diameter of inhibition zones were measured.

5.3 RESULTS AND DISCUSSIONS

5.3.1 Synthesis of Ag-MWCNTs hybrid nanocomposite

MWCNTs tend to aggregate because of the high aspect ratio and strong van der Waals attraction between the MWCNTs. This results in poor solubility in most solvents and thus limits its practical applications (Guo & Li, 2005). Functionalisation of the surface improves the dispersion of MWCNTs. After refluxing in concentrated HNO_3 and H_2SO_4, carboxylic acid (–COOH) group are attached to the defect sites of the MWCNTs (Marshall et al., 2006). The acid functionalization of MWCNTs was confirmed by FTIR spectroscopy. The FT-IR spectra of the pristine MWCNTs, purified MWCNTs and F-MWCNTs are shown in Fig. 5.1. The Pristine MWCNTs spectrum shows a peak centered at 1570 cm^{-1}, which can be assigned to the C=C stretching of carbon nanotube backbones (Watt et al., 2007). The F-MWCNTs spectrum shows peaks at 1706 cm^{-1} and 1260 cm^{-1} which were characteristic absorption peaks for C=O and C–O stretching bands of carboxylic acid groups (Hanaoka et al., 2001; Sunil & Narayana, 2008) . In addition, free hydroxyl (-OH) absorption band was observed between 3300 ~ 3500 cm^{-1} in the F-MWCNTs spectrum indicating successful functionalization of the MWCNTs. The presence of carboxylic acid groups on the sidewalls of the MWCNTs is very important because these groups can act as anchor groups to couple with other materials.

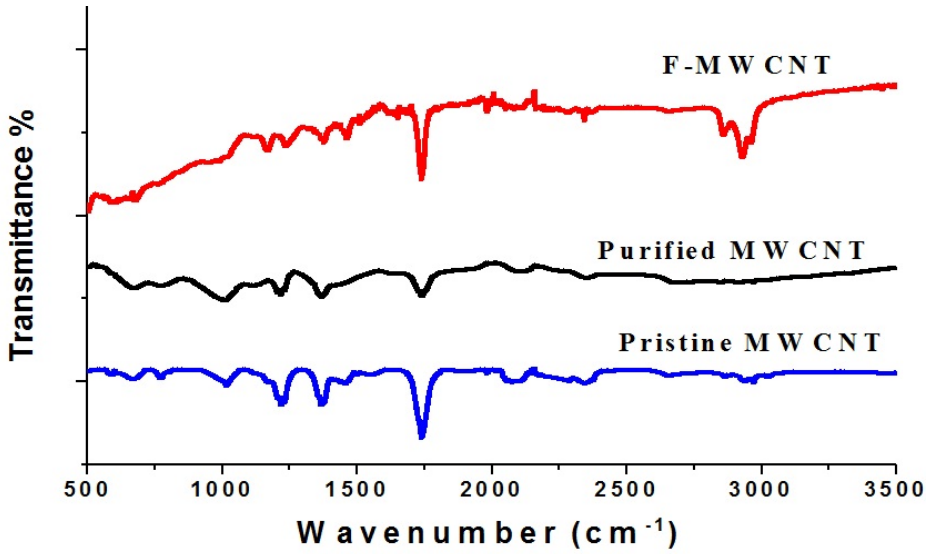

Figure 5.1: FTIR spectra of Pristine-MWCNTs (A), Purified MWCNTs (B) and F-MWCNTs (C)

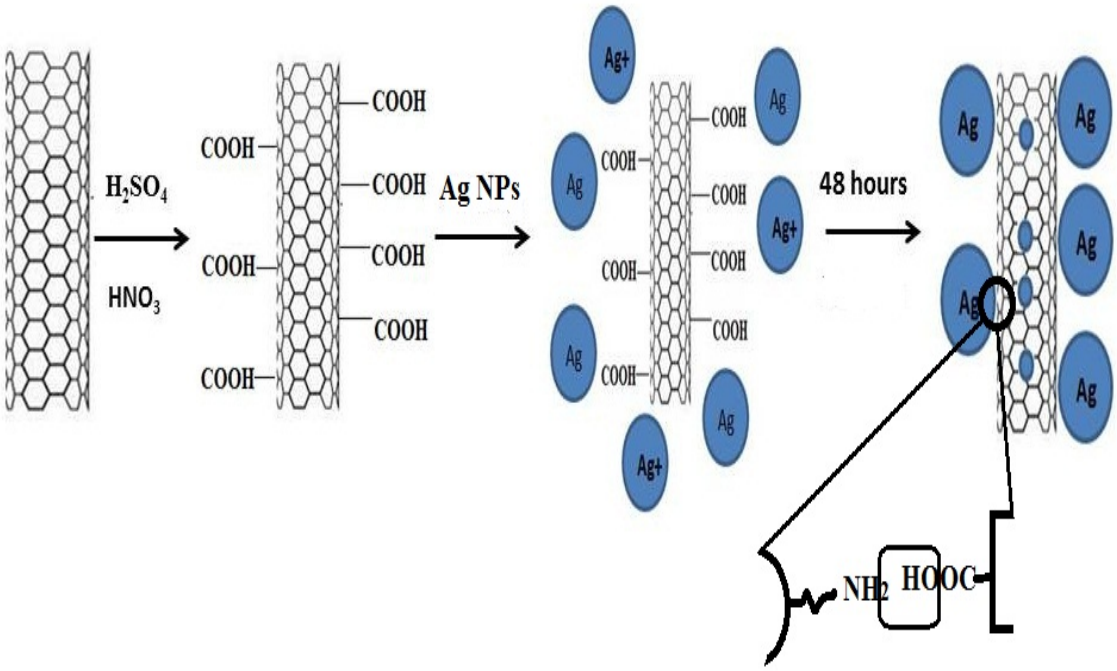

Figure 5.2: Schematic diagram indicating the mechanism for the formation of Ag-MWCNTs nanocomposites.

After the addition of F-MWCNTs into the silver solution, silver functionalized MWCNTs (Ag-MWCNT) was obtained. The Ag-NPs interact with F-MWCNTs through the gelatin -NH_2 group to form a covalent bond with the carboxyl group of the F-MWCNTs. The FTIR spectrum of the Ag-MWCNTs given in Figure 5.3 clearly shows the covalent bond formed between F-MWCNTs and Ag-NPs. A broad peak between 2965- 3664 cm^{-1} shows the presence of –CO-NH- bond formed between the amine group of gelatin and carboxyl group of F-MWCNTs. The presence of amide linkage is again confirmed by the peaks at 1549 cm^{-1} which is due to the –NH bend. A sharp peak at 1296 cm^{-1} is due to the amide linkage caused by the –C-N stretch plus –NH in phase bending (Oraby et al., 2013). A sharp peak at 1025 cm^{-1} may be due to the –C-O stretching vibration from gelatin. A significant peak at 1619 cm^{-1} is attributed to the carbonyl group (–C=O) vibration. Two small peaks at 588 cm^{-1} and 666 cm^{-1} corresponds to the deformation vibrations of metal oxygen bond between Ag-O (Deneva, 2010). The schematic diagram indicating the mechanism for the formation of Ag-MWCNTs nanocomposites is shown in Fig. 5.2.

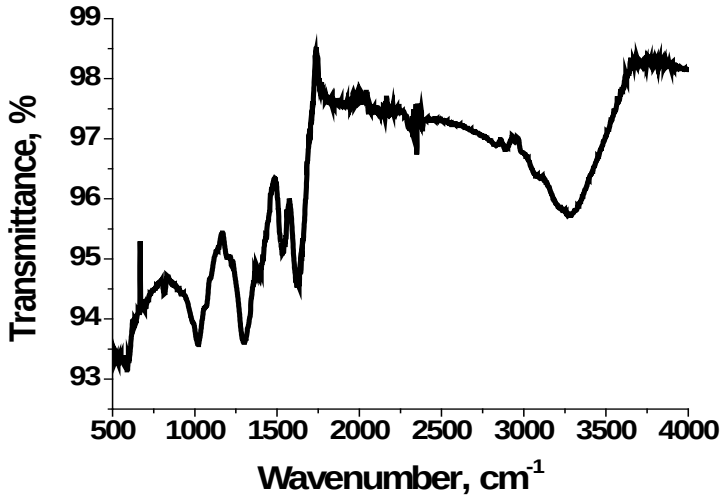

Figure 5.3: FTIR spectra of Ag -MWCNTs

5.3.1.1 X- ray diffraction analysis

The X-ray diffraction patterns of the F-MWCNTs and the as-synthesized Ag-MWCNTs are shown in Figure 5.4. The diffraction pattern for the F-MWCNTs in Fig. 5.4A shows two peaks at $2\theta = 25.8^{o}$ and 42.7^{o} assigned to the graphite crystalline phase of MWCNTs which corresponds to the (002) and (110) planes respectively. Compared to the normal graphite peak at $2\theta = 26.5^{o}$, this peak shows a downward shift; which is attributed to an increase in the sp^2, C=C layers spacing (Kastner et al., 1994). The diffraction pattern for Ag-MWCNTs nanocomposite (Figure 5.4B) shows four diffraction peaks at $2\theta = 38.48$, 44.32, 64.2, and 77.64◦ corresponding to (111), (200), (220), and (311) crystalline planes of the face centered cubic (fcc) crystalline structure of metallic silver, respectively (JCPDS file No. 04-0783). In addition, the characteristic Bragg diffraction peak of MWCNTs which is at about 25.8^{o} is also retained in the composite. The XRD results showed that the composites composed of Ag and MWCNTs and confirmed its crystallinity.

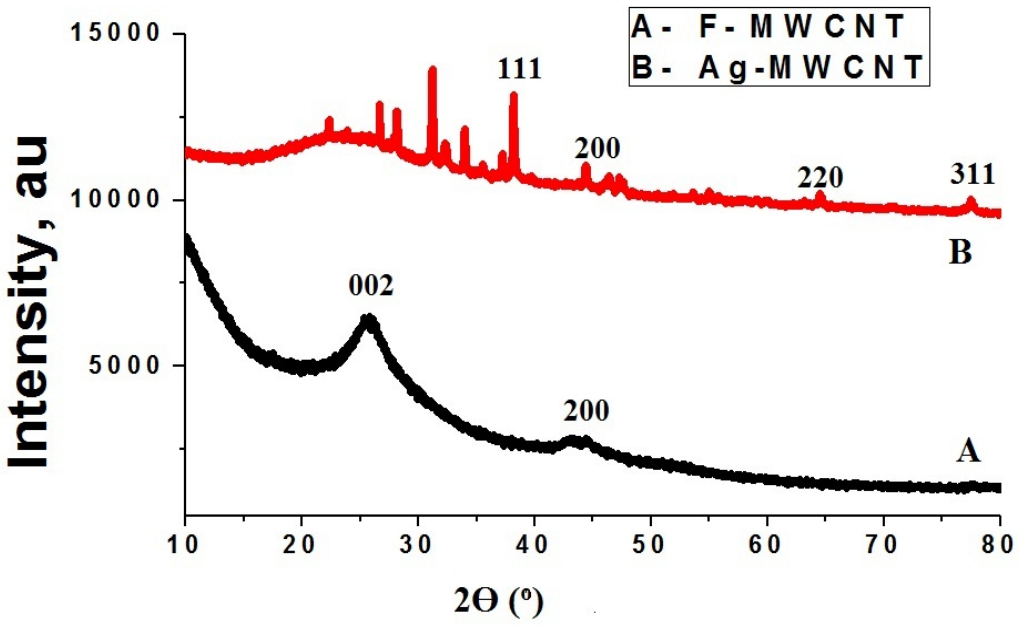

Figure 5.4: X-ray diffraction patterns of (A) F-MWCNTs and (B) Ag-MWCNTs

5.3.1.2 Raman spectroscopy Analysis

Figure 5.5 shows the Raman spectra of MWCNTs, F-MWCNTs and Ag-MWCNTs. Three characteristic bands corresponding to the D band (defect), G band (graphite band) and G' band (D overtone) of the MWCNTs were observed at 1324 cm^{-1}, 1574 cm^{-1} and 2644 cm^{-1} respectively (Figure 5.5 A). The D' band which indicates the structural defect of the MWCNTs, F-MWCNTs and Ag-MWCNTs hybrid nanocomposites were found at 1601 cm^{-1}, 1608 cm^{-1} and 1611 cm^{-1} respectively (Figure 5.5A-C). The shift in D' band of the Ag-MWCNTs to higher wavenumber compared to the MWCNTs is attributed to both structural defects after functionalisation and broadening caused by modification with Ag-NPs (Zhang et al., 2002) . The G' peak of the Ag-MWCNTs hybrid nanocomposites shifted to higher wavenumber (2688 cm^{-1}) compared with MWCNTs and F-MWCNTs (2644 cm^{-1} and 2680 cm^{-1} respectively). The shift in the G' peak is attributed to a

substantial charge transfer interaction between the Ag-NPs and F-MWCNTs (Peng et al., 2004) . Zhang *et al*., (Corio et al., 2004) and Santangelo *et al*.,(Zhang et al., 2011) had shown that information related to the amount of structural defects and sp^3 hybridised carbon atom as well as the degree of side wall functionalization can be obtained from the relative intensity of the D and G bands (I_D/I_G).

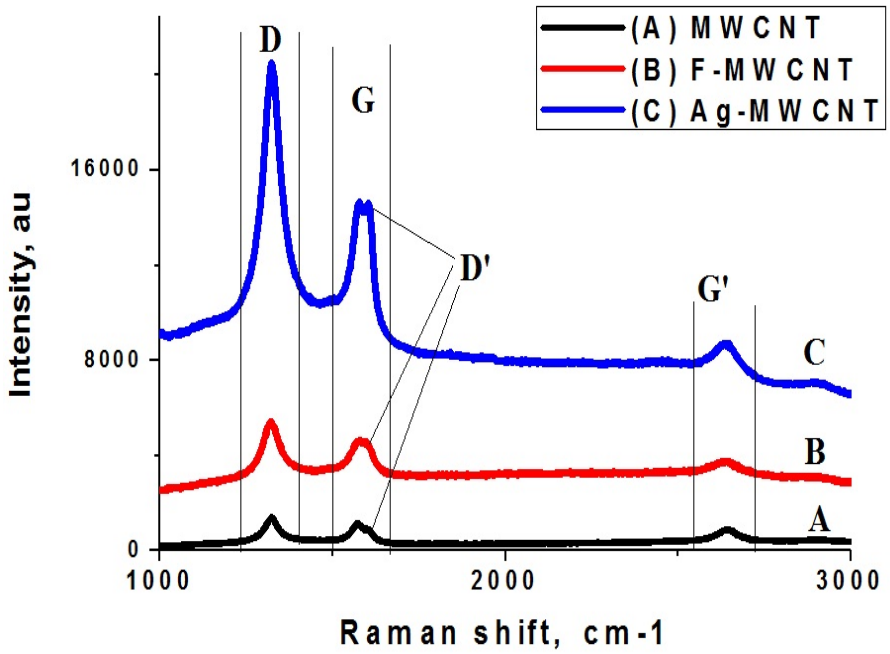

Figure 5.5: Raman spectra of MWCNT, F_MWCNT and Ag-MWCNT nanocomposite.

The degree of crystallinity and the scale on which the graphitic order extends can be understood from the relative intensity of the G' and D bands ($I_{G'}/I_D$) and relative intensity of the G' and G bands ($I_{G'}/I_G$) respectively. The relative intensities of the D/G, G'/D and G'/G ratios are presented in Figure 5.6. The D/G ratios are 1.176, 1.233, and 1.499 for the MWCNTs, F-MWCNTs, and Ag-MWCNTs hybrid nanocomposites, respectively. The increase in the D/G ratio of F-MWCNTs compared with that of the MWCNTs confirms

successful introduction of functional groups on the MWCNTs surface and also indicated that, the outer layers of the MWCNTs were chemically modified (Corio et al., 2004). An increase in the D/G ratio of Ag-MWCNTs hybrid nanocomposites when compare with that of F-MWCNTs can be attributed to the introduction of Ag nanoparticles on the surface of the F-MWCNTs. The G'/G ratios are 0.78, 0.76, and 0.48 for MWCNTs, F-MWCNTs, and Ag-MWCNTs hybrid nanocomposites, respectively while the G'/D ratios are 0.66, 0.62, and 0.32 for the MWCNTs, F-MWCNTs and Ag-MWCNTs hybrid nanocomposites respectively. The decrease in the G'/G and G'/D ratios of the F-MWCNTs compared with those of the MWCNTs has been attributed to the presence of higher density of lattice defects in the F-MWCNTs. The intensity of the G' peak of the Ag-MWCNTs hybrid nanocomposites increases due to the increase in mass fraction of MWCNTs in the hybrid material. The G' peak arises from a two-phonon process, and the increase in G’ intensity shows the sample becoming more ordered by, not interfering on the coupling effect that is required for the two-phonon process. This effect is different compared to the earlier reports which shows normal decrease in G’ after its surface functionalization (Melvin et al., 2014) . The G'/G and G'/D ratios of the Ag-MWCNTs hybrid nanocomposites showed the lowest values. This is due to the structural defects formation arising from the interaction between the Ag-NPs and the MWCNTs.

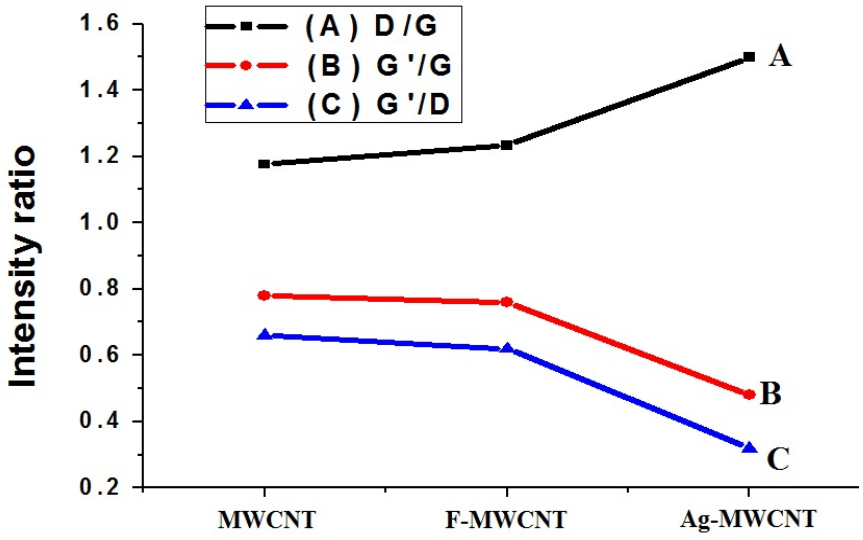

Figure 5.6: Relative intensity ratios of D/G, G'/G, and G'/D peaks of MWCNTs, F-MWCNTs and Ag-MWCNTs hybrid nanocomposites

5.3.1.3 High resolution transmission electron microscopic analysis

The electron microscope images of the Ag-NPs and Ag-MWCNTs are shown in Fig. 5.7. The TEM image of the Ag-NPs (Fig. 5.7A) indicates that the particles are small, spherical and well dispersed with an average particles size of 9.88 ± 1.23 nm. The TEM image of Ag-MWCNTs hybrid nanocomposites shown in Fig. 5.7 B clearly shows the presence of Ag-NPs grafted on the surface of F-MWCNTs. Ag-NPs are homogeneously dispersed with no agglomeration and are strongly adhered to the surfaces of the F-MWCNTs. The aveage diameter of the Ag-NPs grafted onto the surface of the F-MWCNTs was found to be 9.68 ± 1.44. The diameter and aspect ratio of the F-MWCNTs was about 32.9 ± 1.37 nm and 6 nm respectively. Fig. 5.7C shows aligned Ag- NPs on the surface of F-MWCNTs with inset showing the SAED image of the Ag-MWCNTs nanocomposite. The SAED diffraction pattern (Fig. 5.7C (inset)) confirmed the crystallinity of the Ag-

MWCNTs nanocomposite. Fig. 5.7 D shows the high resolution image of a single silver nanoparticle on the surface of the MWCNTs.

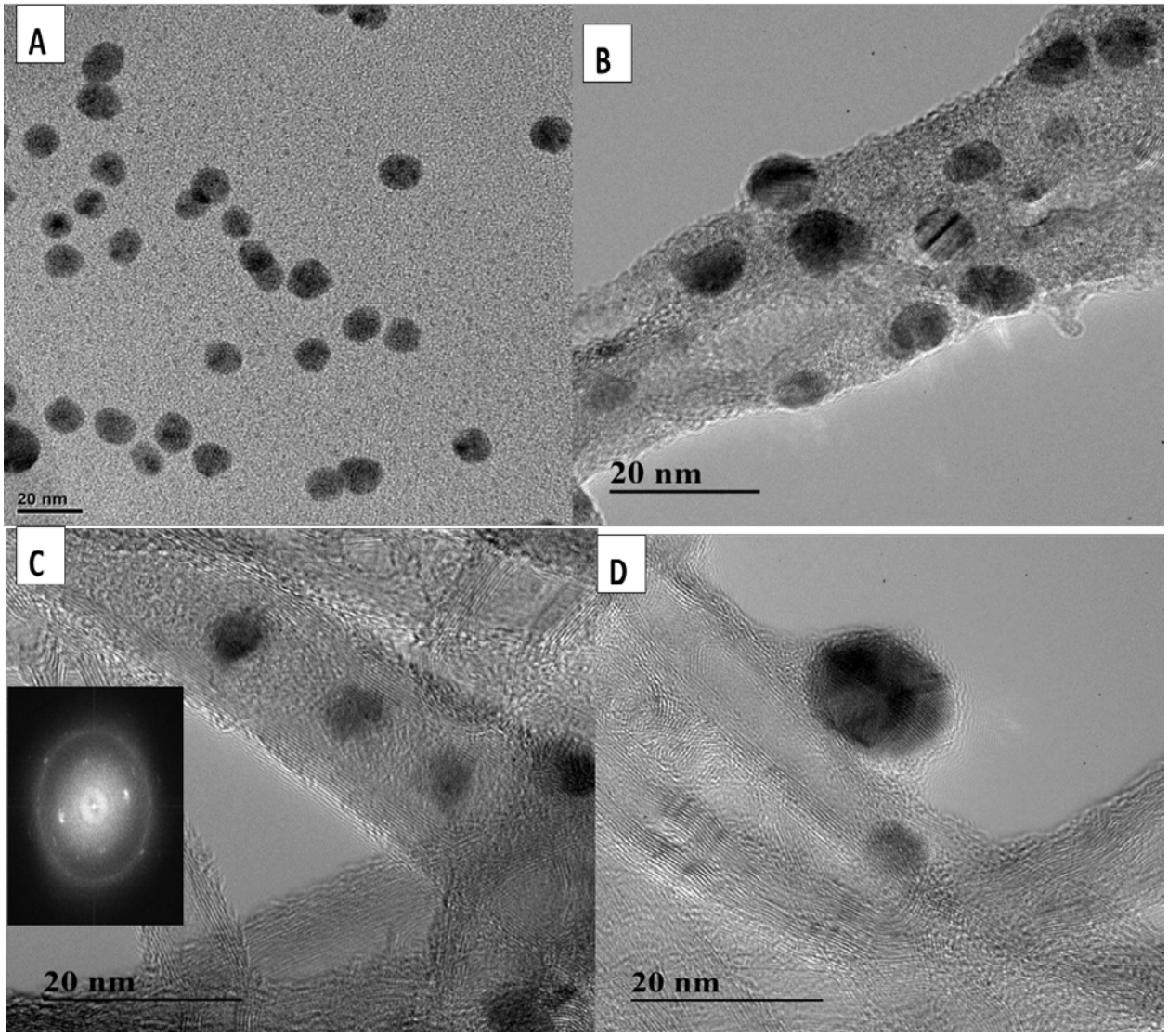

Figure 5.7: TEM images of (A) Ag-NPs (B) Ag-MWCNTs (C) Aligned Ag- NPs on F-MWCNTs (inset : SAED image of Ag-MWCNT) and (D) Single Ag-NP on the MWCNTs surface .

5.3.1.4 Antibacterial activity

The antibacterial activities of Ag-MWCNTs nanocomposites were assessed with the paper-disk diffusion method. As shown in Fig. 5.8, Ag-MWCNTs exhibit significant inhibitory effects on *E. coli* and *P.aregunosa.* For comparison, antibacterial activities of Ag-NPs and F-MWCNTs were studied and the results of inhibition zones are given in Table 5.1. The results show that both F-MWCNTs and Ag-NPs show lower activities towards *E.coli* than Ag-MWCNTs while in the case of *P. aregunosa*, the Ag-MWCNTs is the least effective. The inhibitory result indicates that Ag-MWCNTs could hinder the growth of bacteria by direct contact, in which the cell membrane was ruptured and surface charge interactions between Ag-MWCNTs and the bacteria were initiated (Seo et al., 2014) .

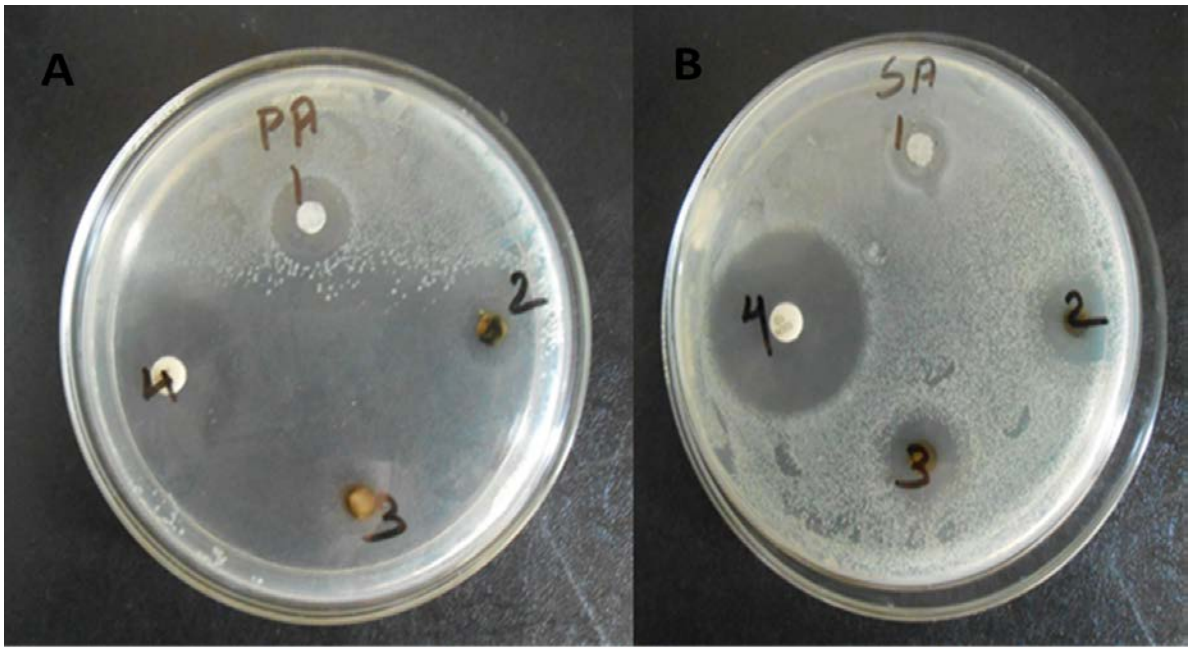

Figure 5.8: Results of the antibacterial test carried out using paper-disk diffusion method against (A) Gram positive pseudomonas and (B) Gram-negative E. coli bacteria.

Table 5.1 : Average diameter of inhibition zone for functionalised CNT, Ag-MWCNT and silver nanoparticles against E. coli and P. aeruginosa.

Sl.No	Sample	Diameter zone of inhibition (mm)	
		E.coli (ATCC 25922)	P.aeruginosa (ATCC 27853)
1	CNT COOH	11	16
2	CNT AG	15	10
3	Spherical Ag	14	11
4	Gentamycin	24	21

5.3.1.5 Catalytic activity

Catalytic activities of Ag-MWCNTs for the conversion of p-nitrophenol (p-NP) to p-aminophenol (p-AP) in the presence of $NaBH_4$ were studied using the UV-vis absorption spectrophotometer. Fig. 5.9 (A) shows the absorption spectra for the reduction of P-nitophenol at different reaction time. In the absence of Ag-MWCNTs nanocomposites, the solution containing p-NP and $NaBH_4$ shows absorption band maximum at ~ 400 nm. This band correspond to the p-nitrophenolate ion under alkaline condition. After addition of a small amount of Ag-MWCNTs nanocomposite to the above reaction mixture under continous stiring, the colour of the solution changes gradually from yellow to colourless within 120 sec. A time-dependent UV–vis spectra of this reaction shows gradual reduction in the absorbance of the peak at 400 nm accompanied by a gradual development of a new peak at 270 nm. The new band at 270 nm is attributed to the formation of p-AP.

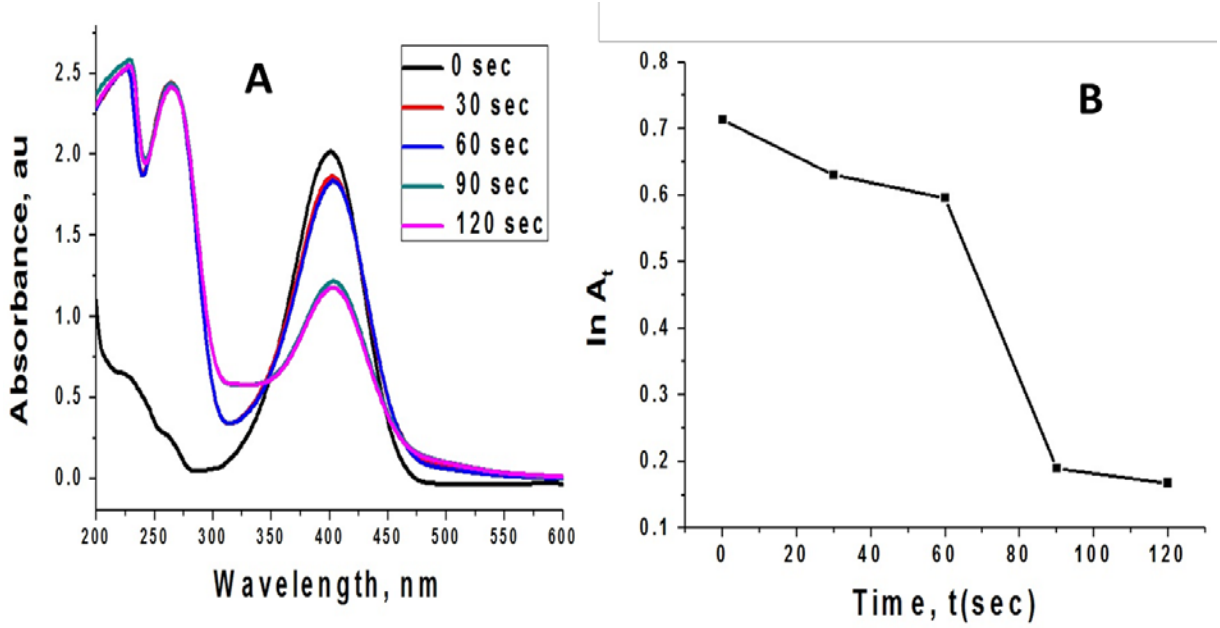

Figure 5.9: (A) UV–vis spectra of p-nitrophenol at different time interval during its reduction by $NaBH_4$ in presence of Ag-MWCNTs as catalyst (B) Plots of 'ln At ' vs. time 't' (s) for the reduction of p-nitrophenol to paminophenol by $NaBH_4$ in presence of Ag-MWCNT .

The catalytic conversion of p-NP to p-AP follows the first order kinetics. In this reaction, the reaction rate constant has been evaluated by plotting the 'ln At' versus time 't'; where At is absorbance at any time, 't' and the calculated value is $5.18\times 10^{-1}s^{-1}$. The approximate linear relations of ln At versus 't' observed for all the reaction times as shown in Fig. 5.9 (B), support the first-order kinetics. We proposed that hydrogen from sodium borobydride is transferred to the Ag-MWCNTs by the decomposition of borohydride and this hydride species then reacts with p-NP to yield the product p-AP (Bhui & misra, 2012). The Ag-MWCNTs here act as a template for the transfer of H^+ from $NaBH_4$ and initiate the reduction process. Langmuir–Hinshelwood mechanism can

be used to model the kinetics of the reaction where both reactants need to be adsorbed on the surface prior to reaction (Xu et al., 2008) . The mechanism is schematically displayed in Figure 5.10. The rate-determining step is governed by the reaction of the adsorbed species. The adsorption/desorption equilibrium is assumed to be much faster and is modeled in terms of a Langmuir isotherm. The rate of reduction is independent of $NaBH_4$ concentration because when this reagent was used in excess compared to p-NP, there was no change in the absorption spectra. The isosbestic points in the UV–vis spectra demonstrate with high precision that p-NP is converted to p-AP with no side reaction.

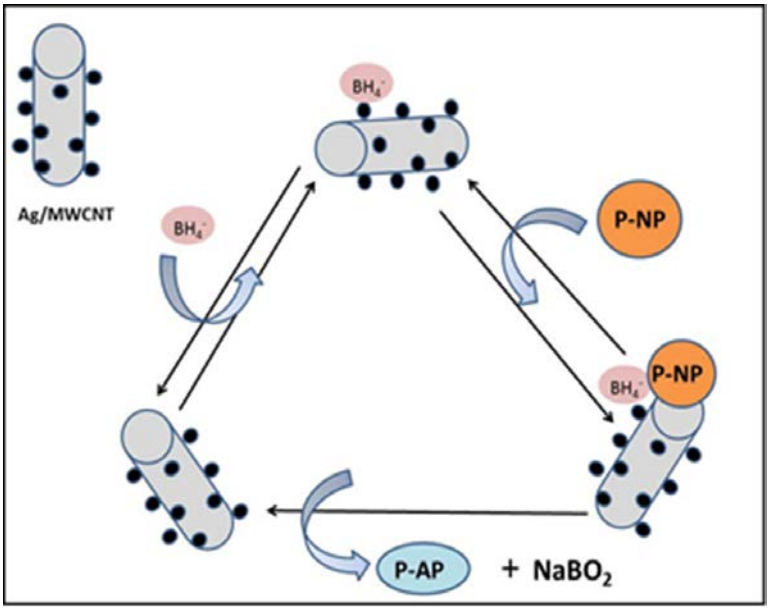

Figure 5.10: Mechanistic model of Langmuir–Hinshelwood mechanism for the reduction of p-NP to p-AP by sodium borohydride in presence of Ag-MWCNTs nanoparticles.

5.3.2 Sensing Application.

5.3.2.1 Sensing property of gelatin capped silver nanoparticles towards H_2O_2

The sensing property of gelatin-capped Ag-NPs were analysed by measuring their sensitivity against H_2O_2. Figure 5.11 shows the change in the maximum SPR peak position of the Ag-NPs after the addition of H_2O_2 at different concentrations. The absorbance was measured 60 seconds after the addition of H_2O_2 solution. A red-shift in the LSPR peak position from 426 nm to 438 was observed after the addition of H_2O_2 solution. In addition, the colour of the solution changes gradually from yellow to colourless depending on the concentration of the hydrogen peroxide. The linear regression coefficient (R^2) was found to be 0.81543 with the lowest detection limit of 10^{-6}M. This hyperchromic shift in the LSPR peak position and the change in the colour of the solution have been attributed to the redox reaction between the Ag-NPs and hydrogen peroxide (Pal et al., 1988). The reaction between the Ag-NPs and H_2O_2 caused the destruction of the gelatin coating of the Ag-NPs thus, making the aggregation of the nanoparticles inevitable and therefore increased in the particle size as evident by the red-shifting of the LSPR peak position (Figure 5.10 inset). A schematic representation of the possible mechanism is given in Figure 5.12(A). When the concentration of the H_2O_2 solution added to the Ag-NPs increased, a decrease in the λ_{max} intensity was observed. The observed decrease in the absorbance intensity implies decrease in the Ag-NPs concentration (Figure 5.12 B). The decrease in the absorbance is proportional to the concentration of the H_2O_2 solution. The higher the peroxide concentration, the stronger the decrease in the Ag-NPs concentration in the solution and hence, lowering of the Ag-NPs LSPR peak intensity. A schematic representation of the catalytic action of Ag-NPs in

the presence of H_2O_2 is given in Figure 5.12 (B). The nanoparticles used here are protected by a gelatin layer. The redox reaction between silver and hydrogen peroxide occurs through the protection layer of gelatin around the Ag-NPs. The introduction of ROS species like H_2O_2 in the solution, forms reactive radical species and initiates the degradation of the gelatin protected Ag-NPs. This results in the oxidation of Ag to Ag^+ ions and thereby decrease in the LSPR absorbance.

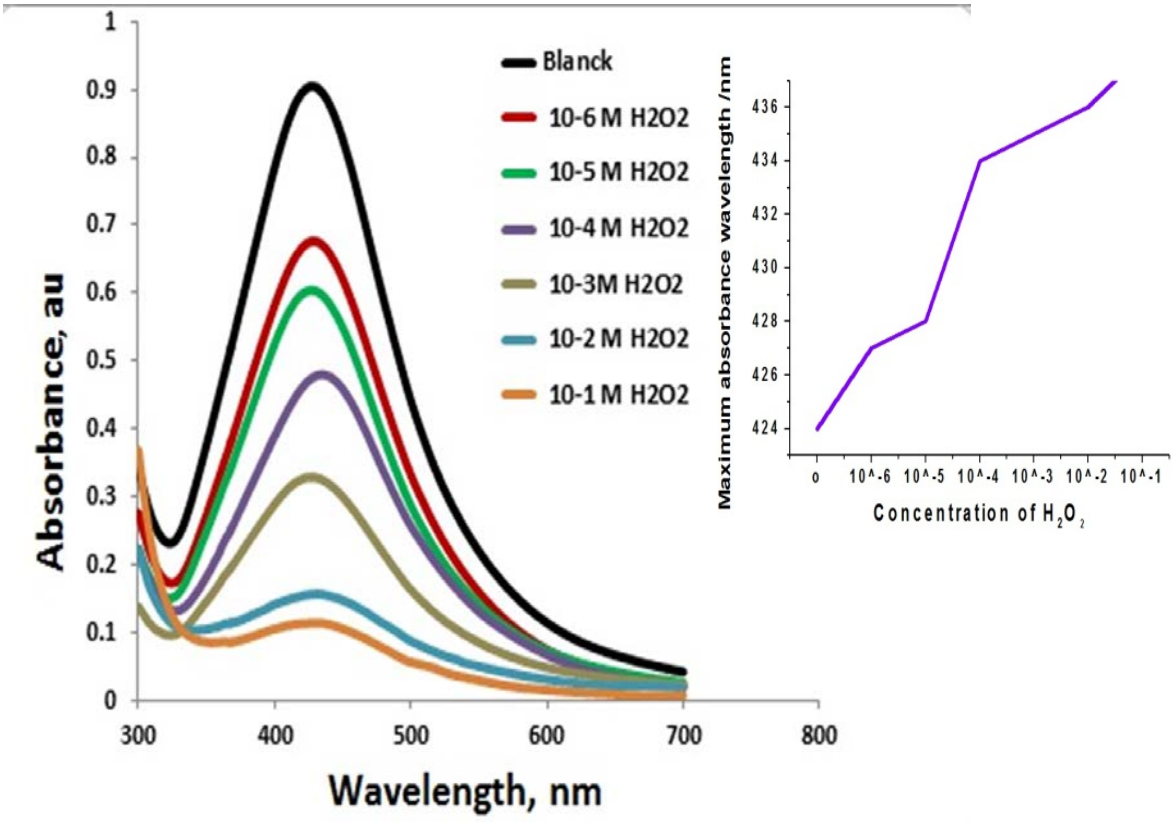

Figure 5.11: Change in the LSPR peak position after the addition of H_2O_2 at different concentration. Inset: graph of H_2O_2 concentration against the SPR peak position

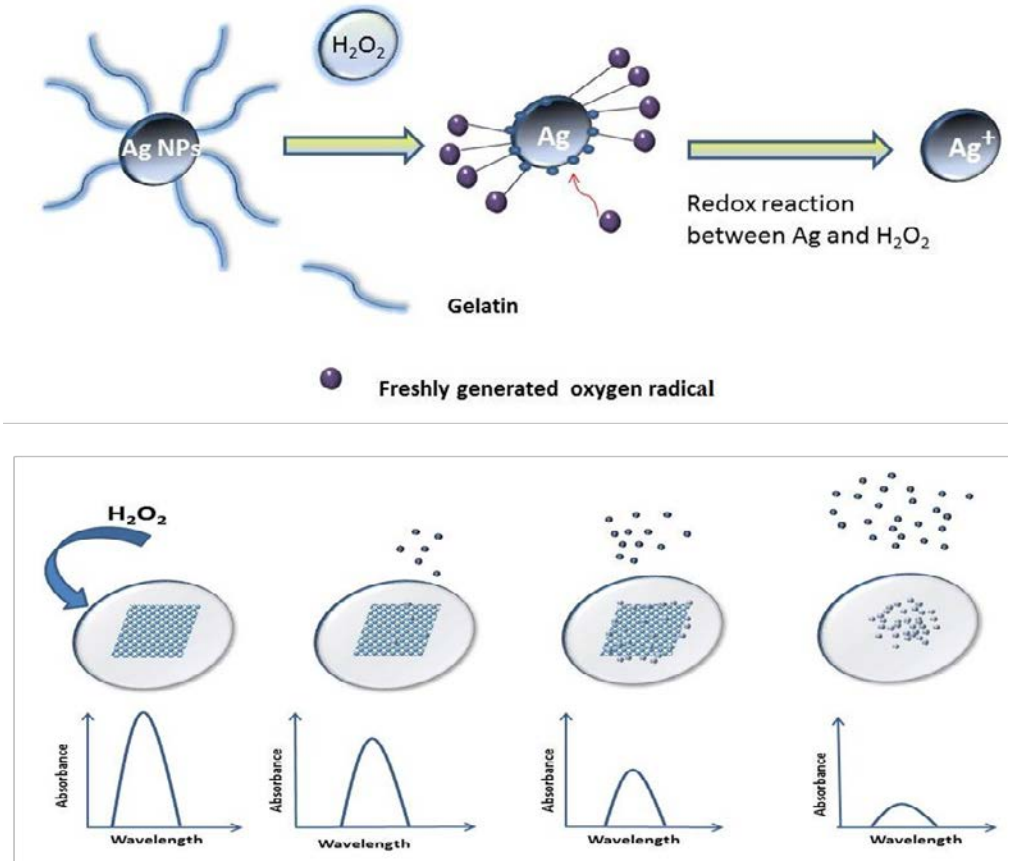

Figure 5.12: Possible mechanism and schematic representation of (A) reaction between Ag-NPs and H_2O_2 and (B) decrease in the absorbance intensity with increase in concentration of H_2O_2.

5.3.2.2 Sensing property of starch capped silver nanoparticles towards H_2O_2

The typical absorption spectra for the sensitivity of starch –capped Ag-NPs towards different H_2O_2 concentrations ($1x10^{-1}$ M – $1x\ 10^{-10}$M) are shown in Fig. 5.13 (A). The absorbance was measured 60 s after the addition of different H_2O_2 concentration. After the addition of H_2O_2, the colour of the solution changes gradually from dark brown to colourless depending on the concentration of the hydrogen peroxide. This is accompanied by a red-shift in the SPR peak position of Ag-NPs from 405 to 417 as the H_2O_2

concentration increased. The red-shift in the SPR peak position has been attributed to the increase in the particle size of the Ag-NPs. The reaction between the Ag-NPs and H_2O_2 caused the destruction of the starch coating on the surface of the Ag-NPs thus, making the aggregation of the nanoparticles inevitable and therefore increased in the particle size as evident by the red-shifting of the SPR peak position (Figure 5.13B). The spectra also indicate that increase in the concentration of the H_2O_2 solution led to the decrease in the maximum intensity. The observed decrease in the absorbance intensity implies decrease in the amount of smaller Ag-NPs originally present in the solution.

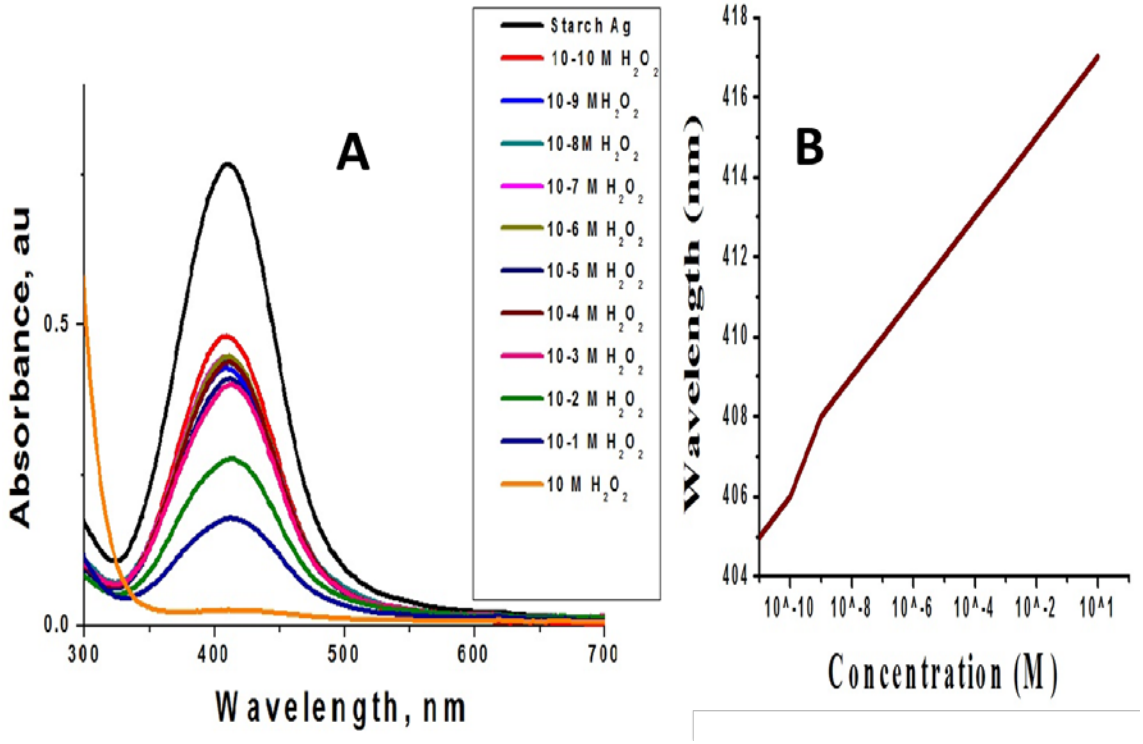

Figure 5.13 : (A) Change in the LSPR peak position after the addition of H_2O_2 at different concentration. (B) Graph of H_2O_2 concentration against the SPR peak position.

The decrease in the absorbance is proportional to the concentration of the H_2O_2 solution. The higher the peroxide concentration, the stronger the decrease in the Ag-NPs concentration and hence, lowering of the Ag-NPs SPR peak intensity. The introduction of H_2O_2 in the solution forms reactive radical species and initiates the degradation of the starch protected Ag-NPs (Mohan et al., 2014). This degradation increase particle aggregation and decrease the amount of smaller Ag-NPs concentration in the solution and hence, lowering of the Ag-NPs SPR peak intensity. The linear regression coefficient (R^2) was found to be 0.88223 with the lowest detection limit of 10^{-10}M. In comparison with previous report by Filippo et al., 2009 and Vasileva et al., 2011 the present study offer faster detection time (within one minute) with high sensitivity. This is in addition to the fact that, the synthesis involved completely green processes without the use of any accelerator or additional complexant and the products are highly stable and biocompatible.

5.4 Conclusions

Ag-MWCNTs nanocomposite were successfully synthesized via a simple, straightforward and facile method without degradation of the MWCNTs. The method involves the use of biodegradable and biocompatible reagents and is suitable for large scale synthesis without additional chemicals, complexant, irradiations, ultrasound, optical and electric treatments. The surface chemistry investigated using FTIR and Raman spectroscopy analyses confirmed the formation of Ag-MWCNTs. The as-synthesised Ag-NPs were homogenously dispersed in the MWCNTs while the XRD and TEM confirmed the crystalline nature of the Ag-MWCNTs. The Ag-MWCNTs nanocomposites show high

antibacterial activity against E-coli compared to the Ag-NPs and MWCNTs. The catalytic activity of the hybrid nanocomposites demonstrated by studying its effect in the conversion of p-nitrophenol to p-aminophenol (p-AP) in the presence of $NaBH_4$ follows first order kinetics with a rate constant of $5.18\times 10^{-1}S^{-1}$. By this environmental friendly technique, Ag-MWCNTs nanocomposites with enhanced antibacterial efficacy, durability and biocompatibility as well as reduced biotoxicity and environmental impacts can be easily synthesized on a large scale. This will further improve its practical applications in the areas of biomedical research, catalysis, environmental engineering, and water purification.

The sensing property of biopolymer capped Ag-NPs showed promising results. The degradation of silver nanoparticles induced by the decomposition of hydrogen peroxide causes a significant change in the LSPR absorbance depending on the H_2O_2 concentration. The gelatin Ag-NPs based sensor has a very good sensitivity and a linear response over the wide H_2O_2 concentration range of 10^{-1} to 10^{-6} M H_2O_2. Compared to gelatin-capped Ag-NPs, starch capped Ag-NPs showed better sensitivity upto a lower concentration. It showed a linear response over a wide concentration range from 10^{-1} to 10^{-10}. This method offers a simple and cost effective approach with high sensitivity for the detection of H_2O_2. Thus, providing a promising non-skill dependent approach with high sensitivity for remedial /control processes of environmental pollutant.

Reference

Akhavan, O., Abdolahad, M., Abdi, Y. & Mohajerzadeh, S. 2011. Silver nanoparticles within vertically aligned multi-wall carbon nanotubes with open tips for antibacterial purposes. *J. Mater. Chem.,* 21: 387-393.

Bahr, J. L. & Tour, J. M. 2002. Covalent chemistry of single-wall carbon nanotubes. *J. Mater. Chem.,* 12:1952-1958.

Bhui, D. K. & Misra, A. 2012. Synthesis of worm like silver nanoparticles in methyl cellulose polymeric matrix and its catalytic activity. *Carbohydr. Polym.,* 89: 830-835.

Corio, P., Santos, A. P., Santos, P.S., Temperini, M.L.A. & Brar, V.W. 2004. Characterization of single wall carbon nanotubes filled with silver and with chromium compounds. *Chem. Phys. Lett*., 383: 475-480.

Deneva, M. 2010. Infrared spectroscopy investigation of metallic nanoparticles based on copper, cobalt and nickel synthesized through borohydride reduction method. *J. Univ. Chem. Tech. Metal,* 45: 351-378 .

Ehre, A.D., Mamane, H., Belenkova, T., Markovich, G. & Adin, A. 2009. Silver nanoparticle–E. coli colloidal interaction in water and effect on E. coli survival. *J. Colloid Interface Sci.,* 339:521- 526.

Endo, T., Yanagida, Y. & Hatsuzawa, T. 2008. Quantitative determination of hydrogen peroxide using polymer coated Ag nanoparticles. *Measurement*, 41:1045–1053.

Filippo, E., Serra, A., Manno, D. 2009. Poly(Vinyl Alcohol) Capped Silver Nanoparticles as Localized Surface Plasmon Resonance-Based Hydrogen Peroxide Sensor. *Sens. Actuators B*, 138: 625–630.

Georgakilas, V., Tzitzios, V., Gournis, D. & Petridis, D. 2005. Attachment of Magnetic Nanoparticles on Carbon Nanotubes and Their Soluble Derivatives. *Chem. Mater.* 17: 1613-1617.

Guo, D. J. & Li, H. L. 2005. Highly dispersed Ag nanoparticles on functional MWNT surfaces for methanol oxidation in alkaline solution. *Carbon* 43:1259-1264.

Hanaoka, S., Lin, J. & Yamada, M. 2001.Chemiluminescent flow sensor for H_2O_2 based on the decomposition of H_2O_2 catalyzed by cobalt(II)-ethanolamine complex immobilized on resin. *Anal. Chem. Acta,* 426 (1): 57–64.

Horvath, I.T. & Anastas, P.T. 2007. Introduction: green chemistry. *Chem. Rev.,* 107: 2167- 2173.

Hostenson, E. T., Ren, Z. F. & Chou, T. W. 2001. Advances in the science and technology of carbon nanotubes and their composites: A Review. *Compos. Sci. Technol*., 61:1899-1912.

Hu, Y., Shenderova, O. A., Hu, Z., Padgett, C. W. & Brenner, D. W. 2006. Carbon nanostructures for advanced composites. *Rep. Prog. Phys*., 69:1847-1895.

Iijima, S. 1991. Helical microtubules of graphitic carbon. *Nature* 354: 56- 58.

Kar, P. & Choudhury, A. 2013. Carboxylic acid functionalized multi-walled carbon nanotube doped polyaniline for chloroform sensors. *Sens. Actuators B,* 183: 25-33.

Kastner, J., Pichler, T., Kuzmany, H., Curran, S., Blau, W., Weldon, D.N., Delamesiere, M., Draper, S. & Zandbergen, H. 1994. Resonance Raman and infrared spectroscopy of carbon nanotubes. *Chem. Phys. Lett*., 221:53-58.

Khalili, S., Ghoreyshi, A. A., Jahanshahi, M. & Pirzadeh, K. 2013. Enhancement of Carbon Dioxide Capture by Amine-Functionalized Multi-Walled Carbon Nanotube. *Clean – Soil, Air, Water,* 41: 939-948.

Li, W., Xie, X., Shi, Q., Zeng, H., Yang, Y.O. & Chen, Y. 2010. Antibacterial activity and mechanism of silver nanoparticles on Escherichia coli. *Appl. Microbiol. Biotechnol*., 85: 1115-1122.

Li, Z., Fan, L., Zhang, T. & Li, K. 2011. Facile synthesis of Ag nanoparticles supported on MWCNTs with favorable stability and their bactericidal properties. *J. Hazard. Mater*., 187: 466-472.

Lin, Y., Taylor, S., Li, H., Fernando, K. A. S., Qu, L. & Wang, W. 2004. Advances toward bioapplications of carbon nanotubes. *J. Mater. Chem*., 14:527- 547.

Liu, F., Zhang, X. B., Cheng, J.P., Tu, J. P., Kong, F. Z., Huang, W. Z. & Chen, C. P. 2003. Preparation of short carbon nanotubes by mechanical ball milling and their hydrogen adsorption behavior. *Carbon,* 41: 2527-2532.

Liu, X., Yu, L., Liu, F., Sheng, L., An, K., Chen, H. & Zhao, X. 2012. Preparation of Ag–Fe-decorated single-walled carbon nanotubes by arc discharge and their antibacterial effect. *J. Mater. Sci.,* 47: 6086-6094.

Lu, L., Ai, K. & Ozaki, Y. 2008. Environmentally friendly synthesis of highly monodisperse biocompatible gold nanoparticles with Urchin-like shape. *Langmuir*, 24: 1058-1063.

Marshall, M. W., Nita, S. P. & Shapter, J. G. 2006. Measurement of functionalised carbon nanotube carboxylic acid groups using a simple chemical process. *Carbon,* 44: 1137-1141 .

Melvin, G. J. H., Ni, Q. Q., Suzuki, Y. & Natsuki, T. 2014. Microwave-absorbing properties of silver nanoparticle/carbon nanotubehybrid nanocomposites. *J. Mater. Sci*., 49: 5199-5207.

Mohan, S., Oluwafemi, O. S., George, S. C., Jayachandran, V. P., Lewue, F. B., Songca, S. P., Kalarikkal, N. & Thomas, S. 2014. Completely green synthesis of dextrose reduced silver nanoparticles, its antimicrobial and sensing properties. *Carbohydr. Polym.,* 106: 469-474.

Morones, J. R., Elechiguerra, J.L., Camacho, a., Holt, K., Kouri, J.B., Ramírez, J. T. & Yacaman, M.J. 2005. The bactericidal effect of silver nanoparticles. *Nanotechnology*, 16: 2346 -2353

Oraby, M. A., Waley, A. I., El-Dewany, A. I., Saad, E. A. & Abd El-Hady, B. M. 2013. Electrospinning of gelatin functionalized with silver nanoparticles for nanofiber fabrication. *Model Numer Simul Mater Sci*., 3: 95-105.

Pal, T., Maity, D.S. & Ganguly, A. 1988. Silver-gelatin method for determination of inorganic peroxides in alkaline solution. *Talanta,* 35: 658-660.

Park, K. C., Hayashi, T., Tomiyasu, H., End, M. & Dresselhaus, M. S. 2005. Progressive and invasive functionalization of carbon nanotube sidewalls by diluted nitric acid under supercritical conditions. *J. Mater. Chem*., 15: 407-411.

Peng, J., Qu, X., Wei, G., Li, J. & Qiao, L. 2004. The cutting of MWNTs using gamma radiation in the presence of dilute sulfuric acid. *Carbon*, 42: 2741-2744 .

Seo, Y., Hwang, J., Kim, J., Jeong, Y., Hwang, M. P. & Choi, J. 2014. Antibacterial activity and cytotoxicity of multi-walled carbon nanotubes decorated with silver nanoparticles. *Int. J. Nanomedicine,* 9: 4621-4629 .

Sharma, V. K., Yngard, R. A. & Lin, Y. 2009. Silver nanoparticles: green synthesis and their antimicrobial activities. *Adv. Colloid Interface Sci.,* 145: 83-96.

Sunil, K. & Narayana, B. 2008. Spectrophotometric determination of hydrogen peroxide in water and cream samples. *Bull. Environ. Contam. Toxicol*. 81(4): 422-426.

Vasileva, P., Donkova, B., Karadjova, I., Dushkin, C. 2011. Synthesis of starch-stabilized silver nanoparticles and their application as a surface plasmon resonance-based sensor of hydrogen peroxide. *Colloids Surf., A*, 382 (1–3): 203–210.

Wang, Y., Fang Li, Y. & Huang, C.Z. 2009. A One-Pot Green Method for One-Dimensional Assembly of Gold Nanoparticles with a Novel Chitosan−Ninhydrin Bioconjugate at Physiological Temperature. *J. Phys. Chem. C*, 113: 4315-4320.

Watt, N. T., Routledge, M. N., Wild, C. P. & Hooper, N.M. 2007. Cellular prion protein protects against reactive-oxygen-species-induced DNA damage. *Biol. Med*., 43(6): 959–967.

Xu, W., Kong, J. S., Yeh, E. Y-T. & Chen, P. 2008. Single-molecule nanocatalysis reveals heterogeneous reaction pathways and catalytic dynamics. *Nature Materials*, 7: 992-996.

Zhan, J. H., Bando, Y., Hu, J. Q., Liu, Z. W., Yin, L. W. & Golberg, D. 2005. Fabrication of Metal–Semiconductor Nanowire Heterojunctions. *Angew. Chem. Int*., 44: 2140-2144.

Zhang, H. B., Lin, G. D., Zhou, Z. H., Dong, X. & Chen, T. 2002. Raman spectra of MWCNTs and MWCNT-based H_2-adsorbing system. *Carbon*, 40: 2429-2436.

Chapter 6

Conclusion and Future Perspectives

Nanotechnology is highly significant today due to the ability to develop new and efficient materials for various applications. But as its popularity is increasing, the need to develop more environmentally friendly synthetic protocols for the nanomaterial has become a serious concern. Considering this fact, this study reports on greener techniques for the synthesis of core-shell and core-multi shell quantum dots, silver nanoparticles and silver nanocomposites. The first part of the thesis involves the synthesis of core- shell quantum dots and their polymer nanocomposite. The second part of the thesis involves the synthesis of stable biopolymer-capped silver nanoparticles. The salient results are summarized in this chapter followed by suggestions for future works.

Cadmium based core shell and core-multi shell QDs have been successfully synthesized using a non-TOP based method in the absence of an inert atmosphere via hot precursor injection technique. The structural and morphological characterization revealed that the as-synthesized QDs are stable, highly crystalline and monodispersed. The as-synthesized QDs were dispersed in various polymer matrices to produce fluorescent polymer nanocomposites. Optical analyses of the as-synthesised CdSe/CdS/ZnS core-multi shell QDs showed that as the growth time increases, the absorption and emission spectra shifted towards the red region indicating increase in particle size. All the samples showed high fluorescent lifetime of around 10 nano seconds. Structural and morphological analysis revealed that the particles are small, monodispersed and highly crystalline. The dispersion of the as-synthesized CdSe/CdS/ZnS QDs in epoxy polymer matrix produced fluorescent polymer nanocomposite which can be used as the polymer cap for LED

device fabrication. The luminescence position of the polymer shifted from blue region to yellow region after the addition of QDs. In addition, the fluorescent life time of the composite decreases due to the well passivation of the QDs surface by the polymer chains. The problem of nanoparticle agglomeration in polymer matrix while preparing composite was not observed in this study. This has been attributed to the compatibility of the QDs surface and polymer chains. The TEM image of the composite shows that the QDs are uniformly dispersed inside the composite without any agglomeration. This is one of the success of this study. The brillouin spectra of the composite revealed that adding QDs to the polymer varied the acoustic frequency of the composite. The tensile measurement of the composite showed that the mechanical property of the polymer increased after the addition of the quantum dots.

In another study, highly fluorescent CdSe/ZnS core-shell QDs was synthesized using a phosphine free one pot synthetic method in the absence of an inert atmosphere. The as-synthesized materials were highly crystalline with high quality emission and absorption properties. The CdSe/ZnS core shell QDs were dispersed in PMMA matrix to prepare highly fluorescent bright yellow emitting PMMA-CdSe/ZnS QD nanocomposite thin film. This type of composite can be applied to flexible coloured filters, full colour displays and for the fabrication of brand new solid lighting devices.

In an effort to bring more environmentally friendly reagents to the synthesis protocol, HDA capped CdSe nanoparticles were also synthesized via a simple non-organometallic and non-TOP based method, by dispersing the as-synthesised CdSe cluster in octadecene followed by thermolysis in hexadecylamine in the absence of an inert gas. The nanoparticles obtained were of high quality and monodispersed with high absorption and

emission features. The as-synthesized CdSe NPs were dispersed in a biopolymer polycaprolactone to produce orange emitting electrospun polymer nanocomposite nanofibers for possible applications in biomedical field.

This study also reported the synthesis of water soluble QDs via ligand exchange. The organic soluble CdSe/ZnS QDs were successfully converted to highly water soluble materials after ligand exchange with mercaptoundecanoic acid (MUA) without the loss of their emission properties. After the ligand exchange, the morphology and above all the fluorescence property of the quantum dots were intact. There was a slight blue shift in the absorption and emission maxima positions of the water soluble compared to the organic – capped core-shell QDs. This is attributed to the redistribution of the electronic density and increase in the quantum confinement energy of the water soluble QDs. Compared to several reported works in which the retention of the emission property after ligand exchange was a major problem after surface modification, this synthetic route for organically soluble QDs is very promising for synthesizing high quality water soluble QDs. This high quality material will be useful in biological systems for various biolabelling applications.

In the second part of the study, different biopolymer capped silver nanoparticles were synthesized using a completely green method. By varying the reaction time, the temporal evolution of the growth, optical, antimicrobial and sensing properties of the as-synthesised Ag-NPs were investigated. Both gelatin capped Ag-NPs and starch capped Ag- NPs showed better antibacterial efficacy against E.coli and p.aeruginosa. Compared to the starch capped Ag-NPs, gelatin capped Ag-NPs gave better MIC and MBC. This has been attributed to the smaller particle size of the gelatin capped Ag-NPs. The cell viability

of Ag-NPs against human THP-1 cells shows that the as synthesized particles are less toxic at concentrations less than 10 µg/ml. The preliminary screening was only done and future work is to study in detail the mechanism of cell destruction by Ag-NPs and diagnosing the morphological change happening during the interaction between nanoparticles and cells using SEM. The as-synthesized Ag-NPs showed efficient sensing activity against H_2O_2. Gelatin-capped Ag-NPs showed a detection limit upto 10^{-6}M while starch-capped Ag-NPs was upto 10^{-10} M. This may be due to the structural difference between the two polymers and also the effect of capping. Gelatin protects the Ag-NPs more efficiently thus, the silver ions cannot interact with the H_2O_2 at very low concentrations like starch capped Ag-NPs.

In the latter part of the study, silver functionalised MWCNTs hybrid nanocomposites were prepared via a simple procedure The optical and structural characterization revealed that the Ag-NPs are uniformly dispersed on the surface of MWCNTs through an amide linkage between the –COOH functional group of the MWCNTs and $–NH_2$ group of the gelatin capped Ag-NPs. The Ag-MWCNTs hybrid nanocomposite showed promising catalytic activity in the conversion of p-nitrophenol to p-aminophenol in the presence of $NaBH_4$. This kind of hybrid nanocomposites synthesized using green techniques will improve its practical application in various fields especially biomedical applications.

Future work and recommendations

Fluorescent core shell and core-multi shell quantumdots and its polymer nanocomposites have already proven to have immense scope for application in various fields. Many aspects of these materials still need to be explored in order to make these materials suitable for more specific applications like biomedical field. Some of the parameters

include its purity, stability in buffer pH, tuning the core and shell thickness to make the material emit in certain wavelength etc. Some of the aspects of this work which can be further explored are:

In core-multi shell quantum dots, the thickness of various shells influence the overall optical properties of the final material. Therefore, analyzing the effect of shell thickness on the overall property and stability of the core-multi shell quantum dots should be investigated.

Replacement of CdSe NPs with more efficient materials like CdTe NPs will increase the fluorescence and absorption wavelength towards the IR region which is important for deep tissue penetration in biological application.

Semiconductor nanocrystals are known for showing high quality non-linear optical properties (NLO). A detailed study of the non-linear optical properties of various QDs can be done. The effect of various shells on the NLO properties of these materials is an interesting area to consider.

Addition of fillers influence various mechanical and rheological properties of polymers. Various thermal and mechanical properties of the polymer-QD nanocomposite can be studied to understand the effect of fillers on the polymer properties.

Fabrication of QDs/Polymer composites by directly dispersing the core/multi-shell QDs into polymer resin as the encapsulating and light conversion materials for the application on the various light LED, more specifically White LED.

Various hybrid nanocomposites of carbon nanostructures using Ag-NPs can be prepared and their catalytic efficiency can be studied. For example replacing MWCNTs with

graphene. Adopting green synthetic procedures for the preparation of these hybrid composites will enhance its application in various biomedical applications.